Post-Seismic deformation in the Vrancea Region (Romania)

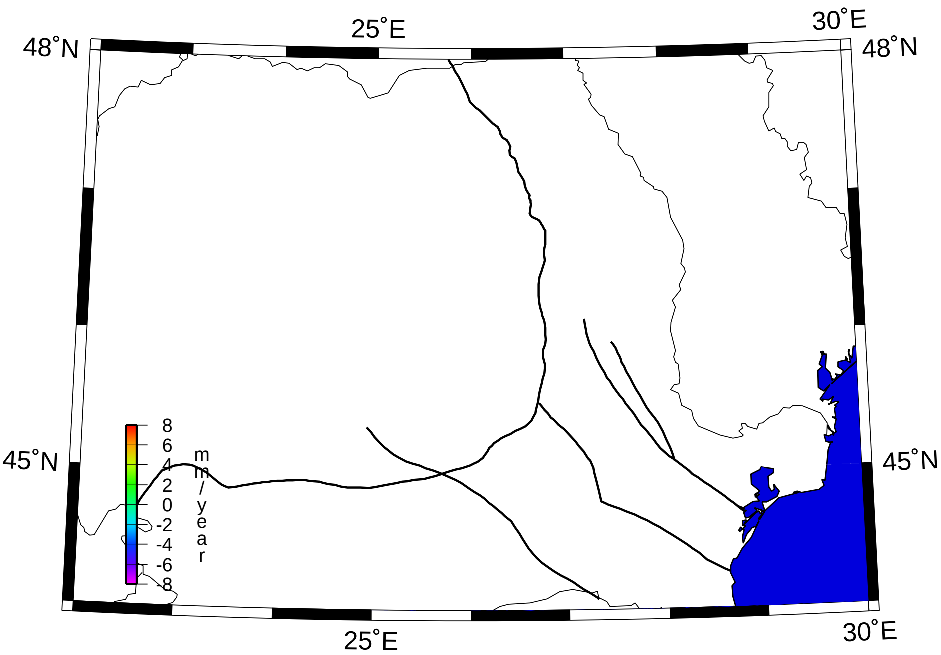

J. Van Hove

Astrodynamics & Satellite Systems
Faculty of Aerospace Engineering
Delft University of Technology
Kluyverweg 1, 2629 HS Delft
The Netherlands

Post-Seismic deformation in the Vrancea Region (Romania)

Master of Sience Thesis

J. Van Hove

Delft, 20 October 2004

Supervisor	:	Dr. L.L.A. Vermeersen
Co-supervisors	:	Ir. A.G.A. van der Hoeven
		R.E.M. Riva, M.Sc.

Astrodynamics &
Satellite systems

This document was typeset with $\LaTeX 2_\varepsilon$.
The layout was designed by Remko Scharroo © 1993–2002

Preface

This report was written as a conclusion to the Master of Science program for the Faculty of Aerospace Engineering of the Delft University of Technology. It describes the calculation of postseismic surface displacements following intermediate-depth earthquakes in the Vrancea Region and how they contribute to GPS observed displacements in south-east Romania.

The calculation of the displacements has been based on the lecture notes of "Geophysical applications of satellite measurements" (AE4-877) and on the *Geophysical Journal International* paper "Global post-seismic deformation". The GPS observed velocity vectors used in this report are obtained from a GPS network covering a large part of Romania. A subject about which a more extensive reading can be found in the *EOS* paper "GPS Probes the kinematics of the Vrancea seismogenic zone".

Chapter (2) briefly explains the structure of the Earth, plate tectonics and the geometry of earthquakes in general and for the Vrancea region in particular. The theory on which the postseismic calculations are based is given in Chapter (3). This theory differs from the Normal Mode Analysis as it is used for the calculation of postglacial rebound in two ways. For postseismic relaxation, in addition to the spheroidal component, a toroidal component to the surface displacements has to be taken into account and an earthquake is modeled as an internal loading to the Earth model, not a surface loading. Readers not interested in any theory are directed to Chapter (5) for the general results of intermediate-depth earthquakes applied to several realistic Earth models. Chapter (6) gives a comparison between the displacements as they where numerically modeled and observed by a GPS network. Chapter (6) also contains more information about the GPS network in Romania. Conclusions and recommendations can be found in Chapter (7).

I would like to show my gratitude towards my supervisor Bert Vermeersen and co-supervisors Riccardo Riva and Andre van der Hoeven for sharing their experience and providing me with all the information I needed.

I also want to thank all the students in the student rooms for their help concerning all the problems I encountered during programming and with the English language. For assisting me with the generation of the figures as they are present in the report I would like to thank Mark Knegt and Riccardo Riva.

For their help with the grammar and structure of this report I would like to thank Bert Vermeersen, Vanessa Ratard, Greet Leegwater and Bert Wouters. Of which the last two also deserve together with my parents a special thanks for comforting me or just enduring my presence during the whole graduation process.

Contents

Summary

The Vrancea region in Romania is known for its very complicated tectonic setting. It is the border region of three main tectonic units in south-east Romania. The collision between these units is believed to be the origin of the East and South Carpathians. The Vrancea region is also the home of a large amount of intermediate-depth earthquakes that are all confined to a relatively small volume corresponding with a seismic detectable slab starting from a depth of 60-70 km. What this slab exactly is, is still is a point of discussion among scientists. It remains unanswered whether the slab is a subducted oceanic lithosphere or a part of the lithospheric mantle that has been separated and sunk gravitationally into the underlying mantle, and also whether the slab is still attached, in progress of detachment or already detached.

What is known is that the horizontal crustal movement of the area between the Vrancea region and the Black Sea is mainly in a south-east direction relative to the assumed stable Eurasian platform. This was concluded in [*van der Hoeven, et. al.*, 2004] where GPS vector solutions are given based on data of the combined *Netherlands Research Center for Integrated Solid Earth Sciences* (ISES), the *German Research Foundation* (DFG) and *Collaborative Research Center* (CRC) 461 networks in Romania. Also known is that when the tectonic processes mentioned above are modeled they never result in acceptable approximation of the GPS observed movements, some even result in displacements in the opposite direction. Thus, the question arises : "What is the contribution of the major intermediate-depth Vrancea earthquakes of the last thirty years to the GPS observed movements in the south-east of Romania?".

To answer this question a study was undertaken of all available literature about the Earth structure in the region. This resulted into two realistic laterally homogeneous and radially stratified Earth models for the Vrancea region, one being a five-layer model and the other a seven-layer model. The latter is almost a replica of the five-layer model, with the exception of a low-viscosity zone being inserted. The models are mainly based on a paper about the local lithospheric strength [*Lankreijer, et. al.*, 1997] for the upper part and postglacial rebound studies for the deeper structure of the Earth.

The earthquakes used in the simulations are the March 4 1977, the August 30 1986, the May 30 1990 and the May 31 1990 earthquakes. These are, according to the GMT catalogue, the only earthquakes of the last 30 years with a moment magnitude larger than 6. These earthquakes are applied as internal loadings to the incompressible, non-rotating, self-gravitating, Maxwell viscoelastic sphere representing the Earth. The displacements on the Earth's surface can then be calculated by solving the equations governing infinitesimal, quasi-static perturbations in the sphere by use of Normal Mode Analysis. Subsequently similar simulations were done for several Earth models with varying parameters resulting in three dimensional surface displacements for almost every realistic structure of the Earth.

All the simulations resulted in horizontal movements whereof the direction corresponds reasonably well with GPS observations in the area between the Vrancea Region and the Black Sea. It was recognized that the best correlation was obtained close to the Vrancea region, the region for which the Earth model was constructed. The extent to which the magnitudes of the modeled displacements and the observed movements correspond depends mainly on the depth of the boundary between the upper and lower lithospheric mantle. The best correlation was obtained for the models where the upper and lower lithospheric mantle are 20 km and 80 km thick, respectively. The viscosity of the lower lithospheric mantle also has an important influence on the resulting magnitude of the horizontal displacements. When it is equal to 10^{19} Pa s the magnitude decreases rather fast with increasing distance to the epicenters, leading to vectors that do not conform to GPS observed motions in the far-field. This decrease does not take place when the lower lithospheric mantle viscosity is equal to 10^{18} or 10^{17} Pa s. Models with these compositions resulted in the best correspondence with the GPS observation in the region of interest.

For further research related to the body of work presented in this report it is recommended to proceed with the simulations using Earth models that are not only radially stratified, so that variations in the thickness of layers are possible and local low-viscosity zones can be included in the models. Furthermore it is advised to continue the GPS observation, so as to further improve the accuracy and allow a possibility to compare the vertical displacements to the numerically modeled vertical displacements. The residual motions resulting from subtraction of the GPS observations from the modeled values should then be compared to crustal movements caused by all possible geological processes occurring underneath the Vrancea region.

Chapter 1

Introduction

Vrancea

Vrancea is a Romanian county in the Moldavia region and is located at the sharp bending zone between the eastern and southern Carpathians (see Figure 1.1). It forms the border zone between three main tectonic units: the East-European platform to the north and north-east, the Moesian plate to the south and the Tisia-Dacia block to the north-west [*Dinter and Schmitt*, 2001]. In [*Lankreijer, et. al.*,

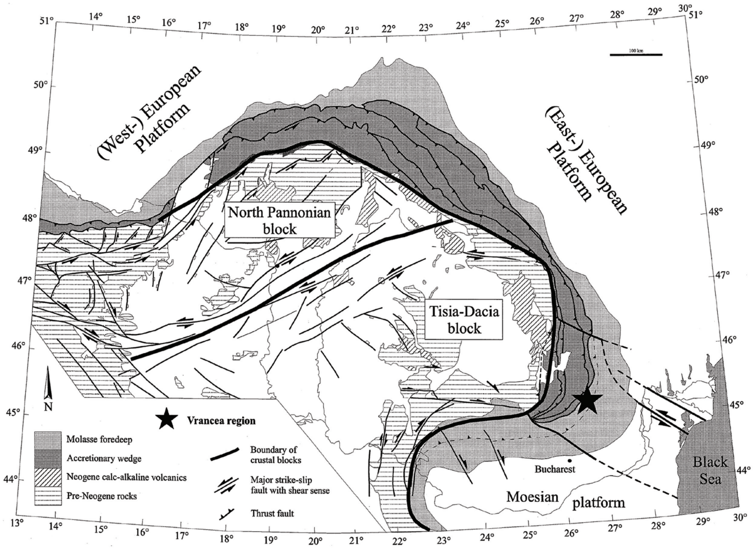

Figure 1.1 Location of the Vrancea region, [*Sperner, et. al.*,2001]

1997] it is suggested that in the late Mesozoic there was a small ocean similar to the Black Sea at the location of the Carpathians. The oceanic plate subducted under the Tisia-Dacia block closing the small ocean and a collision followed between the European platform, that was attached to the oceanic plate, and the Tisia-Dacia block creating the Eastern Carpathians. This oceanic plate pulled on the attached continental platform, causing it to enter the subduction zone. However, other authors [*Chalot-Prat and Girbacea*, 2000], [*Gvirtzman*, 2002], [*Girbacea and Frisch*, 1998] believe that the continental lithosphere is unsubductable due to its higher buoyancy (Section 2.2). And, that the constant gravitational pull of the subducted oceanic lithosphere caused the delamination between the continental lithosphere and its underlying lithospherical mantle and roll-back of the latter. Thus, implying that at the contact zone between the oceanic and continental crust the opposite stresses were larger than the strength of the local material, causing it to break. The dense oceanic lithosphere continued to sink gravitationally while the fracture grew horizontally. This resulted in the present-day situation where a delaminated lithospheric mantle is positioned vertical underneath the Vrancea region, 130 km away from the break-off point. The resulting gap was filled by material of the underlying asthenosphere (Section 2.1). Eventually this has led to the brake-off of the subducted slab, oceanic lithosphere or lithospheric mantle. This break-off has started in the west of the Carpathian Arc during early Miocene [*Nemcok, et. al.*, 1998] and moved along the arc-shaped Carpathians towards its present position, the Vrancea area.

Another question is whether presently the slab is still attached, in progress of detachment or already detached. Several seismologic measurements [*Fan, et. al.*, 1998], [*Sperner, et. al.*, 2001], [*van der Hoeven, et. al.*, 2004] have identified the existence of a 20 to 60 km wide and 130 km long body, that has different material characteristics than the surrounding area. The same measurements sometimes detect an area above this body with no anomalies regarding the environs between 40 and 60-70 km depth; which could mean that the subducting body is already detached. This is however contradicted by several authors (e.g. [*Sperner, et. al.*, 2001], [*Chalot-Prat and Girbacea*, 2000], [*Gvirtzman*, 2002]) who claim that the measurements were done with too low a resolution, that the stresses measured in the body are too large for it to be detached, or that the measured anomalies are actually the asthenosphere risen.

A very important tool in efforts to answer these questions is GPS. GPS is presently considered to be one of the most powerful space-geodetic tools to measure the three dimensional surface deformations [*van der Hoeven, et. al.*, 2004]. In the same paper velocity vector solutions are given for the present-day horizontal crustal movement in Romania. These solutions are based on observation of the combined *Netherlands Research Center for Integrated Solid Earth Sciences* (ISES), the *German Research Foundation* (DFG) and *Collaborative Research Center* (CRC) 461 networks in Romania. The network has repeatedly been observed since 1998. For the scope of this report its main conclusion is that the movement of the crust of the area between Vrancea and the Black Sea is in the south-east to south direction.

This conclusion is important because many geological and geophysical studies [*van der Hoeven, et. al.*, 2004] have tried to determine the cause of the GPS observed surface displacements in terms of active long-term geodynamic processes such as convergence, subduction and slab break-off. They all failed in giving a good estimate of the crustal movement in the Vrancea region and the whole area south-east (see Figure 1.1) as it was observed. These studies did not take into account that the earthquakes that occurred in the past could have a large influence on the present-day crustal movement.

The fact remains that the structure under the Vrancea region as described by the seismology field is confirmed by the location of major earthquakes (see Figure 1.2). Although minor earthquakes are spread all over the crust in Romania, the largest in strength are confined to the same area, the subducting slab underneath the Vrancea region (see Figure 1.2). Moreover, there is also an area of no seismic activity between 40 and 60-70 km depth [*Bala, et. al.*, 2003], [*Chalot-Prat and Girbacea*, 2000], [*Girbacea and Frisch*, 1998]. Similarly, this is not proof that the slab is already detached. It is important to have a better understanding of the effect on the surface of all possible processes active inside the Earth so that they can be linked to the horizontal and vertical displacements, measured by use of GPS. This

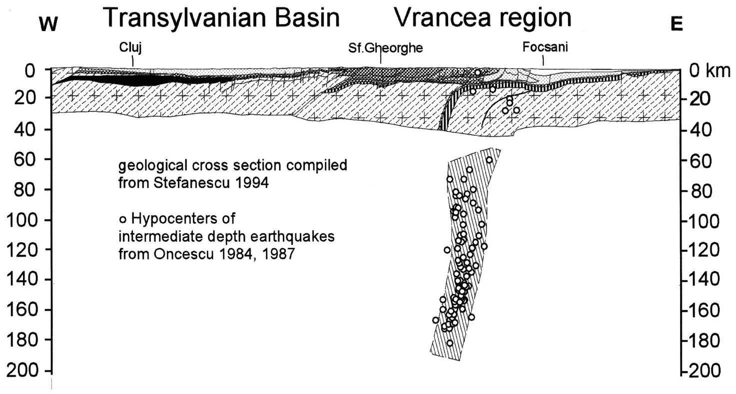

Figure 1.2 Hypocenters intermediate depth earthquakes, [*Linzer, et. al.*,1998]

way a better understanding of the structure of Earth and what internal processes can cause is obtained.

Postseismic deformation

The objective of this project as described in this report was to calculate the contribution of the major earthquakes of the last 30 years to the present-day horizontal and vertical crustal movements, using realistic Earth models and comparing the results with GPS observed displacements of the Vrancea region. The surface displacements induced by the redistribution of the stresses inside the different layers of the Earth years after an earthquake, that caused the sudden build up of stress, are called postseismic deformations. The earthquakes used for these calculations are the 4 March 1977, the 30 August 1986, the 30 May 1990 and the 31 May 1990 events. These are according to the *Harvard CMT catalogue* the only events in the Vrancea area in the last 30 years that reach a moment magnitude (M_W) higher than 6. All these earthquakes occurred between a depth of 60 to 140 km, making them intermediate depth events. This is an important fact because until now most of the research on postseismic deformation concerned shallow earthquakes. Still little is known about the effect of the events occurring at intermediate depth.

A realistic Earth model means that the model utilized for the simulation is the most appropriate radially stratified sphere, when the known composition of the Earth underneath the research area is considered. Here a strength profile of the local lithosphere is used for the structure of the upper layers of the model, while the viscosities and thicknesses of the layers of the mantle are based on postglacial rebound studies. So, it is assumed that the Earth is built up of several layers with constant material properties. Of course in reality the Earth can not be separated into homogeneous layers, there are lateral discontinuities of all the material properties. The constant values should be seen as an average over the whole layer. Furthermore, for the simulations a self-gravitating, viscoelastic Maxwell Earth model is applied. The simulations approach used is almost totally analytical and based on the *Normal Mode Theory*.

Structure of the report

The report is composed of seven chapters. In **Chapter 2** the structure of the Earth, global plate tectonics and the tectonic situation in the Vrancea region are discussed. Following these is a discussion on earthquakes in general and the earthquakes used in this report.

Chapter 3 provides the mathematical background used to calculate the post-seismic surface displacements induced by the earlier discussed earthquakes. Here a set of equations describing the assumed conditions in laterally homogeneous spherical Earth models is given. Followed by a thorough explanation of the method used to analytically solve these equation for an internal loading applied to the model.

Based on the lithospheric strength profile as it is given in [*Lankreijer, et. al.*, 1997] and post-glacial rebound studies, in **Chapter 4** values are assigned to the different parameters of a five- and a seven-layer Earth model. Both of these models form the initial concept used to compose several other models by altering one parameter (like viscosity or thickness of a layer) of the model.

The results of the actual calculations are presented in two parts. The emphasis in **Chapter 5** lies on determining the influence of the intermediate depth earthquakes on surface displacement. This is obtained by comparing the results of the different Earth models.

In **Chapter 6** one model that is realistic and whose results correspond to the GPS observations is selected from all the simulated models and is adjusted according to the latest research about the local composition of the Earth. Using the Normal Mode Theory, deformations are calculated for several viscosities. The results are compared to the GPS measurements to find out what the influence of the earthquakes on the observed velocities are in the area.

The report ends with conclusions and recommendation pertaining to the results obtained, in **Chapter 7**.

Chapter 2

Plate tectonics and earthquakes

In this chapter an introduction will be made to the global Earth structure and plate tectonics mainly based on the theory as it was described in [*Vermeersen*, 2002a]. The source of the general description of earthquakes (section 2.3) is [*Stein and Wysession*, 2003].

2.1 Earth structure

Based on seismologic research the interior of the Earth can be separated in three layers: the crust, the upper-most layer, the mantle, the central layer and the core, the interior layer. As Figure (2.1) shows, each of these layers can then be sub-

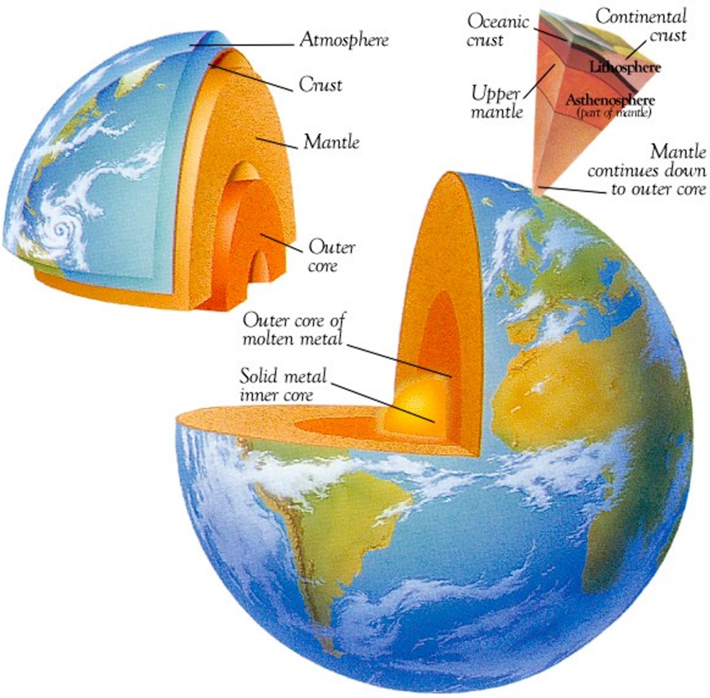

Figure 2.1 Internal structure of the Earth, [*Sklyarov*]

divided into several other layers. The crust forms the surface we live on or the ocean's floor. In general the oceanic crust is thinner but denser than the continental crust. The boundary between the crust and the mantle is the so-called *Mohorovicic discontinuity* or *Moho* and is seismically detectable. The average depth of the Moho is 35 km but can vary from 0 km at a *mid-ocean ridge* (see Chapter 2.2) to 70 km beneath mountains.

The mantle is almost 2900 km thick and contributes to about 80 % of the Earth's total volume. The mantle is split into the upper and the lower mantle by the 670 km discontinuity. Beneath this boundary no earthquakes occur.

The lower mantle is separated from the core by the *Core - Mantle Boundary* (CMB) at a depth of about 2900 km. The core exists of an outer core of molten metal and a solid metal inner core that starts at a depth of approximately 5150 km. The mean radius of the Earth is 6371 km. The metal 'fluid' in the outer core moves with velocities of about 0.1 mm/s, which makes the core a sort of dynamo that generates the Earth's magnetic field.

There is also another possibility for the differentiation of the upper layers of Earth: the crust and the most upper part of the mantle form the lithosphere. This lithosphere is considered the strongest layer of the Earth and can reach to a depth of about 200 km. The lithosphere is believed to be situated on a very hot, semi-solid part of the upper mantle known as the asthenosphere. The asthenosphere is a weaker part of the upper mantle.

2.2 Plate tectonics

The crust is not one whole shell; in global plate tectonics it is divided into 15 rigid plates (see Figure 2.2). The plates are rigid in the sense that it is assumed that deformations take place at the boundaries. These 15 plates are of two types: oceanic and continental ones. Figure (2.2) illustrates that many plates contain

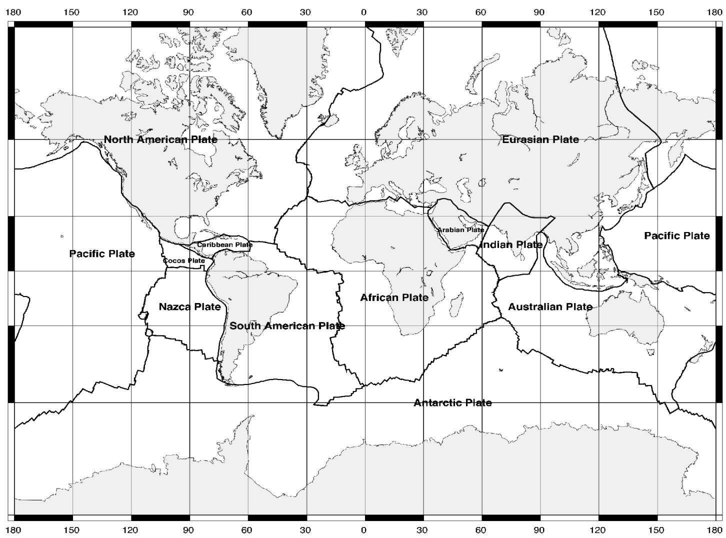

Figure 2.2 Tectonic plates of the present-day Earth, [*Mueller*]

a (part of a) continent and an (part of an) ocean and are thus a combination of both crustal types. The boundaries where an ocean runs adjacent to a continent inside a plate is called a *passive plate margin*. The plates move relative to each other, with a maximum of about 100 mm/year. The direction and velocity of the plate movement has hardly changed over the past million years . A boundary between two moving plates is called an *active plate margin* or *transform fault* when the relative motion is mainly horizontal. It is important to note that although the majority of movement processes occur at plate boundaries, they are not the only place where the events can occur. Some plates are built up of smaller plates which also move relative to each other. So the same events as described below can take place inside a plate.

The fact that the plates move in different directions means that some plates will collide while others will drift apart. In case of the latter, as there is no crust to cover the mantle, an upward flow of molten materials from the mantle (magma) reaches the Earth's surface or the ocean floor. In oceans it is called a *mid-ocean ridge*. There the magma condenses and becomes part of the diverging ocean plates.

In the case of two plates moving towards each other again a differentiation must be made between oceanic and continental plates. As stated previously an oceanic plate is denser than a continental plate and it is possible that part of it consists of the same material as the mantle below. When an oceanic plate runs into another plate and a downward motion is triggered, the oceanic plate can start to sink into the mantle below. This is known as *subduction* and the velocity of the process can run up to 100 mm per year. The exact trigger of this process is not always known but sediments on the ocean floor can be a driver. This total process, the renewal and subduction of material, means that oceanic lithosphere is not older than approximately 200 million years. When a subducted plate is connected to a continental plate it is possible that over time the continental plate will start subducting when it reaches the boundary. However, it would not totally sink because of it lesser density. The part already subducted would probably tear off in time and sink further. In general conditions however, continental plates will not subduct because of their lower density and thus higher buoyancy. Buoyancy is the difference between the force pushing the plate down and the upward pressure exerted by the underlying mantle. The Vrancea area is at the moment one of the few places on Earth where late-stage development of active ocean-continent collision, combined with subduction in a relative small area, can be studied [*van der Hoeven, et. al.*, 2004], [*Sperner, et. al.*, 2001]. Although it is not clear at what stage the subducted slab is at, it is known that the plates are past the ocean-continental collision stage and have moved into a continental-continental collision.

In case of two continental plates converging, both will thicken at the contact zone and a chain of mountains arises. This is what happened in the Vrancea region between the three main tectonic units: the East-European platform, the Moesian plate and the Tisia-Dacia block. The collision created the Carpathians.

2.3 Earthquakes

The motion between two massive plates is not smooth. The deforming boundaries cause stress to build up along the fault. This process, that is part of the so-called *seismic cycle*, can take over thousands of years and is called the *interseismic stage*. During this stage there is a possibility of movement in the neighborhood of the fault but the fault itself stays locked. The next stage is the *pre-seismic stage*; it begins shortly before the actual earthquake and it is often associated with small earthquakes (*foreshocks*). The earthquake itself is the moment when the built-up stress (partially) releases because the rocks can no longer take the stress anymore and break. It marks the *co-seismic* stage of the cycle. This is the most disastrous phase because in just a few seconds the fault can move a couple of meters with sometimes catastrophic results for the people and buildings on the surface. The final stage is known as the *post-seismic phase* and starts after the *aftershocks*. The stress is then redistributed over all the layers of the Earth. It can be the cause for surface velocities up to centimeters a year. Afterwards the fault settles into interseismic behavior again.

Because of the long duration of the total process it is hard to study the cycle. There is no data available for a whole cycle at one location. There is however data from observation of different places. It is assumed that the total gives an insight in the whole cycle but the accuracy of this assumption is not known. This means that earthquake physics remains an uncertain research area where a variety of techniques is used in several active studies. An important result from research performed by seismology and geodesy for postseismic studies of earthquakes is the fault geometry. When an earthquake occurs waves start traveling trough the different layers of the Earth. By measuring the time the waves take to arrive to seismometers at different sites and assuming velocity profiles for all the layers the waves travel trough, it is possible to determine the location of an earthquake. The amplitudes and shapes of these seismic waves are used to outline the size of the earthquake and the geometry of the fault on which it occurred. The exact technique used will not be further explained.

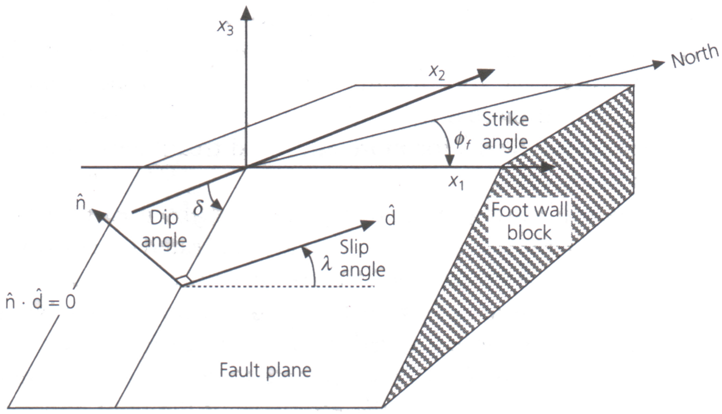

Figure 2.3 Fault geometry, [*Stein and Wysession*,2003]

Fault geometry is assumed to consist of a plane, the *fault plane*, that describes the movement of two plates relative to each other due to an earthquake (see Figure 2.3). The intersection line of this plane and the Earth surface is called the *strike*. The *slip angle* λ gives the direction in which the upper block moves with respect to the lower block. This direction also determines the direction of the fault. The *strike* angle ϕ_f can now be determined as the angle clockwise from the geographical north in direction of the fault. The *dip angle* δ defines the direction of the fault plane relative to the Earth's local surface. The *hypocentre* is the center of the earthquake and the *epicenter* is its perpendicular projection on the Earth's surface. The distance between these two defines the depth of the earthquake. The main direction that the two tectonic units move relative to each other determines whether an earthquake is classified as having a *strike-slip* or a *dip-slip source*. In the Vrancea region the intermediate depth earthquakes are caused by subduction, resulting in the assumption that all the earthquakes have a slip-dip source.

In this report the geometry was further simplified; it was assumed that the units move or only vertical or only horizontal relative to each other. This means

Table 2.1 Seismic source parameters for the Harvard CMT solution

Date	d (km)	δ (Deg)	ϕ_f (Deg)	M_0 (Nm)	LAT (Deg)	LONG (Deg)
4-Mar-77	83.6	62.0	235.0	$1.99E+20$	45.23	26.17
30-Aug-86	132.7	72.0	240.0	$7.91E+19$	45.76	26.53
30-May-90	74.3	63.0	236.0	$3.01E+19$	45.92	26.81
31-May-90	87.3	69.0	309.0	$3.23E+18$	45.67	26.00

Table 2.2 Seismic source parameters for the regional solution

Date	d (km)	δ (Deg)	ϕ_f (Deg)	M_0 (Nm)	LAT (Deg)	LONG (Deg)
4-Mar-77	94.0	70.0	220.0	$7.08E+19$	45.34	26.30
30-Aug-86	131.0	65.0	235.0	$5.01E+19$	45.52	26.49
30-May-90	91.0	63.0	236.0	$3.55E+19$	45.83	26.90
31-May-90	79.0	69.0	309.0	$4.47E+18$	45.83	26.89

that for a slip-dip source the slip angle was assumed to be rectangular and no further consideration was given to two dimensional movements in the fault plane. For the calculations of postseismic deformations at the Earth's surface an earthquake was thus completely defined by its coordinates (LAT, $LONG$), depth (d), dip (δ) and strike ϕ_f direction, moment magnitude M_W and the date at which the earthquake occurred. For each earthquake these quantities were measured by a network of seismometers. It is noteworthy that these quantities can differ quite a lot depending on the use of a global network like the *Harvard CMT Catalog* (see Table 2.1) or a regional network of stations (see Table 2.2). It was not possible to determine which of the two is better, so both of them are used to generate the postseismic deformations that were compared with GPS measurements. However, this is not applicable to the first section of the research, as its objective was to study the differences in surface displacements caused by intermediate-depth earthquakes, for several Earth models. Thus, it was of lesser importance that the quantities were not exactly known as the same set of data was used for all the simulations. That is also why only the three strongest earthquakes as given in the first three rows in Table (2.1) were used.

Chapter 3

Mathematical background

In this chapter the general equations will be discussed and solved. These are the equations governing infinitesimal, quasi-static perturbations in a spherical, incompressible, non-rotating, self-gravitating, Maxwell viscoelastic sphere representing the Earth, subjected to an internal load. Furthermore it will be assumed that the Earth is laterally homogeneous and hydro-statically pre-stressed. Laterally homogeneous means that it is assumed the Earth consists of separate shells (layers) of constant material properties, and a constant internal gravity acceleration g. The quantities can and in most cases do differ for different layers. Figure (3.1) shows how the Earth is divided into N layers; layer N being the core and the top of layer 1 represents the Earth's surface. Layer N_s is where the internal loading will occur.

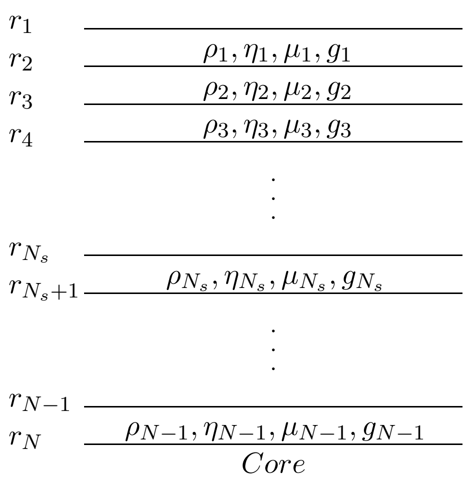

Figure 3.1 Layered structure of the Earth

Solving the equations means that in this report displacements and potential field at the surface as a result of the internal loading are found.

The following notations are used in these derivations. A bold symbol will always represent a tensor and an arrow on top of a symbol makes it a vector. Unit basis vectors of the spherical coordinates r, θ and ϕ are respectively given by

$$\hat{e}_r = \hat{e}_1$$
$$\hat{e}_\theta = \hat{e}_2$$
$$\hat{e}_\phi = \hat{e}_3$$

3.1 Basic equations

A particle is taken inside the described sphere. The situation where the particle is in equilibrium when a force per unit volume $\vec{F}$ is applied, that is, the force is balanced by surface stresses, is given in vector notation by

$$\nabla \cdot \boldsymbol{\sigma} + \rho \vec{F} = \vec{0} \tag{3.1}$$

with a density ρ and the symmetric stress tensor $\boldsymbol{\sigma}$. The ∇ operator in spherical coordinates is given in Appendix (A). The pressure exerted by the surrounding Earth on the particle is given as the pressure gradient:

$$\frac{dp}{dr} = -\rho(r)g(r). \tag{3.2}$$

This is a function of the radius to the center of Earth r. Equation (3.2) implies that a displacement of the internal particle by an amount $\vec{u}$ will change the surrounding pressure and thus the pressure inside the particle. This change in pressure is given as a function of the initial pressure p_0 and the displacement vector $\vec{u}$:

$$p = p_0 + \vec{u} \cdot \nabla p_0 \tag{3.3}$$

where the last term on the right hand side is the so-called convective term. Equation (3.3) expresses that the initial stress distribution is advected with the deformation [*Vermeersen*, 2002b]. A relation between the pressure and the stress is given by the hydrostatic condition

$$\sigma_{ij} = -p\delta_{ij} \tag{3.4}$$

in which the the subscript (ij) indicates the position of the stress element in the tensor. The elements of the *Kronecker delta* tensor are given by δ_{ij} [*Vermeersen*, 2002b].

A combination of equations (3.1) to (3.4) gives the balance of forces in the deformed situation:

$$-\nabla p_0 + \nabla \cdot \boldsymbol{\sigma} - \nabla \left(\rho_0 g \vec{u} \cdot \hat{e}_r\right) + \rho \vec{F} = 0 \tag{3.5}$$

where $\boldsymbol{\sigma}$ represents the acquired stress.

If the assumption is then made that the force $\vec{F}$ is equal to the gravity force and that no other forces or loads work on the particle then the disturbance force can be written as

$$\vec{F} = -\nabla \phi \tag{3.6}$$

The potential field ϕ and the density can be written as a function of their original state, respectively:

$$\phi = \phi_0 + \phi_1 \qquad \text{with } \phi_1 \ll \phi_0 \tag{3.7}$$

$$\rho = \rho_0 + \rho_1 \qquad \text{with } \rho_1 \ll \rho_0 \tag{3.8}$$

where the subscript 0 denotes the initial state and the subscript 1 the infinitesimal perturbation.

Combining equation (3.6) with (3.7) and inserting the result and equations (3.2) and (3.8) in (3.5), neglecting second-order terms, gives the following linearized equation of momentum:

$$\nabla \cdot \boldsymbol{\sigma} - \nabla \left(\rho_0 g \vec{u} \cdot \hat{e}_r\right) - \rho_0 \nabla \phi_1 - \rho_1 g_0 \hat{e}_r = 0 \tag{3.9}$$

Equation (3.9) states the conservation of momentum for a compressible self-gravitating body only subjected to the gravity. The first term represents the influence of the stress and the second the advection of the hydrostatic pre-stress. The third term describes the change in gravity and shall be zero when self-gravitation is neglected. The last term, which describes the influence of the perturbed density, shall be equal to zero because an incompressible body is considered and thus the perturbed density ρ_1 equals zero. This also has consequences for the perturbed gravitational potential ϕ_1 due to an infinitesimal displacement. This satisfies the Poisson equation

$$\nabla^2 \phi_1 = 4\pi G \rho_1 \tag{3.10}$$

where G is the universal gravitational constant, but may as result of incompressibility be derived further into

$$\nabla^2 \phi_1 = 0 \tag{3.11}$$

Now the symbol σ^E is introduced for the "elastic part" of any tensor. According to Hooke's Law this stress can be written as [*Vermeersen*, 2002b]

$$\sigma_{ij}^E = \lambda \sum_{k=1}^{3} \epsilon_{kk} \delta_{ij} + 2\mu \epsilon_{ij} \tag{3.12}$$

which gives a relation between the stress σ and the strain ϵ in homogeneous and isotropic materials. The elements of the tensor of infinitesimal deformations ϵ_{ij} are given by

$$\epsilon_{ij} = \frac{1}{2}\left(\frac{\partial u_i}{\partial x_j} + \frac{\partial u_j}{\partial x_i}\right) \qquad \text{for } i,j = 1,2,3 \tag{3.13}$$

where the elements between the parentheses are the partial derivatives of the displacements u_i to the positional coordinates x_j.

In equation (3.12) λ and μ are constant material parameters called *Lamé constants*. The latter is also referred to as the shear modulus or rigidity. They are related to the isentropic incompressibility or bulk modulus k by:

$$k = \lambda + \frac{2}{3}\mu \tag{3.14}$$

It is also possible to write σ^E by combining the constitutive relation of Maxwell viscoelasticity and the Newtonian viscosity for incompressible fluids, respectively:

$$\dot{\epsilon}_{ij} = \frac{\dot{\sigma}_{ij}}{2\mu} + \frac{\sigma_{ij}}{2\eta} \tag{3.15}$$

$$\eta = \frac{\sigma_{ij}}{2\dot{\epsilon}_{ij}} \qquad \text{for } i \neq j \tag{3.16}$$

as

$$\dot{\sigma}_{ij}^E = \dot{\sigma}_{ij} + \frac{\mu}{\eta}\left(\sigma_{ij} - \frac{1}{3}\sum_{k=1}^{3} \sigma_{kk}\delta_{ij}\right) \tag{3.17}$$

in which the dot represents the derivative with respect to time. With equation (3.17) and the derivative of equation (3.12) the relation of stress and strain for a three dimensional Maxwell model is given by

$$\dot{\sigma}_{ij} + \frac{\mu}{\eta}\left(\sigma_{ij} - \frac{1}{3}\sum_{k=1}^{3}\sigma_{kk}\delta_{ij}\right) = 2\mu\dot{\epsilon}_{ij} + \lambda\sum_{k=1}^{3}\dot{\epsilon}_{kk}\delta_{ij} \tag{3.18}$$

Next the *Laplace transformation* of a function $f(t)$ is introduced according to [*Bavinck and Meijer*, 2002]:

$$\tilde{F}(s) = \int_{-\infty}^{\infty} f(t)e^{-ts}dt \tag{3.19}$$

with t the time and s the Laplace variable. The tilde denotes Laplace transformed variables. The Laplace transformation of these equations is necessary for an analytical solution to be reached.

Equation (3.19) is then applied to equations (3.9), (3.11), (3.13) and (3.18) and also to the condition of incompressibility, as an incompressible Earth is assumed:

$$\nabla \cdot \tilde{\boldsymbol{\sigma}}(s) = \nabla\left(\tilde{\vec{u}}(s) \cdot \rho_0 g_0 \hat{e}_r\right) + \rho_0 \nabla\tilde{\phi}_1(s) \tag{3.20}$$

$$\nabla \cdot \tilde{\vec{u}}(s) = 0 \tag{3.21}$$

$$\nabla^2\tilde{\phi}_1(s) = 0 \tag{3.22}$$

$$\tilde{\boldsymbol{e}}(s) = \frac{1}{2}\left[\nabla\tilde{\vec{u}}(s) + \left(\nabla\tilde{\vec{u}}(s)\right)^T\right] \tag{3.23}$$

$$\tilde{\boldsymbol{\sigma}}(s) = \tilde{\lambda}(s)\tilde{\bar{\boldsymbol{e}}}(s)\boldsymbol{I} + 2\tilde{\mu}(s)\tilde{\boldsymbol{e}}(s) \tag{3.24}$$

with the Laplace transformed Lamé parameters

$$\tilde{\mu}(s) = \frac{\mu s}{s + \mu/\eta} \tag{3.25}$$

$$\tilde{\lambda}(s) = \frac{\lambda s + \mu k/\eta}{s + \mu/\eta} \tag{3.26}$$

and $\boldsymbol{I}$ the identity matrix with the proper dimensions. Equation (3.21) is the condition of incompressibility and it states that the convergence of the infinitesimal displacement vector is zero. All the mathematical operators are given in Appendix (A).

These five equations (3.20-3.24) are the basic equations that govern the quasi-static deformations of a spherical, incompressible, self-gravitating viscoelastic body [*Piersanti, et. al.*, 1995]. These equations are partial differential equations and are not directly analytically solvable.

3.2 Spherical harmonic decomposition

To solve the five basic equations (3.20- 3.24) the partial differential equations must be transformed into ordinary differential equations. These can then be solved by means of standard propagator techniques. The *Correspondence Principle* states that the elastic solutions in the Laplace domain give a unique time-dependent viscoelastic solution after an inverse Laplace transformation is performed [*Vermeersen*, 2002b].

In order to get to a solution the relevant fields need to be split into spheroidal and toroidal components [*Piersanti, et. al.*, 1995]. This can be done for all basic equations separately, as laterally homogeneous viscosity and density profiles were chosen. In order to do this first the spherical harmonics are introduced as

$$Y_{nm}(\theta,\phi) = (-1)^m N_{nm} P_n^m(\cos\theta) e^{im\phi} \tag{3.27}$$

with N_{nm} the norm factors:

$$N_{nm} = \sqrt{\frac{2n+1}{4\pi}\frac{(n-m)!}{(n+m)!}} \tag{3.28}$$

The spherical harmonics $Y_{nm}(\theta,\phi)$ are related to the associated Legendre functions $P_n^m(\cos\theta)$:

$$P_n^m(\cos\theta) = \frac{(1-(\cos\theta)^2)^{\frac{m}{2}}}{2^n n!}\frac{d^{n+m}}{d(\cos\theta)^{n+m}}\left((\cos\theta)^2+1\right)^n \tag{3.29}$$

where n is the degree and m is the order of the expansion.

Secondly the vector spherical harmonics $\vec{S}^{-1}_{n+m}, \vec{S}^{1}_{n+m}, \vec{S}^{0}_{n+m}$ are introduced as

$$\begin{aligned}
S^{-1}_{n+m}(\cos\theta) &= Y_{nm}(\theta,\phi)\hat{e}_r, \\
S^{1}_{n+m}(\cos\theta) &= \frac{\partial Y_{nm}(\theta,\phi)}{\partial\theta}\hat{e}_\theta + \frac{1}{\sin\theta}\frac{\partial Y_{nm}(\theta,\phi)}{\partial\phi}\hat{e}_\phi, \\
S^{0}_{n+m}(\cos\theta) &= -\frac{1}{\sin\theta}\frac{\partial Y_{nm}(\theta,\phi)}{\partial\phi}\hat{e}_\theta + \frac{\partial Y_{nm}(\theta,\phi)}{\partial\theta}\hat{e}_\phi.
\end{aligned} \tag{3.30}$$

Using this orthogonal set of vector functions a vector field can be expanded in a spherical and a toroidal part. The harmonics $\vec{S}^{-1}_{n+m}$ and $\vec{S}^{1}_{n+m}$ form the spheroidal basis, while $\vec{S}^{0}_{n+m}$ is the toroidal basis [*Hanyk*, 1999].

This can be clarified by expanding the total displacement field $\tilde{\vec{u}}(r,\theta,\phi,s)$ and the gravitational field $\tilde{\phi}(r,\theta,\phi,s)$ respectively, using the spherical harmonic function:

$$\tilde{\vec{u}} = \sum_{nm}\left[\tilde{U_{nm}}\vec{S}^{-1}_{n+m} + \tilde{V_{nm}}\vec{S}^{1}_{n+m} + \tilde{W_{nm}}\vec{S}^{0}_{n+m}\right], \tag{3.31}$$

$$\tilde{\phi} = \sum_{nm}\tilde{\phi}_{nm}Y_{nm} \tag{3.32}$$

where $\sum_{nm}$ represents $\sum_{n=0}^{\infty}\sum_{m=-n}^{n}$.

By combining (3.30) and (3.31) the displacement vector $\tilde{\vec{u}}$ can be written as the sum of the spheroidal and toroidal part:

$$\tilde{\vec{u}}(r,\theta,\phi,s) = \tilde{\vec{u}}_S(r,\theta,\phi,s) + \tilde{\vec{u}}_T(r,\theta,\phi,s) \qquad \text{where} \tag{3.33}$$

$$\begin{aligned}
\tilde{u}_{r,S} &= \textstyle\sum_{nm}\tilde{U}_{nm}(r,s)Y_{nm}(\theta,\phi) & ,\tilde{u}_{r,T} &= 0 \\
\tilde{u}_{\theta,S} &= \textstyle\sum_{nm}\tilde{V}_{nm}(r,s)\frac{\partial Y_{nm}(\theta,\phi)}{\partial\theta} & ,\tilde{u}_{\theta,T} &= -\textstyle\sum_{nm}\tilde{W}_{nm}(r,s)\frac{1}{\sin\theta}\frac{\partial Y_{nm}(\theta,\phi)}{\partial\phi} \\
\tilde{u}_{\phi,S} &= \textstyle\sum_{nm}\tilde{V}_{nm}(r,s)\frac{1}{\sin\theta}\frac{\partial Y_{nm}(\theta,\phi)}{\partial\phi}, & ,\tilde{u}_{\phi,T} &= \textstyle\sum_{nm}\tilde{W}_{nm}(r,s)\frac{\partial Y_{nm}(\theta,\phi)}{\partial\theta}
\end{aligned}$$

Now the same separation can be done for the basic equations (3.20-3.24) by substitution of the expanded deformation vector (3.31) and gravity field (3.32). Starting with the substitution of (3.31) in the condition for incompressibility (3.21), resulting in

$$\nabla\cdot\tilde{\vec{u}}_S = \sum_{nm}\left(\frac{d\tilde{U}_{nm}}{dr} + \frac{2\tilde{U}_{nm} - n(n+1)\tilde{V}_{nm}}{r}\right)Y_{nm} = 0$$

and

$$\nabla \cdot \tilde{\vec{u}}_T = \sum_{nm} \frac{\tilde{W}_{nm}}{r \sin\theta} \left(-\frac{\partial^2 Y_{nm}}{\partial\theta\partial\phi} + \frac{\partial^2 Y_{nm}}{\partial\phi\partial\theta} \right) = 0$$

for the the spheroidal and toroidal component, respectively. The latter does not result into a significant relation. The conditions for the spheroidal component can further be derived to

$$\tilde{\chi}_{nm} = \frac{d\tilde{U}_{nm}}{dr} + \frac{2\tilde{U}_{nm} - n(n+1)\tilde{V}_{nm}}{r} = 0 \tag{3.34}$$

Substitution of (3.32) in the incompressible Poisson equation (3.22) results in the following second order differential equation:

$$\nabla^2 \tilde{\phi}_1 = \sum_{nm} \nabla \cdot \left(\frac{d\tilde{\phi}_{nm}}{dr} \vec{S}^{-1}_{nm} + \frac{\tilde{\phi}_{nm}}{r} \vec{S}^{1}_{nm} \right) = 0$$

or

$$\sum_{nm} \left(\frac{d^2\tilde{\phi}_{nm}}{dr^2} + \frac{2}{r}\frac{d\tilde{\phi}_{nm}}{dr} - \frac{n(n+1)\tilde{\phi}_{nm}}{r^2} \right) Y_{nm} = 0$$

or

$$\frac{d^2\tilde{\phi}_{nm}}{dr^2} + \frac{2}{r}\frac{d\tilde{\phi}_{nm}}{dr} - \frac{n(n+1)\tilde{\phi}_{nm}}{r^2} = 0 \tag{3.35}$$

This formula can be rewritten by use of the potential stress $\tilde{Q}_{nm}$:

$$\tilde{Q}_{nm} = \frac{d\tilde{\phi}_{nm}}{dr} + \frac{n+1}{r}\tilde{\phi}_{nm} + 4\pi G\rho\tilde{U}_{nm} \tag{3.36}$$

into:

$$\frac{d\tilde{Q}_{nm}}{dr} - \frac{(n-1)}{r}\tilde{Q}_{nm} + \frac{4\pi G\rho(n-1)}{r}\tilde{U}_{nm} + 4\pi G\rho\frac{d\tilde{U}_{nm}}{dr} = 0 \tag{3.37}$$

and after substituting (3.34) results in:

$$\frac{d\tilde{Q}_{nm}}{dr} - \frac{(n-1)}{r}\tilde{Q}_{nm} + \frac{4\pi G\rho(n+1)}{r}\tilde{U}_{nm} - \frac{4\pi G\rho n(n+1)}{r}\tilde{V}_{nm} = 0 \tag{3.38}$$

Although the choice to employ the quantity $\tilde{Q}_{nm}$ may seem remarkable, its selection shall be clarified in Section (3.4.1) where the boundary conditions are discussed.

The symmetric tensor of infinitesimal deformations $\tilde{e}$ (equations 3.23 and A.2) can also be written as the sum of a spherical and a toroidal component, by substitution of (3.31):

$$\tilde{\boldsymbol{e}} = \sum_{nm} \begin{bmatrix} e_{S,rr} + e_{T,rr} & \frac{1}{2}\left(e_{S,r\theta} + e_{T,r\theta}\right) & \frac{1}{2}\left(e_{S,r\phi} + e_{T,r\phi}\right) \\ \frac{1}{2}\left(e_{S,r\theta} + e_{T,r\theta}\right) & e_{S,\theta\theta} + e_{T,\theta\theta} & \frac{1}{2}\left(e_{S,\theta\phi} + e_{T,\theta\phi}\right) \\ \frac{1}{2}\left(e_{S,r\phi} + e_{T,r\phi}\right) & \frac{1}{2}\left(e_{S,\theta\phi} + e_{T,\theta\phi}\right) & e_{S,\phi\phi} + e_{T,\phi\phi} \end{bmatrix} \quad \text{where} \tag{3.39}$$

$$\begin{aligned}
&e_{S,rr}=\frac{d\tilde{U}_{nm}}{dr}\tilde{Y}_{nm} &&, e_{T,rr}=0 \\
&e_{S,r\theta}=\left(\frac{d\tilde{V}_{nm}}{dr}+\frac{\tilde{U}_{nm}-\tilde{V}_{nm}}{r}\right)\frac{\partial\tilde{Y}_{nm}}{\partial\theta} &&, e_{T,r\theta}=-\left(\frac{d\tilde{W}_{nm}}{dr}-\frac{\tilde{W}_{nm}}{r}\right)\frac{1}{\sin\theta}\frac{\partial\tilde{Y}_{nm}}{\partial\phi} \\
&e_{S,r\phi}=\left(\frac{d\tilde{V}_{nm}}{dr}+\frac{\tilde{U}_{nm}-\tilde{V}_{nm}}{r}\right)\frac{1}{\sin\theta}\frac{\partial\tilde{Y}_{nm}}{\partial\phi} &&, e_{T,r\phi}=\left(\frac{d\tilde{W}_{nm}}{dr}-\frac{\tilde{W}_{nm}}{r}\right)\frac{\partial\tilde{Y}_{nm}}{\partial\theta} \\
&e_{S,\theta\theta}=\left(\frac{\tilde{U}_{nm}}{r}\tilde{Y}_{nm}+\frac{\tilde{V}_{nm}}{r}\frac{\partial^2\tilde{Y}_{nm}}{\partial^2\theta}\right) &&, e_{T,\theta\theta}=-\frac{\tilde{W}_{nm}}{r}\frac{\partial}{\partial\theta}\frac{1}{\sin\theta}\frac{\partial\tilde{Y}_{nm}}{\partial\phi} \\
&e_{S,\theta\phi}=\frac{2\tilde{V}_{nm}}{r}\frac{\partial}{\partial\theta}\frac{1}{\sin\theta}\frac{\partial\tilde{Y}_{nm}}{\partial\phi} &&, e_{T,\theta\phi}=\frac{\tilde{W}_{nm}}{r}\left(2\frac{\partial^2\tilde{Y}_{nm}}{\partial^2\theta}+n(n+1)\tilde{Y}_{nm}\right) \\
&e_{S,\phi\phi}=\frac{\tilde{U}_{nm}}{r}\tilde{Y}_{nm}-\frac{\tilde{V}_{nm}}{r}\left(\frac{\partial^2\tilde{Y}_{nm}}{\partial^2\theta}+n(n+1)\tilde{Y}_{nm}\right) &&, e_{T,\phi\phi}=\frac{\tilde{W}_{nm}}{r}\frac{\partial}{\partial\theta}\frac{1}{\sin\theta}\frac{\partial\tilde{Y}_{nm}}{\partial\phi}
\end{aligned}$$

The first invariant of the tensor of infinitesimal deformations $\tilde{e}$ is, according to equation (A.3), equal to:

$$\tilde{\bar{\boldsymbol{e}}} = e_{rr} + e_{\theta\theta} + e_{\phi\phi} = \frac{d\tilde{U}_{nm}}{dr} + \frac{2\tilde{U}_{nm} - n(n+1)\tilde{V}_{nm}}{r} \tag{3.40}$$

Comparison of equation (3.40) and (3.34) shows the first invariant of $\tilde{\boldsymbol{e}}$ is equal to the quantity $\tilde{\chi}_{nm}$ which for the incompressible case is zero and thus:

$$\tilde{\bar{\boldsymbol{e}}} = 0 \tag{3.41}$$

Inserting equation (3.41) into the stress tensor formula (3.24) gives:

$$\tilde{\boldsymbol{\sigma}}(s) = 2\tilde{\mu}(s)\tilde{\boldsymbol{e}}(s) \tag{3.42}$$

which is a combination of the Laplace transformed shear modulus equation (3.25) and the tensor of infinitesimal deformations equation (3.39). Therefore the stress tensor can also be split into a spheroidal and toroidal component:

$$\tilde{\boldsymbol{\sigma}}(s) = \tilde{\boldsymbol{\sigma}}_S(s) + \tilde{\boldsymbol{\sigma}}_T(s) = 2\tilde{\mu}(s)\left[\tilde{\boldsymbol{e}}_S(s) + \tilde{\boldsymbol{e}}_T(s)\right] \tag{3.43}$$

Now the last basic equation, the equation of momentum (3.20), can be split. Starting with the left-hand-side, the equations (3.21), (3.23), (3.43) and (3.31) can be combined, resulting in

$$\begin{aligned}
\nabla\cdot\tilde{\boldsymbol{\sigma}} &= 2\tilde{\mu}(s)\left(\tfrac{1}{2}\left[\nabla\cdot\nabla\tilde{\vec{u}} + \nabla\nabla\cdot\tilde{\vec{u}}\right]\right) = \tilde{\mu}(s)\left[\nabla\cdot\nabla\tilde{\vec{u}}\right] \\
&= \tilde{\mu}(s)\textstyle\sum_{nm}\left(\tilde{U}''_{nm} + \frac{2\tilde{U}'_{nm}}{r} - \frac{(N+2)\tilde{U}_{nm}+2N\tilde{V}_{nm}}{r^2}\right)\vec{S}^{(-1)}_{nm} + \\
&\quad \tilde{\mu}(s)\textstyle\sum_{nm}\left(\tilde{V}''_{nm} + \frac{2\tilde{V}'_{nm}}{r} + \frac{2\tilde{U}_{nm}-N\tilde{V}_{nm}}{r^2}\right)\vec{S}^{(1)}_{nm} + \\
&\quad \tilde{\mu}(s)\textstyle\sum_{nm}\left(\tilde{W}''_{nm} + \frac{2\tilde{W}'_{nm}}{r} - \frac{N\tilde{W}_{nm}}{r^2}\right)\vec{S}^{(0)}_{nm}
\end{aligned} \tag{3.44}$$

where $N = n(n+1)$ and the prime $'$ indicates the derivative with respect to radius r. Note, this means that $\nabla\cdot\tilde{\boldsymbol{\sigma}}$ is already split into a spheroidal and a toroidal part because $\vec{S}^{(i)}$ are the bases of this separation. After inserting equation (3.34) and the three elements of the first row of the stress tensor $\tilde{\boldsymbol{\sigma}}$ (equation 3.42) without the summation and spherical harmonics notation:

$$\tilde{\sigma}_{rr,nm} = 2\tilde{\mu}\tilde{U}'_{nm} \tag{3.45}$$

$$\tilde{\sigma}_{r\theta,nm} = \tilde{\mu}\left(\tilde{V}'_{nm} + \frac{\tilde{U}_{nm} - \tilde{V}_{nm}}{r}\right) \tag{3.46}$$

$$\tilde{\sigma}_{r\phi,nm} = \tilde{\mu}\left(\tilde{W}'_{nm} - \frac{\tilde{W}_{nm}}{r}\right) \tag{3.47}$$

equation (3.44) can be rewritten as:

$$\begin{aligned}
\nabla\cdot\tilde{\boldsymbol{\sigma}} = &\textstyle\sum_{nm}\left(\tilde{\sigma}'_{rr,nm} - \frac{12\tilde{\mu}}{r^2}\tilde{U}_{nm} + \frac{6N\tilde{\mu}}{r^2}\tilde{V}_{nm} - \frac{N}{r}\tilde{\sigma}_{r\theta,nm}\right)\vec{S}^{(-1)}_{nm} + \\
&\textstyle\sum_{nm}\left(\tilde{\sigma}'_{r\theta,nm} - \frac{6\tilde{\mu}}{r^2}\tilde{U}_{nm} - \frac{2(2N-1)\tilde{\mu}}{r^2}\tilde{V}_{nm} + \frac{1}{r}\tilde{\sigma}_{rr,nm} + \frac{3}{r}\tilde{\sigma}_{r\theta,nm}\right)\vec{S}^{(1)}_{nm} + \\
&\textstyle\sum_{nm}\left(\tilde{\sigma}'_{r\phi} - \frac{(N-2)\tilde{\mu}}{r^2}\tilde{W}_{nm} + \frac{3}{r}\tilde{\sigma}_{r\phi,nm}\right)\vec{S}^{(0)}_{nm}
\end{aligned} \tag{3.48}$$

For the right-hand-side of the momentum equation (3.20) a similar expansion can be done by making use of the expanded displacement and gravitational fields, leading to:

$$\nabla\left(\tilde{\vec{u}}\cdot\rho_0 g_0 \hat{e}_r\right)+\rho_0\nabla\tilde{\phi}_1=\sum_{nm}\left[\rho_0\left(\tilde{\phi}'+g_0\tilde{U}'\right)\tilde{\vec{S}}_{nm}^{(-1)}+\rho_0\left(\frac{\tilde{\phi}}{r}+\frac{g_0\tilde{U}}{r}\right)\tilde{\vec{S}}_{nm}^{(1)}\right] \tag{3.49}$$

Combining equations (3.48) and (3.49) results in a full separation of the momentum equation into a spheroidal and toroidal component:

$$\tilde{\vec{S}}_{nm}^{(-1)}:\ \tilde{\sigma}'_{rr,nm}-\frac{12\tilde{\mu}}{r^2}\tilde{U}_{nm}+\frac{6N\tilde{\mu}}{r^2}\tilde{V}_{nm}-\frac{N}{r}\tilde{\sigma}_{r\theta,nm}=\rho_0\left(\tilde{\phi}'+g_0\tilde{U}'\right) \tag{3.50}$$

$$\tilde{\vec{S}}_{nm}^{(1)}:\ \tilde{\sigma}'_{r\theta,nm}-\frac{6\tilde{\mu}}{r^2}\tilde{U}_{nm}-\frac{2(2N-1)\tilde{\mu}}{r^2}\tilde{V}_{nm}+\frac{1}{r}\tilde{\sigma}_{rr,nm}+\frac{3}{r}\tilde{\sigma}_{r\theta,nm}=\rho_0\left(\frac{\tilde{\phi}}{r}+\frac{g_0\tilde{U}}{r}\right) \tag{3.51}$$

$$\tilde{\vec{S}}_{nm}^{(0)}:\ \tilde{\sigma}'_{r\phi,nm}-\frac{(N-2)\tilde{\mu}}{r^2}\tilde{W}_{nm}+\frac{3}{r}\tilde{\sigma}_{r\phi,nm}=0 \tag{3.52}$$

The gravity acceleration g_0 is given by the relation $g_0\hat{e}_r = \nabla\phi_0$ and is assumed to be constant in every layer. It can thus be rewritten by inserting the Poisson equation (3.10):

$$2\frac{g_0}{r} = 4\pi G\rho_0. \tag{3.53}$$

Equation (3.50) can then be rewritten by inserting equations (3.34), (3.36) and (3.53) as follows:

$$\tilde{\sigma}'_{rr,nm}-\frac{12\tilde{\mu}}{r^2}\tilde{U}_{nm}+\frac{6N\tilde{\mu}}{r^2}\tilde{V}_{nm}-\frac{N}{r}\tilde{\sigma}_{r\theta,nm}=\rho_0\left(\tilde{Q}_{nm}-\frac{n+1}{r}\tilde{\phi}_{nm}-2\frac{g_0}{r}\tilde{U}_{nm}-g_0\frac{2\tilde{U}_{nm}+N\tilde{V}_{nm}}{r}\right) \tag{3.54}$$

Now all five basic equations are spherical harmonically expanded, resulting in several ordinary differential equations. Furthermore, the equations are decoupled into spheroidal and toroidal based equations. In the next section the equations will be re-arranged and written as two solvable sets of equations based on the spheroidal and toroidal separation.

3.3 Ordinary differential equations

3.3.1 Spheroidal components

In the previous section it was described how the basic equations (3.20-3.24) can be decoupled into a spheroidal and a toroidal component and written as ordinary differential equations. A closer look at Section (3.2) reveals that for the spheroidal component all the equations are written as a function of six components. These components define the vector $\tilde{\vec{y}}_{nm}$ as:

$$\tilde{\vec{y}}_{nm} = \left[\tilde{U}_{nm}, \tilde{V}_{nm}, \tilde{\sigma}_{rr,nm}, \tilde{\sigma}_{r\theta,nm}, \tilde{\phi}_{nm}\tilde{Q}_{nm}\right]^T \tag{3.55}$$

This vector can then be used to rewrite equations (3.34), (3.36), (3.38), (3.46), (3.51) and (3.54) in a reduced form:

$$\frac{d\tilde{\vec{y}}_{nm}(r,s)}{dr} = \tilde{\boldsymbol{S}}_n(r,s)\cdot\tilde{\vec{y}}_{nm}(r,s) \tag{3.56}$$

where $\tilde{\boldsymbol{S}}_n(r,s)$ is a 6x6 matrix given by:

$$\tilde{\boldsymbol{S}}_n(r,s) = \begin{bmatrix} -\frac{2}{r} & \frac{N}{r} & 0 & 0 & 0 & 0 \\ -\frac{1}{r} & \frac{1}{r} & 0 & \frac{1}{\tilde{\mu}} & 0 & 0 \\ \frac{12\tilde{\mu}}{r^2}-\frac{4g\rho}{r} & -\frac{6N\tilde{\mu}}{r^2}+\frac{Ng\rho}{r} & 0 & \frac{N}{r} & -\frac{(n+1)\rho}{r} & \rho \\ -\frac{6\tilde{\mu}}{r^2}+\frac{g\rho}{r} & \frac{2\left(2n^2+2n-1\right)\tilde{\mu}}{r^2} & -\frac{1}{r} & -\frac{3}{r} & \frac{\rho}{r} & 0 \\ -4\pi G\rho & 0 & 0 & 0 & -\frac{(n+1)}{r} & 1 \\ -4\pi G\frac{(n+1)\rho}{r} & 4\pi G\frac{N\rho}{r} & 0 & 0 & 0 & \frac{(n-1)}{r} \end{bmatrix}. \tag{3.57}$$

Note that the subscript 0, that denotes the initial condition, is disregarded. This relation is correct for all the layers of the Earth with exception of layer N_s where the internal loading applies. The solution for that layer is discussed later in this section. For every other layer (i) with constant material parameters and constant internal gravity, equation (3.56) can be solved into:

$$\tilde{\vec{y}}_{nm}^{(i)}(r,s) = \tilde{\boldsymbol{Y}}_n^{(i)}(r,s) \cdot \tilde{\vec{C}}_{nm}^{(i)}(r) \tag{3.58}$$

where every $\tilde{\vec{C}}_{nm}^{(i)}(r)$ is a vector of six integration constants and every $\tilde{\boldsymbol{Y}}_n^{(i)}(r,s)$ is a so-called fundamental matrix [*Vermeersen*, 2002b]:

$$\begin{bmatrix} \frac{nr^{n+1}}{2(2n+3)} & r^{n-1} & 0 & \frac{(n+1)r^{-n}}{2(2n-1)} & r^{-n-2} & 0 \\ \frac{(n+3)r^{n+1}}{2(2n+3)(n+1)} & \frac{r^{n-1}}{n} & 0 & \frac{(2-n)r^{-n}}{2n(2n-1)} & \frac{r^{-n-2}}{n+1)} & 0 \\ \frac{(n\rho gr+2(n^2-n-3)\tilde{\mu})r^n}{2(2n+3)} & (\rho gr+2(n-1)\tilde{\mu})r^{n-2} & \rho r^n & \frac{(n+1)\rho gr-2(n^2+3n-1)\tilde{\mu}}{2(2n-1)r^{n+1}} & \frac{\rho gr-2(n+2)\tilde{\mu}}{r^{n+3}} & \frac{\rho}{r^{n+1}} \\ \frac{n(n+2)\tilde{\mu}r^n}{(2n+3)(n+1)} & \frac{2(n-1)\tilde{\mu}r^{n-2}}{n} & 0 & \frac{(n^2-1)\tilde{\mu}}{n(2n-1)r^{n+1}} & \frac{2(n+2)\tilde{\mu}}{(n+1)r^{n+3}} & 0 \\ 0 & 0 & -r^n & 0 & 0 & \frac{1}{r^{n+1}} \\ \frac{2\pi G\rho nr^{n+1}}{2n+3} & 4\pi G\rho r^{n-1} & -(2n+1)r^{n-1} & \frac{2\pi G\rho(n+1)}{(2n-1)r^n} & \frac{4\pi G\rho}{r^{n+2}} & 0 \end{bmatrix} \tag{3.59}$$

The product of the fundamental matrix and the matrix with the integration constants would give the solution for each independent layer if the constants were known. This is however not the case, so another method for solving the system has been developed (Section 3.4) involving the inverse of the fundamental matrix:

$$\tilde{\boldsymbol{Y}}_n^{-1}(r,s) = \tilde{\boldsymbol{D}}_n(r)\tilde{\bar{\mathrm{Y}}}_n(r,s) \tag{3.60}$$

where $\tilde{\boldsymbol{D}}_n(r)$ is a diagonal matrix with the elements

$$diag(\tilde{\boldsymbol{D}}_n(r)) = \frac{1}{2n+1}\left(\frac{n+1}{r^{n+1}}, \frac{n(n+1)}{2(2n-1)r^{n-1}}, \frac{1}{r^{n-1}}, nr^n, \frac{n(n+1)}{2(2n+3)}r^{n+2}, -r^{n+1}\right) \tag{3.61}$$

and

$$\tilde{\bar{\mathrm{Y}}}_n(r,s) = \begin{bmatrix} \frac{\rho gr}{\tilde{\mu}}-2(n+2) & 2n(n+2) & \frac{r}{\tilde{\mu}} & \frac{nr}{\tilde{\mu}} & \frac{\rho r}{\tilde{\mu}} & 0 \\ -\frac{\rho gr}{\tilde{\mu}}+\frac{2(n^2+3n-1)}{n+1} & -2(n^2-1) & \frac{r}{\tilde{\mu}} & \frac{(2-n)r}{\tilde{\mu}} & \frac{\rho r}{\tilde{\mu}} & 0 \\ 4\pi G\rho & 0 & 0 & 0 & 0 & -1 \\ \frac{\rho gr}{\tilde{\mu}}+2(n-1) & 2(n^2-1) & \frac{r}{\tilde{\mu}} & \frac{(n+1)r}{\tilde{\mu}} & \frac{\rho r}{\tilde{\mu}} & 0 \\ \frac{\rho gr}{\tilde{\mu}}\,\frac{2(n^2-n-3)}{n} & -2n(n+2) & \frac{r}{\tilde{\mu}} & \frac{(n+3)r}{\tilde{\mu}} & \frac{\rho r}{\tilde{\mu}} & 0 \\ 4\pi G\rho r & 0 & 0 & 0 & 2n+1 & -r \end{bmatrix}. \tag{3.62}$$

For the layer N_s a forcing vector is added to equation (3.56) resulting in [*Piersanti, et. al.*, 1995]:

$$\frac{d\tilde{\vec{y}}_{nm}(r,s)}{dr} = \tilde{\boldsymbol{S}}_n(r,s) \cdot \tilde{\vec{y}}_{nm}(r,s) + \tilde{\vec{f}}_{nm} \tag{3.63}$$

The vector $\tilde{\vec{f}}_{nm}$ contains the spectral components of the spheroidal part of the body force. When assumed equivalent to a point dislocation characterized by an impulsive time-dependence, the vector can split be into two parts:

$$\tilde{\vec{f}}_{nm} = \tilde{\vec{f}}_{\delta,nm}\delta(r-r_s) + \tilde{\vec{f}}_{\delta',nm}\delta'(r-r_s) \tag{3.64}$$

proportional to the Dirac delta function $\delta(r-r_s)$ and to its radial derivative $\delta'(r-r_s)$, respectively. The radius at which the internal point dislocation is situated is represented by r_s. The components of the coefficients $\tilde{\vec{f}}_{\delta,nm}$ and $\tilde{\vec{f}}_{\delta',nm}$

are dependent of the source parameters (Tables 2.1 and 2.2) and are given in Appendix (B).

Equation (3.63) can be solved in a similar way as the homogeneous equation (3.56). The solution is actually a sum of the previous solution (equation 3.58) and the linearly independent heterogeneous solutions of equation (3.63) [*Piersanti, et. al.*, 1995]

$$\tilde{\vec{y}}_{nm}^{(N_s)}(r,s)=\begin{cases} \tilde{\boldsymbol{Y}}_n^{(N_s)}(r,s)\cdot\left[\tilde{\boldsymbol{Y}}_n^{(N_s)^{-1}}(r_s,s)\left(\boldsymbol{I}\tilde{\vec{f}}_{\delta,nm}+\tilde{\boldsymbol{S}}_n(r_s,s)\tilde{\vec{f}}_{\delta',nm}\right)+\tilde{\vec{C}}_{nm}^{(N_s)}(r)\right], & r_s\leq r\leq r_a; \\ \tilde{\boldsymbol{Y}}_n^{(N_s)}(r,s)\cdot\tilde{\vec{C}}_{nm}^{(N_s)}(r), & r_b\leq r<r_s; \end{cases} \tag{3.65}$$

where $\boldsymbol{I}$ is the identity matrix, and r_a and r_b are the top and bottom boundaries of the layer N_s, respectively. The fact that the solution for this layer depends on the position within, means that the normal and shear stress (third and fourth components in the vector $\tilde{\vec{y}}_{nm}(r,s)$) are not continuous when passing the point dislocation.

3.3.2 Toroidal components

Similar to the spheroidal component a system of equations can be written for the toroidal component:

$$\frac{d\tilde{\vec{z}}_{nm}(r,s)}{dr} = \tilde{\boldsymbol{T}}_n(r,s)\cdot\tilde{\vec{z}}_{nm}(r,s)+\tilde{\vec{g}}_{nm}. \tag{3.66}$$

In this case the system is based on equations (3.47) and (3.52). Both these equations are a function of $\tilde{W}_{nm}$ and $\tilde{\sigma}_{r\theta,nm}$ which are thus the components of the vector $\tilde{\vec{z}}_{nm}$:

$$\tilde{\vec{z}}_{nm}(r,s) = \left[\tilde{W}_{nm}, \tilde{\sigma}_{r\theta,nm}\right]^T. \tag{3.67}$$

The matrix $\tilde{\boldsymbol{T}}_n$ is given by:

$$\tilde{\boldsymbol{T}}_n = \begin{bmatrix} \frac{1}{r} & \frac{1}{\tilde{\mu}} \\ \frac{\tilde{\mu}(n(n+1)-2)}{r^2} & -\frac{3}{r} \end{bmatrix}. \tag{3.68}$$

The vector $\tilde{\vec{g}}_{nm}$ is similar to $\tilde{\vec{f}}_{nm}$ and represents the spectral components of the toroidal part of the body force equivalent to the point dislocation. It can also be split into two parts:

$$\tilde{\vec{g}}_{nm} = \tilde{\vec{g}}_{\delta,nm}\delta(r-r_s)+\tilde{\vec{g}}_{\delta',nm}\delta'(r-r_s) \tag{3.69}$$

The components of $\tilde{\vec{g}}_{\delta,nm}$ and $\tilde{\vec{g}}_{\delta',nm}$ may be found in Appendix (B). The vector $\tilde{\vec{g}}_{\delta,nm}$ is zero for all layers except layer N_s and therefore the solution of all other layers is equal to the homogeneous solution of equation (3.66).

A fundamental matrix $\tilde{\boldsymbol{Z}}_n$ can be found assuming that the components of $\tilde{\vec{z}}_{nm}$ are of the form [*Piersanti, et. al.*, 1995]

$$\begin{aligned} \tilde{z}_{1,nm} &= r^{n+k} \\ \tilde{z}_{2,nm} &= a(n)\tilde{\mu}r^{n+k-1} \end{aligned}. \tag{3.70}$$

Inserting them into equation (3.66), results in a solution for the unknown a(n) and k:

$$\begin{array}{c} a(n) = n+k-1 \\ k=0 \quad or \quad k=-(2n+1) \end{array}. \tag{3.71}$$

The fundamental matrix $\tilde{\boldsymbol{Z}}_n$ can therefore be written as:

$$\tilde{\boldsymbol{Z}}_n(r,s) = \begin{bmatrix} r^n & r^{-n-1} \\ \tilde{\mu}(n-1)r^{n-1} & -\tilde{\mu}(n+2)r^{-n-2} \end{bmatrix} \tag{3.72}$$

whose inverse is:

$$\tilde{\boldsymbol{Z}}_n^{-1}(r,s) = \frac{1}{\tilde{\mu}(2n+1)} \begin{bmatrix} \tilde{\mu}(n+2)r^{-n} & r^{-n+1} \\ \tilde{\mu}(n-1)r^{n+1} & -r^{n+2} \end{bmatrix}. \tag{3.73}$$

The solution of equation (3.66) is given by:

$$\tilde{\vec{z}}_{nm}(r,s) = \tilde{\boldsymbol{Z}}_n(r,s) \cdot \tilde{\vec{K}}_{nm}(r), \tag{3.74}$$

where $\tilde{\vec{K}}_{nm}(r)$ is the vector of unknown integration constants.

The heterogeneous solution is again only valid for the layer N_s and is given by:

$$\tilde{\vec{z}}_{nm}^{(N_s)}(r,s) = \begin{cases} \tilde{\boldsymbol{Z}}_n^{(N_s)}(r,s) \cdot \left[\tilde{\boldsymbol{Z}}_n^{(N_s)^{-1}}(r_s,s) \left(\boldsymbol{I}\tilde{\vec{g}}_{\delta,nm} + \tilde{\boldsymbol{W}}_n(r_s,s)\tilde{\vec{g}}_{\delta',nm} \right) + \tilde{\vec{K}}_{nm}^{(N_s)}(r) \right], & r_s \leq r \leq r_a; \\ \tilde{\boldsymbol{Z}}_n^{(N_s)}(r,s) \cdot \tilde{\vec{K}}_{nm}^{(N_s)}(r), & r_b \leq r < r_s; \end{cases} \tag{3.75}$$

3.4 Propagator matrix technique

In Section (3.3) two solution vectors were derived: one for the spherical and one for the toroidal part. Equation (3.58) gives for each layer the most general solution for all the components of the vector $\tilde{\vec{y}}_{nm}(r,s)$. It is actually the sum of several linearly independent solution for each harmonic degree n and order m in the Laplace domain. Equation (3.67) does the same for vector $\tilde{\vec{z}}_{nm}(r,s)$. However, the relations are not always correct. As stated before, for the layer N_s at which the internal loading applies, the solution vector $\tilde{\vec{y}}_{nm}(r,s)$ is given by equation (3.65), while equation (3.75) gives the solution vector $\tilde{\vec{z}}_{nm}(r,s)$.

In this section, these solutions of the separate layers will be combined to find one vector solution at the Earth's surface for both the spheroidal and the toroidal component. In order to do so, boundary conditions at the surface, the Core-Mantle Boundary and between internal layers should be discerned.

3.4.1 Boundary Conditions

Figure (3.1) shows that every layer is bounded y two layers. Layers (2) to (N-2) are bounded by two other internal layers and layer (1) and layer (N-1) by only one. The latter two are also bounded by respectively the free outer surface and layer (N), the in-viscid outer core which is also seen as an external layer. For each of these boundaries, conditions are determined below.

At the surface the deformations $\tilde{U}_{nm}$, $\tilde{V}_{nm}$, $\tilde{W}_{nm}$ as well as the potential field $\tilde{\phi}_{nm}$ are the unknown quantities. It is required that the stresses $\tilde{\sigma}_{rr,nm}$, $\tilde{\sigma}_{r\theta,nm}$ and $\tilde{\sigma}_{r\phi,nm}$ are zero because there is no force to balance them (equation 3.1). To clarify why the potential stress $\tilde{Q}_{nm}$ was chosen as a component of the spheroidal solutions vector the following should be considered. If $\tilde{\phi}_{nm}^{(e)}$ is the gravity potential of the external layer the condition for the free surface can be written as [*Vermeersen*, 2002b]:

$$\frac{\partial \tilde{\phi}_{nm}^{(e)}}{\partial r} - \frac{\partial \tilde{\phi}_{nm}^{(1)}}{\partial r} = 4\pi G \rho \tilde{U}_{nm}. \tag{3.76}$$

Combining this relation with:

$$\frac{\partial \tilde{\phi}_{nm}^{(e)}}{\partial r} = -\frac{n+1}{r}\tilde{\phi}_{nm}^{(e)} \tag{3.77}$$

and the fact that at the surface:

$$\tilde{\phi}_{nm}^{(e)} = \tilde{\phi}_{nm}^{(1)} \tag{3.78}$$

results in:

$$\tilde{Q}_{nm} = \frac{d\tilde{\phi}_{nm}}{dr} + \frac{n+1}{r}\tilde{\phi}_{nm} + 4\pi G\rho\tilde{U}_{nm} = 0 \tag{3.79}$$

for the boundary between the top layer and the external layer.

This means that the boundary conditions at the surface can be summarized as:

$$\begin{array}{l} \tilde{y}_{3,nm}^{(1)} = \tilde{y}_{4,nm}^{(1)} = \tilde{y}_{6,nm}^{(1)} = 0 \\ \tilde{z}_{2,nm}^{(1)} = 0 \end{array} \tag{3.80}$$

where $\tilde{y}_{i,nm}^{(1)}$ and $\tilde{z}_{i,nm}^{(1)}$ are the i-th components of the vectors $\tilde{\vec{y}}_{nm}^{(1)}$ and $\tilde{\vec{z}}_{nm}^{(1)}$.

The internal boundaries are all considered to be chemical boundaries. This means that it is assumed that no material can cross the boundary. Furthermore it is required that all displacements, stresses and the gravity field are continuous over the boundaries. Relation (3.79) already made it clear that this is also valid for the potential stress. So there will be no 'cavitation' or slip. This implies that at every internal boundary the solutions of both adjoining layers should be equal, for $i = 1...N-1$:

$$\begin{array}{l} \tilde{\vec{y}}_{nm}^{(i)}(r_{i+1}, s) = \tilde{\vec{y}}_{nm}^{(i+1)}(r_{i+1}, s) \\ \tilde{\vec{z}}_{nm}^{(i)}(r_{i+1}, s) = \tilde{\vec{z}}_{nm}^{(i+1)}(r_{i+1}, s) \end{array} \tag{3.81}$$

The second external boundary is the boundary between the core and the last layer of the mantle and is often referred to as the Core-Mantle Boundary (CMB). The conditions there have been a point of discussion for a long time among geophysicists and are outside the range of interest of this report. So without going into further detail it is stated that [*Vermeersen*, 2002b]:

$$\begin{array}{l} \tilde{\vec{y}}_{nm}^{(N)}(r_c, s) = \boldsymbol{Y}_n^{(N)}(r_c, s) \cdot \tilde{\vec{C}}_{nm}^{(N)}(r_c) = \boldsymbol{I}_{S,nm}(r_c) \cdot \vec{C}_c \\ \tilde{\vec{z}}_{nm}^{(N)}(r_c, s) = \boldsymbol{Z}_n^{(N)}(r_c, s) \cdot \tilde{\vec{K}}_{nm}^{(N)}(r_c) = \boldsymbol{I}_{T,nm}(r_c) k_c \end{array} \tag{3.82}$$

where $\vec{C}_c = (C_1, C_2, C_3)$ is a vector of three constants and $k_c = \tilde{\vec{K}}_{2,nm}^{(N)}(r_c)$ is a single constant. The matrices $\boldsymbol{I}_{S,nm}(r_c)$ and $\boldsymbol{I}_{T,nm}(r_c)$ are respectively given by:

$$\boldsymbol{I}_{S,nm}(r_c) = \begin{bmatrix} \frac{3r_c^{(n-1)}}{4\pi G\rho_c} & 0 & 1 \\ 0 & 1 & 0 \\ 0 & 0 & \frac{4}{3}\pi G\rho_c^2 r_c \\ 0 & 0 & 0 \\ r_c^l & 0 & 0 \\ 2(l-1)r_c^{n-1} & 0 & 4\pi G\rho_c \end{bmatrix} \tag{3.83}$$

and

$$\boldsymbol{I}_{T,nm}(r_c) = \begin{bmatrix} \frac{n-1}{n+2} r_c^{3n+1} + r_c^{-n-1} \\ 0 \end{bmatrix}. \tag{3.84}$$

where ρ_c is the uniform density of the core. Now all the information necessary is available for finding both a spheroidal and a toroidal solution.

3.4.2 Solution of the spheroidal equations

For every layer $i = 1...N$ one solution exists (equations 3.58 and 3.65):

$$\begin{array}{lll} \tilde{\vec{y}}_{nm}^{(N_s)}(r_i,s) = \tilde{\boldsymbol{Y}}_n^{(N_s)}(r,s)\cdot\left[\tilde{\boldsymbol{Y}}_n^{(N_s)^{-1}}(r_s,s)\tilde{\vec{b}}_{f,n}+\tilde{\vec{C}}_{nm}^{(N_s)}(r_i)\right] & r_s\le r_i\le r_{N_s} \\ \tilde{\vec{y}}_{nm}^{(i)}(r_i,s) = \tilde{\boldsymbol{Y}}_n^{(i)}(r_i,s)\cdot\tilde{\vec{C}}_{nm}^{(i)}(r_i) & else \end{array} \quad (3.85)$$

where

$$\tilde{\vec{b}}_{f,n} = \left(\boldsymbol{I}\tilde{\vec{f}}_{\delta,nm} + \tilde{\boldsymbol{S}}_n(r_s,s)\tilde{\vec{f}}_{\delta',nm}\right)$$

is the loading vector for the spheroidal part. Using the internal boundary condition (equation 3.81) every unknown vector of constants $\tilde{\vec{C}}_{nm}^{(i)}(r_i)$, for $i = 1..N-1$, can be written as a function of the propagation matrices and the vector of constants of the next layer:

$$\begin{array}{lll} \tilde{\vec{C}}_{nm}^{(i-1)}(r_{i-1}) = \tilde{\boldsymbol{Y}}_n^{(i-1)^{-1}}(r_i,s)\tilde{\boldsymbol{Y}}_n^{(i)}(r_i,s)\left[\tilde{\boldsymbol{Y}}_n^{(i)^{-1}}(r_s,s)\tilde{\vec{b}}_{f,n}+\tilde{\vec{C}}_{nm}^{(i)}(r_i)\right] & i=N_s \\ \tilde{\vec{C}}_{nm}^{(i-1)}(r_{i-1}) = \tilde{\boldsymbol{Y}}_n^{(i-1)^{-1}}(r_i,s)\tilde{\boldsymbol{Y}}_n^{(i)}(r_i,s)\tilde{\vec{C}}_{nm}^{(i)}(r_i) & else \end{array}. \quad (3.86)$$

Starting with the solution vector at the surface (equation 3.58 for $i = 1$) and inserting all the $N-1$ equations (3.86) results in:

$$\tilde{\vec{y}}_{nm}^{(1)}(r_1,s) = \tilde{\boldsymbol{A}}_n\tilde{\boldsymbol{Y}}_n^{(N_s)^{-1}}(r_s,s)\tilde{\vec{b}}_{f,n} + \tilde{\boldsymbol{B}}_n\tilde{\boldsymbol{Y}}_n^{(N)}(r_c,s)\tilde{\vec{C}}_{nm}^{(N)}(r_c) \quad (3.87)$$

with

$$\tilde{\boldsymbol{A}}_n = \left(\prod_{i=1}^{N_s-1}\tilde{\boldsymbol{Y}}_n^{(i)}(r_i,s)\tilde{\boldsymbol{Y}}_n^{(i)^{-1}}(r_{i+1},s)\right)\tilde{\boldsymbol{Y}}_n^{(N_s)}(r_{N_s},s) \quad (3.88)$$

$$\tilde{\boldsymbol{B}}_n = \prod_{i=1}^{N-1}\tilde{\boldsymbol{Y}}_n^{(i)}(r_i,s)\tilde{\boldsymbol{Y}}_n^{(i)^{-1}}(r_{i+1},s). \quad (3.89)$$

The last two terms on the right-hand-side of equation (3.87) can be rewritten using the boundary condition at the CMB (equation 3.82). This means that the solutions at the surface are now a function of only three unknowns, the components of the vector $\vec{C}_c$. This vector can be solved using the boundary conditions at the surface (equation 3.80). After these boundary conditions are used to define two projection operators $\boldsymbol{P}_1$ and $\boldsymbol{P}_2$ as:

$$\boldsymbol{P}_1\tilde{\vec{y}}_{nm}^{(1)}(r_1,s) = \left[\tilde{y}_{3,nm}^{(1)}, \tilde{y}_{4,nm}^{(1)}, \tilde{y}_{6,nm}^{(1)}\right]^T = [0,0,0]^T \quad (3.90)$$

$$\boldsymbol{P}_2\tilde{\vec{y}}_{nm}^{(1)}(r_1,s) = \left[\tilde{y}_{1,nm}^{(1)}, \tilde{y}_{2,nm}^{(1)}, \tilde{y}_{5,nm}^{(1)}\right]^T = \vec{S}_{S,n}(R,s). \quad (3.91)$$

A combination of equations (3.82), (3.87) and (3.90) results in the following solution for the vector $\vec{C}_c$:

$$\vec{C}_c = -\left[\boldsymbol{P}_1\tilde{\boldsymbol{B}}_n\boldsymbol{I}_{S,nm}(r_c)\right]^{-1}\boldsymbol{P}_1\tilde{\boldsymbol{A}}_n\tilde{\boldsymbol{Y}}_n^{(N_s)^{-1}}(r_s,s)\tilde{\vec{b}}_{f,n}, \quad (3.92)$$

which is inserted together with equation (3.91) into equation (3.87) to result into a solution of the unknown quantities at the Earth's surface $\vec{S}_{S,n}(R,s)$:

$$\vec{S}_{S,n}(R,s) = \left[\boldsymbol{P}_2 - \boldsymbol{G}_2\boldsymbol{G}_1^{-1}\boldsymbol{P}_1\right]\tilde{\boldsymbol{A}}_n\tilde{\boldsymbol{Y}}_n^{(N_s)^{-1}}(r_s,s)\tilde{\vec{b}}_{f,n} \quad (3.93)$$

with $\boldsymbol{G}_1$ and $\boldsymbol{G}_2$ 3x3 matrices given as:

$$\boldsymbol{G}_k = \boldsymbol{P}_k \tilde{\boldsymbol{B}}_n \boldsymbol{I}_{S,nm}(r_c) \qquad , for \quad (k = 1, 2) \tag{3.94}$$

The solution can be simplified by rewriting the inverse matrix $\boldsymbol{G}_1^{-1}$ as [*Lay*, 1998]

$$\boldsymbol{G}_1^{-1} = \frac{\boldsymbol{G}_1^{\dagger}}{\mathscr{G}(s)}, \tag{3.95}$$

to

$$\vec{S}_{S,n}(R,s) = \left[\frac{\boldsymbol{P}_2 \mathscr{G}(s) - \boldsymbol{G}_2 \boldsymbol{G}_1^{\dagger} \boldsymbol{P}_1}{\mathscr{G}(s)} \right] \tilde{\boldsymbol{A}}_n \tilde{\boldsymbol{Y}}_n^{(N_s)^{-1}}(r_s, s) \tilde{\vec{b}}_{f,n} \tag{3.96}$$

where $\boldsymbol{G}_1^{\dagger}$ is the transpose of the matrix of minors of $\boldsymbol{G}_1$ and $\mathscr{G}(s)$ its determinant. Both these quantities are easier to calculate for a 3x3 matrix than its inverse.

After a closer inspection of the algebraic structure of the matrix $\boldsymbol{G}_1$ (3.94) some conclusions can be made. The determinant $\mathscr{G}(s)$ is a polynomial of the Laplace variable s. The degree M of the polynomial depends on the rheological and density stratification of the chosen model. Furthermore the matrix is independent of any displacements or forces applied to the model, so that the M solutions s_j of the so-called spheroidal secular equation:

$$\mathscr{G}(s) = 0 \tag{3.97}$$

are the same as in the post-glacial studies. This means that each of the components of the solution vector can be written as a fraction with a degree M polynomial in s in the numerator [*Vermeersen*, 2002b]. This structure makes it possible to use the *Residue Theorem* (see Appendix C) for the inverse Laplace transformation (equation 3.101) of equation (3.96) for each of the M solutions of s_j.

All these roots are actually inverse times and their negative inverses τ_j denote a set of relaxation times of the relaxation modes. The relaxation modes are customarily labeled according to the role played by the interface of each layer in the relaxation process [*Piersanti, et. al.*, 1995]. For spheroidal modes analytical proofs have shown that if the Earth would be modeled by a homogeneous sphere with Maxwell rheology a single mode M0 is triggered by the surface. This mode remains present in a model with several layers. If a core is present in the model a new mode C0 is introduced. This mode is for the deformation of the CMB. A boundary between an elastic lithosphere and viscoelastic mantle triggers another mode, labeled L0. These are the three modes that are present in the most basic Earth models (Section 2.1). Any two adjoined viscoelastic layers can trigger *buoyancy modes* if their densities are different. Buoyancy modes are usually labeled Mi, with $i = 1, 2, ...$ The most common are M1, the upper-lower mantle discontinuity at 670 km depth and M2, the shallow upper mantle - mantle transition zone at 400 km depth. In addition to those listed, modes are triggered if the *Maxwell times* η/μ of two adjoining viscoelastic layers are different. It that case two 'paired' modes called *transient modes* are introduced. They are commonly labeled Ti, with $i = 1, 2, ...$ It has been found that viscoelastic residues associated with these times are of lesser influence than the other modes listed above [*Vermeersen*, 2002b].

Note that these roots are functions of the degree n but the subscript is disregarded for simplicity. First the solution vector is written as the sum of an elastic term and M viscous terms:

$$\vec{S}_{S,n}(R,s) = \vec{S}^{e}_{S,n}(R) + \sum_{j=1}^{M} \frac{\vec{S}^{j}_{S,n}(R)}{s - s_j} \tag{3.98}$$

where $\vec{S}^{e}_{S,n}(R)$ are the elastic limits and $\vec{S}^{j}_{S,n}(R)$ the vector residues of the solution kernel vector $\tilde{\vec{y}}_{nm}(R,s)$. They are respectively given by:

$$\vec{S}^{e}_{S,n}(R) = \lim_{s\to\infty} \vec{S}_{S,n}(R,s) \tag{3.99}$$

$$\vec{S}^{j}_{S,n}(R) = -\left[\frac{\boldsymbol{G}_2\boldsymbol{G}_1^{\dagger}\boldsymbol{P}_1}{\frac{d}{ds}\mathscr{G}(s)}\right]\tilde{\boldsymbol{A}}_n\tilde{\boldsymbol{Y}}_n^{(N_s)^{-1}}(r_s,s)\tilde{\vec{b}}_{f,n} \tag{3.100}$$

The last step in determining the solution vector $\vec{S}_{S,n}(R,s)$ is inverse Laplace transformations. This method gives a solution as a function of time t. The inverse Laplace transformation is defined as [*Vermeersen*, 2002b]:

$$f(t) = \frac{1}{2\pi i}\int_{\gamma-i\infty}^{\gamma+i\infty}\tilde{F}(s)e^{st}ds \tag{3.101}$$

where γ is a constant chosen such that all the singularities of the function $\tilde{F}(s)e^{st}$ are on the same side of the line running trough $\gamma - i\infty$ and $\gamma + i\infty$. When these points are also connected by a half-circle, on the side where the singularities are positioned, a complex contour originates known as the *Bromwich path*. This makes that the inverse Laplace transformation can be applied to equation (3.98) and a solution can be found without even analytically knowing the primitive function [*Vermeersen*, 2002b]:

$$\vec{S}_{S,n}(R,t) = \vec{S}^{e}_{S,n}(R)\delta(t) + \sum_{j=1}^{M}\vec{S}^{j}_{S,n}(R)e^{s_j t} \tag{3.102}$$

Equation (3.102) shows that the solution in the time-domain dependents on the degree n and consist of two terms. The first term, the elastic term, describes part of the immediate response and equals zero for times larger then zero. The second term, the viscoelastic term, describes the M exponential components that contribute to the immediate response and give the postseismic viscous response. It is clear that the viscous response should decay over time which only happens when all the roots s_j are real and negative for each harmonic degree. If there is a positive root the response will increase exponentially over time and become infinitely large. This would be the case if the density of the layers increased with depth. Any density inversion would trigger convection motions in the Earth model and the assumed linearization breaks down [*Vermeersen*, 2002b].

3.4.3 Solution of toroidal equation

The time dependent solution for the toroidal component is found in a similar way as for the spheroidal component (Section 3.4.2). Equations (3.74) and (3.75) describe the general solution for each layer of the model. The vector of integration constants $\tilde{\vec{K}}_{nm}(r)$ can be eliminated by the use of the internal boundary condition (equation 3.81) and the boundary condition at the CMB (equation 3.82) to result into:

$$\tilde{z}^{(1)}_{nm}(R,s) = \tilde{\boldsymbol{E}}_n\tilde{\boldsymbol{Z}}_n^{(N_s)^{-1}}(r_s,s)\tilde{\vec{b}}_{g,n} + \tilde{\boldsymbol{F}}_n\boldsymbol{I}_{T,nm}(r_c)k_c \tag{3.103}$$

with

$$\tilde{\boldsymbol{E}}_n = \left(\prod_{i=1}^{N_s-1} \tilde{\boldsymbol{Z}}_n^{(i)}(r_i, s) \tilde{\boldsymbol{Z}}_n^{(i)^{-1}}(r_{i+1}, s) \right) \tilde{\boldsymbol{Z}}_n^{(N_s)}(r_{N_s}, s) \tag{3.104}$$

$$\tilde{\boldsymbol{F}}_n = \prod_{i=1}^{N-1} \tilde{\boldsymbol{Z}}_n^{(i)}(r_i, s) \tilde{\boldsymbol{Z}}_n^{(i)^{-1}}(r_{i+1}, s) \tag{3.105}$$

$$\tilde{\vec{b}}_{g,n} = \boldsymbol{I}\tilde{\vec{g}}_{\delta,nm} + \tilde{\boldsymbol{W}}_n(r_s, s)\tilde{\vec{g}}_{\delta',nm} \tag{3.106}$$

According to the boundary condition at the surface (equation 3.80) it possible to eliminate the last unknown constant k_c by introducing two 1x2 projection parameters $\boldsymbol{Q}_1$ and $\boldsymbol{Q}_2$ in such a way that:

$$\boldsymbol{Q}_1 \tilde{\vec{z}}^{(1)}_{nm}(R, s) = \tilde{z}^{(1)}_{2,nm} = 0 \tag{3.107}$$

$$\boldsymbol{Q}_2 \tilde{\vec{z}}^{(1)}_{nm}(R, s) = \tilde{z}^{(1)}_{1,nm} = S_{T,n}(R, s). \tag{3.108}$$

Similar as for the spheroidal solution the toroidal solution can now be written as:

$$S_{T,n}(R, s) = \left[\frac{\boldsymbol{Q}_2 H_1 - H_2 \boldsymbol{Q}_1}{H_1} \right] \tilde{\boldsymbol{E}}_n \tilde{\boldsymbol{Z}}_n^{(N_s)^{-1}}(r_s, s) \tilde{\vec{b}}_{g,n} \tag{3.109}$$

where

$$H_k = \boldsymbol{Q}_k \tilde{\boldsymbol{F}}_n \boldsymbol{I}_{T,nm}(r_c) \qquad , for \quad (k = 1, 2) \tag{3.110}$$

are two scalar functions in s. After inverse Laplace transformation (equation 3.101) the time dependent solution for the toroidal equations reads:

$$S_{T,n}(R, s) = S^e_{T,n}(R)\delta(t) + \sum_{j=1}^{K} S^j_{T,n}(R) e^{r_j t} \tag{3.111}$$

where $S^e_{T,n}(R)$ is the term that gives the elastic contribution and $S^j_{T,n}(R)$ are the associated viscoelastic residues. They are defined similarly to equations (3.99) and (3.100). The K solutions of the so-called toroidal secular equation

$$H_1 = 0 \tag{3.112}$$

are given by r_j. The toroidal roots have a similar connection to a set of relaxation modes as the spheroidal roots. Toroidal modes have, however, been proven to coincide with the number of viscoelastic layers in the model. So there will be less toroidal than spheroidal modes and therefore a lesser number of relaxation times. These rules make it possible to calculate in advance how many relaxation times are to be found by solving both the spheroidal and toroidal secular equation. This is important because the root-searching is the only non-analytic part of the calculation. This method ensures that the complete result is obtained after inverse Laplace transformation.

The final step is to insert all solutions $\tilde{U}_{nm}$, $\tilde{V}_{nm}$ and $\tilde{\phi}_{nm}$ from equation (3.102), and $\tilde{W}_{nm}$ from equation (3.111) into the spherical harmonic expansion of the total displacement $\tilde{\vec{u}}$ (equation 3.31) and gravitational field $\tilde{\phi}$ (equation 3.32).

Chapter 4
Earth models

It has been described how the Earth can be generally divided into several layers (Section 2.1) and how an earthquake is defined by parameters such as depth, magnitude and dip direction (Section 2.3). Chapter (3) then described how deformations and the gravity field at the Earth's surface can be calculated if the seismologic data is applied to a layered Earth model.

In this chapter all models used in the simulations are discussed. To begin, two original Earth models are introduced. A choice was made for one five- and one seven-layer model based on lithospheric strength measurements as performed in [*Lankreijer, et. al.*, 1997] (see Figure 4.1). These two models formed the initial concept upon which all other models were based. By continually changing one property of these base models several other models originated, all of which were simulated.

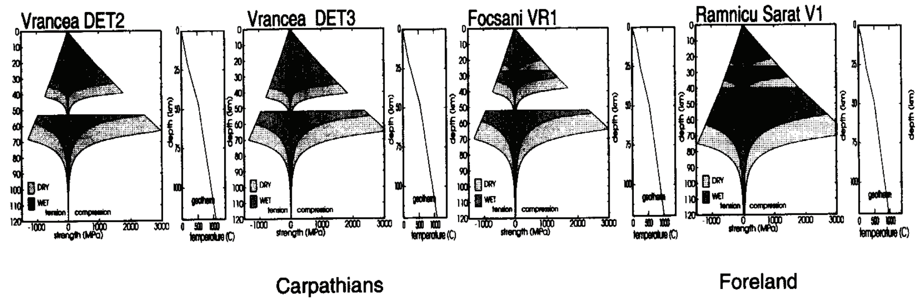

Figure 4.1 Strength profile of the lithosphere in the Vrancea area, [*Lankreijer, et. al.*,1998]

4.1 Five-layer model

In this section it is described how an Earth model was developed consisting of five layers. To calculate the deformations at the surface a constant value for the viscosity, density and shear modulus of each layer was required as was the position of every spheroidal boundary between the layers. The position of the layers was determined starting from the center of Earth (0 km) to the outermost boundary, the average Earth's surface (6731 km). Due to the need for constant values, average numbers were used for the three other properties. The density and the shear modulus were calculated using a general Earth model, developed using a considerable amount of seismological, data called *PREM* [*Dziewonski and Anderson*, 1981]. The viscosity of the layers could not be calculated. One can only

Table 4.1 Five-layer Earth model

Name	Upper Radius (km)	Viscosity (Pas)	Density (kg/m^3)	Shear modulus (Pa)
Lithosphere	6371	10^{50}	3028	5.23E10
Lithospheric mantle	6321	10^{22}	3378	6.76E10
Asthenosphere	6301	10^{19}	3374	6.61E10
Mantle	6221	10^{21}	4535	1.82E11
Core	3480	–	10932	–

use seismologic measurements or strength measurements from a certain area and even then only as indicators. However, it was known that in models, the upper-most layer is generally modeled as an elastic lithosphere and the lower-most layer as an inviscid core. All the numbers are summarized in Table (4.1). The inviscid core was modeled by means of its boundary conditions, thus only the parameters used to calculate them in the simulation (see equations 3.83 and 3.84) are given in the table.

As mentioned before this model was based on the findings as presented in Figure (4.1). It gives a lithospheric strength profile based on temperature distribution for a cross-section through the Vrancea region. All these graphs show a clear separation between a strong upper layer and another strong layer starting at a depth of 50 km. This latter layer ends at a depth of about 70 km to maximal 80 km. The exact depth is unclear because the figures show that there is quite a difference between the calculations based on a dry or a wet composition of the lithosphere. Here was chosen to take a 50 km thick lithosphere and a lithospheric mantle with a thickness of 20 km. The thickness of the asthenosphere was based on seismologic measurements [*Lankreijer, et. al.*, 1997], [*Chalot-Prat and Girbacea*, 2000] which all indicate a transition at a depth of about 150 km. The CMB was taken at its normal depth of about 2900 km.

The rest of the model parameters could not be derived from the lithospheric strength profile. The viscosities of all the layers were chosen as they were found most common in the literature where they were derived from postglacial rebound studies. The very high viscosity of the lithosphere does not make it totally elastic but it is a mathematical approach. It is so high that there was no effect noticeable in the postseismic calculation; it only played a part in the coseismic deformations. This lithospheric mantle is not elastic but again the viscosity is so high that the influence on the postseismic deformations within 30 years were small. The main effect probably comes from the asthenosphere which has a lower viscosity because it is made out of the same material as the lithospheric mantle but is positioned deeper inside the Earth, where temperatures are higher. A difference is that in the postglacial rebound studies the mantle usually is divided into an upper and lower mantle and a transition zone in between, with all different viscosities. In this five-layer model only one layer could be used for the mantle and a mean value for the viscosity was chosen.

Table 4.2 Seven-layer Earth model

Name	Upper Radius (km)	Viscosity ($Pa\ s$)	Density (kg/m^3)	Shear modulus (Pa)
Lithosphere	6371	10^{50}	3028	5.24E10
LVZ	6326	10^{18}	3379	6.78E10
Lithospheric mantle	6321	10^{22}	3378	6.77E10
Asthenosphere	6301	10^{19}	3374	6.61E10
Upper mantle	6221	5.10^{20}	3650	8.88E10
Lower mantle	5701	5.10^{21}	4878	2.19E11
Core	3480	–	10932	–

4.2 Seven-layer model

As stated before the graphs of the strength distribution (Figure 4.1) indicate several layers but it is hard to define the exact boundaries between them. It is even possible to say that in some parts of the cross-section of the Vrancea area there is a gap between the lithosphere and the lithospheric mantle. This gap between two layers, that are assumed to have high viscosities, coincides with a seismologically detectable low-viscosity-zone (LVZ) in the region [*Bazacliu and Radulian*, 1999], [*Bada, et. al.*, 1999]. By inserting a LVZ with a thickness of 5 km into the five-layer Earth model and separating the mantle into an upper and lower section, as found in the field of seismology, a seven-layer Earth model was obtained. All the properties of this model are given in Table (4.2).

It must be noted that the separation of the mantle makes the model more realistic according to the models used in postglacial studies but in Section (5.2.2) is will be shown that it hardly changes the outcome of the calculated postseismic deformation. And it was tested by comparing the results of a six-layer model, which is an exact copy of the five-layer model but with the mantle of the seven layered model, to the results of the five-layer Earth model. The viscosity used for the LVZ is not a measured value; it was chosen to equal 10^{18} Pa s because it is lower than the other values, but still realistic.

4.3 Variation applied to original models

The models presented in Sections (4.1) and (4.2) are not irrevocably correct for the Vrancea. Many uncertainties arise because of our limited knowledge of the Earth structure. That is the reason why several variations of the original Earth models were also simulated using the same mathematical approach.

It was assumed that the thickness and the elasticity of the lithosphere are correct. This is because the position of the Moho, which determines the thickness, is well known due to elaborative seismic research [*Gvirtzman*, 2002], [*Chalot-Prat and Girbacea*, 2000], [*Girbacea and Frisch*, 1998], and the lithosphere is generally assumed elastic. For similar reasons no variations were applied to the properties of the mantle and the core. This means that for the five-layer model the variation focused on the viscosity of the lithospheric mantle, the asthenosphere and on the

Table 4.3 Variation applied to five-layer Earth model

Varied property	Value
Lithosphere mantle viscosity	10^{20} - $\mathbf{10^{22}}$ - elastic
Asthenosphere viscosity	10^{17} - 10^{18} - $\mathbf{10^{19}}$ - 10^{20}
Depth of LMAB	50 km - **70 km** - 90 km - 110 km - 130 km

Table 4.4 Variation applied to seven-layer Earth model

Varied property	Value
LVZ viscosity	10^{17} - $\mathbf{10^{18}}$ - 10^{19} - elastic
Lithosphere mantle viscosity	10^{18} - 10^{20} - $\mathbf{10^{22}}$ - elastic
Asthenosphere viscosity	10^{18} - $\mathbf{10^{19}}$ - 10^{22}

position of the boundary between those two layers (LMAB) while the sum of their total thickness was maintained constant (see Table 4.3).

For the seven-layer Earth model variations were applied to the viscosity and the thickness of the low-viscosity zone and to the viscosity of the lithospheric mantle and asthenosphere (see Table 4.4). The bold symbols in both Tables (4.3) and (4.4) indicate the value of that property in the original model. Furthermore it is emphasized that the values in these tables are always the only property that was changed in comparison with the original model. This way it was possible to determine the influence on the postseismic surface displacements, each of the variation had. The results will be discussed in Chapter 5.

Chapter 5

Simulation results

In this chapter the results of the simulations of the Earth models as introduced in chapter (4) are discussed. Starting with the five-layer model and all the variations applied to it, a similar scenario for the seven-layer model follows. The figures in this chapter describe the average displacement change over the period from 2002 to 2006 of the Earth's surface, introduced by the three earthquakes given in the first three rows of Table (2.1). Velocities are given for an area between $20\,^\circ$ and $30\,^\circ$ longitude and between $43\,^\circ$ and $49\,^\circ$ latitude, thus containing the whole country of Romania.

5.1 Results for five-layer model

5.1.1 Original model

The results for the original model are presented in Figure (5.1) for the horizontal velocities and in Figure (5.2) for the vertical velocities. Both figures consist of four panels where $(\boldsymbol{a})$ gives the postseismic velocity for the 1977 event, $(\boldsymbol{b})$ for the 1986 event and $(\boldsymbol{c})$ for the 1990 earthquake. Part $(\boldsymbol{d})$ is in both cases the sum of the present-day velocities of all events.

An initial observation that can be made after studying Figures (5.1) and (5.2) is that both the horizontal and vertical velocity fields for each earthquake, are mirrored about the line through the epicenter and perpendicular to the strike direction. This is a result of the fact that the earthquakes were modeled as a point dislocation in a laterally homogeneous sphere. This mirroring condition is not preserved when the velocities of the earthquakes are added.

Considering the horizontal velocities, Figure (5.1) shows clearly that the 1977 and the 1986 events are the main contributors to the total displacement field. The surface velocity as a result of the 1990 earthquake is at least twice as small (see Table 5.1). Table (2.1) clarifies that this result is proportional to the magnitudes of considered the earthquakes. Also noticeable is the influence of the depth at which the earthquakes occurred. The 1977 and 1990 event were located close to the boundary between the lithospheric mantle and the asthenosphere while the 1986 event occurred rather close to the bottom of the asthenosphere, about 50 km deeper. This results in a point of no displacement near the epicenters from where the velocity vectors radially diverge and the presence of a relative large displacement in the north-western far field caused by the 1977 and 1990 earthquakes (see Figures 5.1.a and 5.1.c). Figure (5.1.b) shows that the 1986 event introduces al-

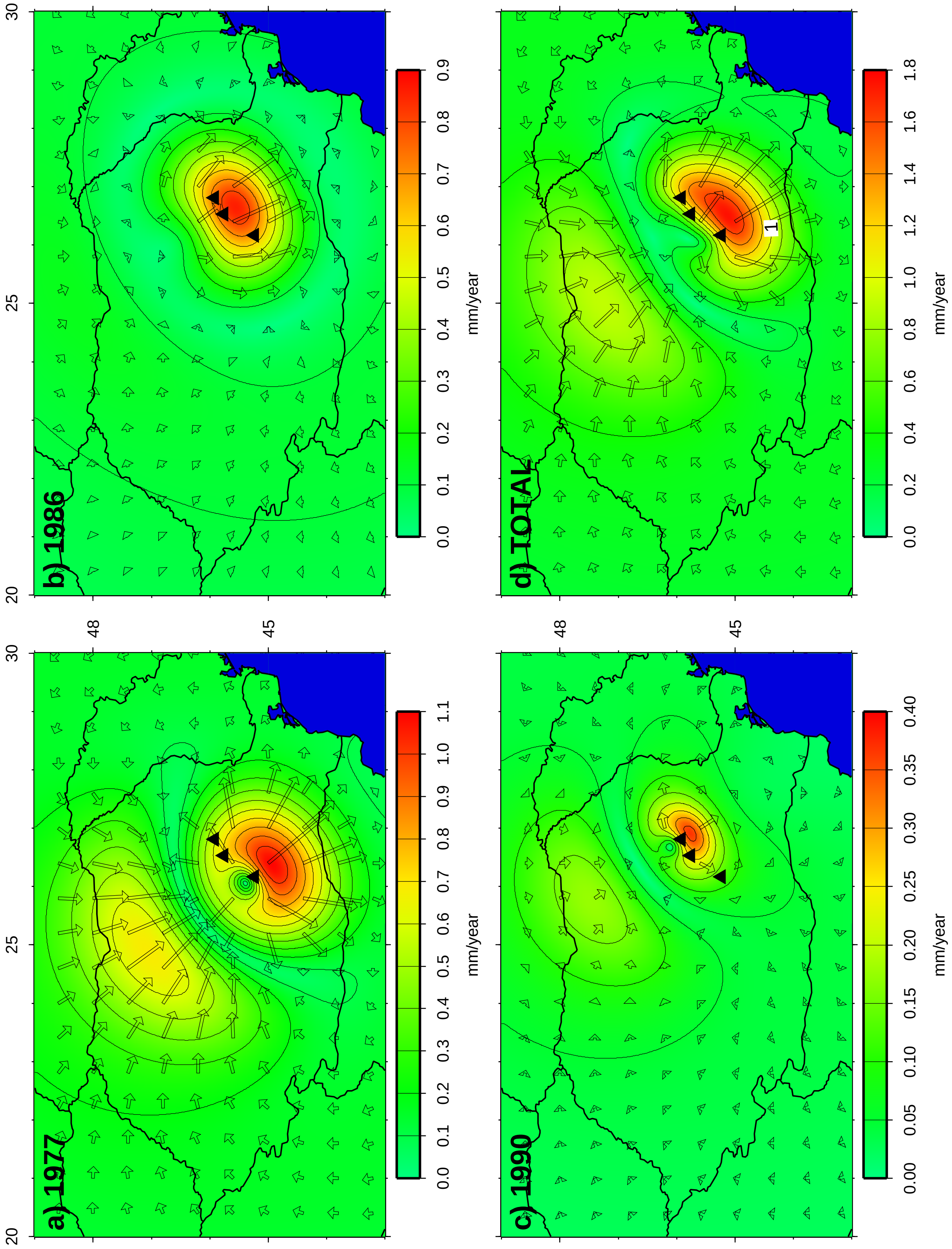

Figure 5.1 Average horizontal surface displacement change from 2002 to 2006 over Romania as result of three separate earthquakes (a-c) and their total (d). The 2-D locations of the earthquakes are indicated by a black triangle

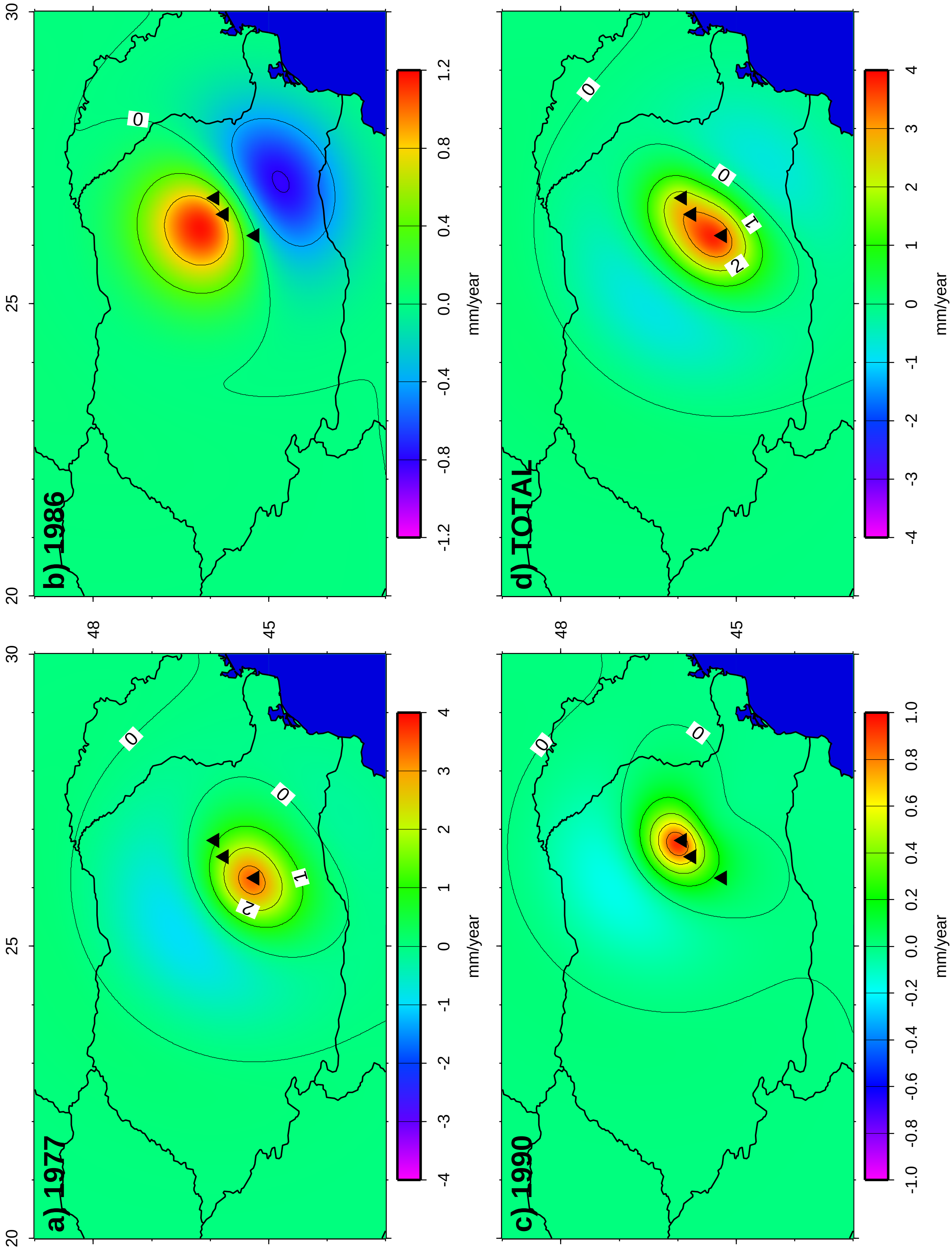

Figure 5.2 Average vertical surface displacement change from 2002 to 2006 over Romania as result of three separate earthquakes (a-c) and their total (d). The 2-D locations of the earthquakes are indicated by a black triangle

Table 5.1 Maximal velocities of the original five-layer model

	4-Mar-77 (mm/year)	30-Aug-86 (mm/year)	30-May-90 (mm/year)	Total (mm/year)
Max. horizontal velocity	1.09	0.86	0.37	1.76
Min. vertical velocity	-0.95	-0.82	-0.17	-0.77
Max. vertical velocity	3.39	1.17	0.94	3.81

most no movement in the far field and that the velocities close to the epicenter all point in roughly the same direction, the southeast.

This results for the total displacements (figure 5.1.d) in almost no displacement in the near field to the northwest of the earthquakes because there the velocity vectors of the 1977 and 1986 events are in opposite directions. In the southeast where the vectors of all earthquakes are in the same direction, the resulting vectors are almost twice as large as those of the isolated earthquakes (see Table 5.1).

Similar conclusions are made after studying the vertical displacements (see Figure 5.2). Again the 1977 (ranging from -0.95 to 3.39 mm/year) and the 1986 (ranging between -0.82 and 1.17 mm/year) earthquakes are responsible for the largest velocity in absolute numbers (see Table 5.1). The 1977 event is now clearly responsible for the largest vertical velocities when considering the positive maximum while the difference with respect to the 1986 event diminishes when considering the negative maximum. The influence of the depth of the earthquakes is that the location of the maxima of the velocities for the 1986 event is different in comparison to the location of the maxima of the velocities for the 1977 and 1990 earthquake. For the latter two the positive maximum is located at the epicenters. The negative maximum is about four times smaller in absolute numbers and is located to the northwest. For the 1986 event the epicenter lies in between the maximum and the minimum and the minimal vertical velocity is about two thirds of the maximum in absolute numbers.

This results into a relatively small maximum of 3.81 mm/year for the total velocity field (last column of Table 5.1). The combined maximal velocity is located in between the maxima of all three events and is only slightly larger than the maximal velocity of 3.39 mm/year caused by the 1977 event alone. The area with positive velocities is enclosed by two small minima, one to the northwest and one to the southeast. These minima are absolutely smaller then the minima of both the 1977 and 1986 earthquakes. All the maximal values caused by the separate earthquakes are partly balanced by an opposite maxima induced by another earthquake.

5.1.2 Varying model properties

Due to the uncertainties concerning several properties of the Earth model described in Section (4.1) the same simulation theory is applied to a series of Earth models where one parameter differs from the original model (see Table 4.3). This way the result of changing one property is discussed.

Table 5.2 Maximal horizontal velocity

LM viscosity (Pa s)	4-Mar-77 (mm/year)	30-Aug-86 (mm/year)	30-May-90 (mm/year)	Total (mm/year)
10^{20}	1.56	0.91	0.47	2.26
10^{22}	1.09	0.86	0.37	1.76
10^{50}	1.09	0.86	0.37	1.75

Lithospheric mantle viscosity

The postseismic velocities at the surface in all three directions are calculated for models with a lithospheric mantle (LM) viscosity of 10^{20}, 10^{22} and 10^{50} Pa s, where the latter is effectively elastic. These results are illustrated in Figure (5.3) for horizontal and in Figure (5.4) for vertical velocities. A first conclusion is that in both the horizontal and the vertical case the shape of the contours is independent of the viscosity but the scale in part ($\boldsymbol{a}$) is larger compared to part ($\boldsymbol{b}$) and ($\boldsymbol{c}$). This means that when the viscosity of the lithospheric mantle is increased starting from 10^{20} Pa s, the magnitude of the present horizontal and vertical velocity vectors will decrease while their direction stays unaltered. However, there is however a point from which this decline becomes minimal. This is as higher viscosities cause larger relaxation times. And as equations (3.102) and (3.111) show, the solution decreases exponentially with increasing relaxation time. These figures show that for a lithospheric mantle viscosity at least as high as 10^{22} Pa s no contribution to the total postseismic displacement is visible.

These conclusions are endorsed by the numbers in the last column of Tables (5.2) to (5.4) which respectively give the horizontal maximum and the vertical minimum and maximum for all three earthquakes separately and for the total. The tables also give an insight into the influence of the separate events to the total, but they do not describe the shape of the contours. What does stand out is that the 1977 event causes the largest maxima for all the displacements, followed by the 1986 event and then the 1990 earthquake. It also should be noticed that the maxima of the 1977 and the 1990 events experience the most influence from increasing the viscosity from 10^{20} to 10^{22} Pa s, while the effect on the velocities caused by the 1986 earthquake is minimal. This can be explained by the fact that the first two are positioned close to the lithospheric mantle, while the latter occurred at a greater depth. Furthermore it is clear that there is indeed only a small difference between a model with an elastic lithospheric mantle and one with a viscosity of 10^{22} Pa s when considering the maxima of the average displacements. The maximal horizontal velocities of the separate events are positioned closely to each other so that the total is almost the sum of the three. For the vertical velocities the total is not much larger than the maxima of the 1977 event and in the case of the minima, even smaller in absolute numbers. This suggests opposing maxima for the 1986 event with respect to the other two as described in Section (5.1.1). The general conclusion is that for this model the maximal velocities increase when the lithospheric mantle viscosity decreases.

Lithospheric mantle - Asthenosphere boundary

Next it is studied what happens when the boundary between the lithospheric mantle and the asthenosphere (LMAB) is shifted between 50 and 130 km depth

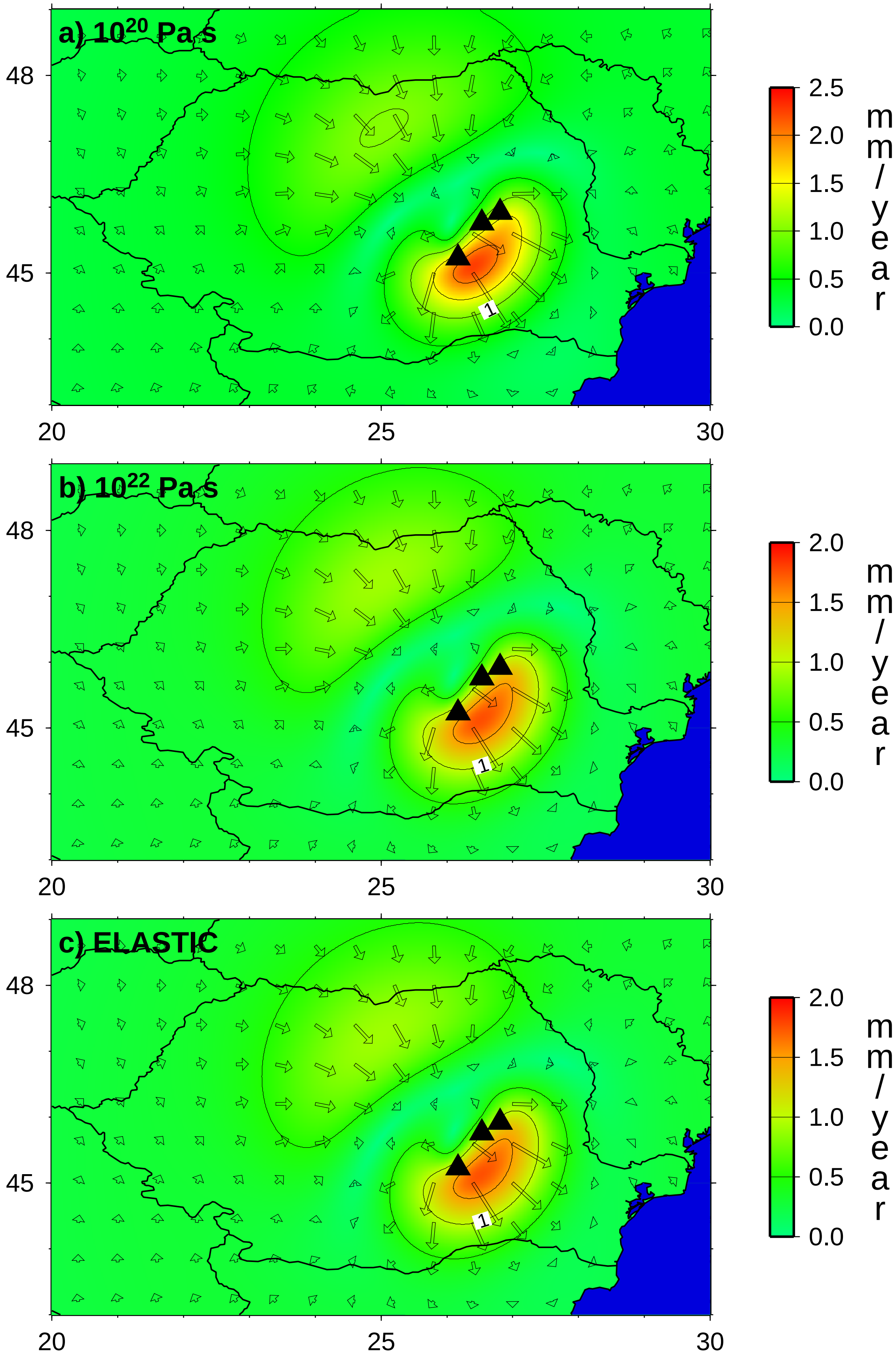

Figure 5.3 Average horizontal surface displacement change from 2002 to 2006 over Romania for an Earth model with varied lithospheric mantle viscosity. The 2-D locations of the earthquakes are indicated by a black triangle

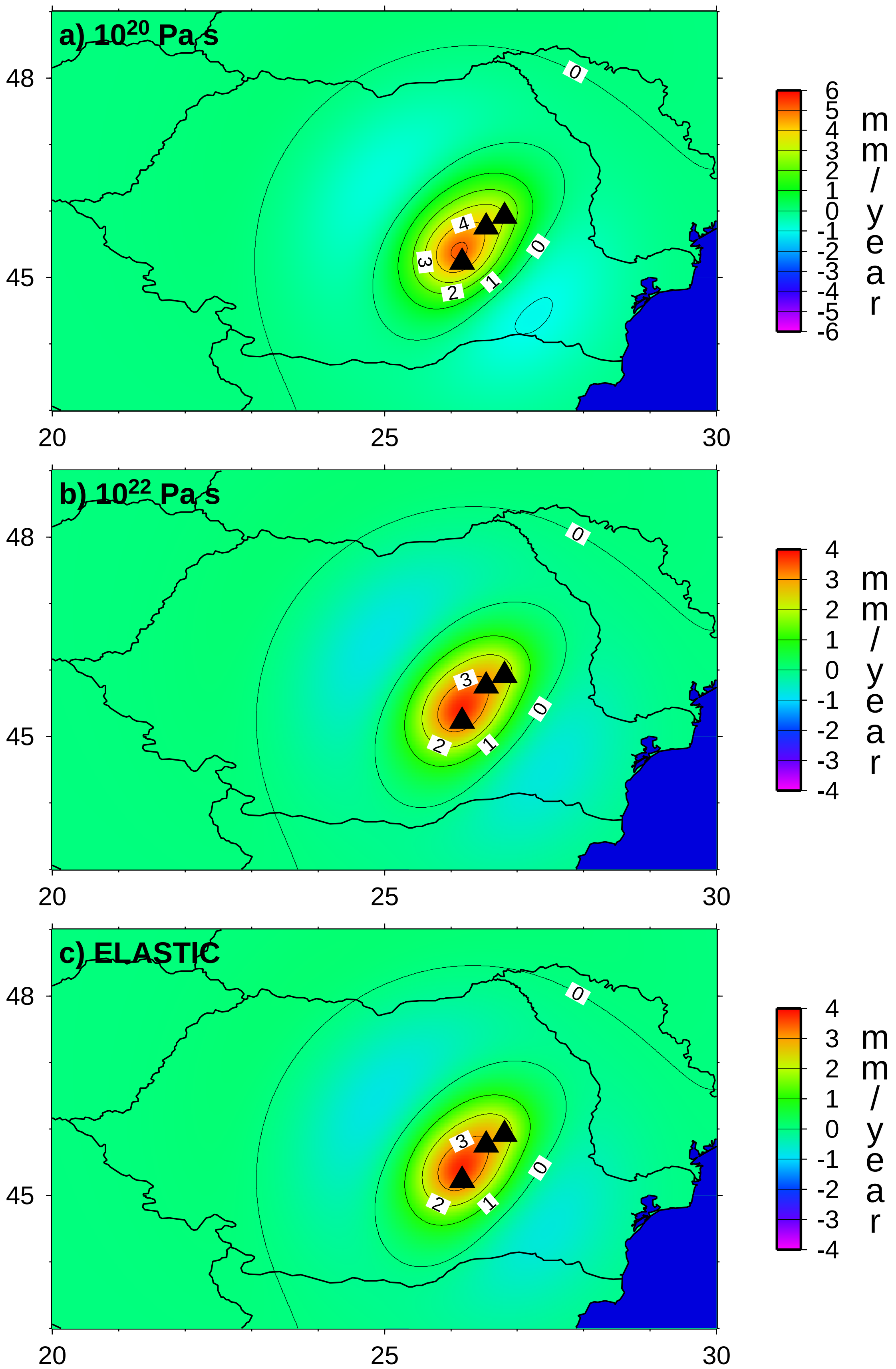

Figure 5.4 Average vertical surface displacement change from 2002 to 2006 over Romania for an Earth model with varied lithospheric mantle viscosity. The 2-D locations of the earthquakes are indicated by a black triangle

Table 5.3 Minimal vertical velocity

LM viscosity (Pa s)	4-Mar-77 (mm/year)	30-Aug-86 (mm/year)	30-May-90 (mm/year)	Total (mm/year)
10^{20}	-1.02	-0.86	-0.18	-1.05
10^{22}	-0.95	-0.82	-0.17	-0.77
10^{50}	-0.95	-0.82	-0.17	-0.77

Table 5.4 Maximal vertical velocity

LM viscosity (Pa s)	4-Mar-77 (mm/year)	30-Aug-86 (mm/year)	30-May-90 (mm/year)	Total (mm/year)
10^{20}	4.71	1.23	1.16	5.16
10^{22}	3.39	1.17	0.94	3.81
10^{50}	3.38	1.17	0.93	3.79

in steps of 20 km. This means that the thickness of the lithospheric mantle varies between 0 and 80 km and the thickness of the asthenosphere between 100 and 20 km. The situations with an LMAB depth of 50, 90 and 130 km are illustrated in Figures (5.5) and (5.6) for the horizontal and vertical displacement velocities, respectively. They show that both the horizontal and the vertical velocities drop significantly, from 2.91 mm/year to 0.74 mm/year, when a 40 km thick lithospheric mantle is inserted in the model and that the velocities drop even more, to 0.54 mm/year, after thickening it to 80 km. Figure (5.5) also illustrates that for the horizontal displacement field the contours near the epicenters shrink and transform from an ellipse to a circular shape. Furthermore the center of these contours shifts towards the northeast, the location of the maximum as a result of the 1986 earthquake, and the velocities in the northwestern far-field seems to vanish. From the results of the original model (Figure 5.1) it is known that this could mean that the influence of the 1977 and 1990 events on the total, is reduced by increasing the depth of the LMAB. This conclusion is supported by the development of the vertical velocity contours when the depth of the LMAB is increased (Figure 5.6). The correspondence between panel (c) and Figure (5.1.b), where the average displacement field introduced by the 1986 event is given, is clear.

In Tables (5.5) to (5.7) the maxima of the horizontal and vertical velocities for all three earthquakes and the total are given for all positions of the LMAB. They clarify that there is indeed a downwards trend of the maxima with an increasing LMAB depth. The most pronounced decrease occurs when the LMAB position is altered from 70 to 90 km. The maxima of the 1977 event, which had the dominating influence to the total, suddenly drop to much smaller values and the 1986 event becomes the main contributor. These numbers confirm what was already visible in the figures. A similar fall occurs in the maxima of the 1990 event but the influence of this earthquake to the total postseismic surface velocities is of lesser importance. An explanation for this decline is that by changing the position of the LMAB to a depth of 90 km, the 1977 and the 1990 earthquakes would have taken place in the lithospheric mantle with a viscosity of 10^{22} Pa s, and as previously discussed the postseismic contribution of this layer to the present-day velocities is small due to its high relaxation time. Thus a reasonable inference is that the influence of earthquakes that occur in this layer decreases in comparison

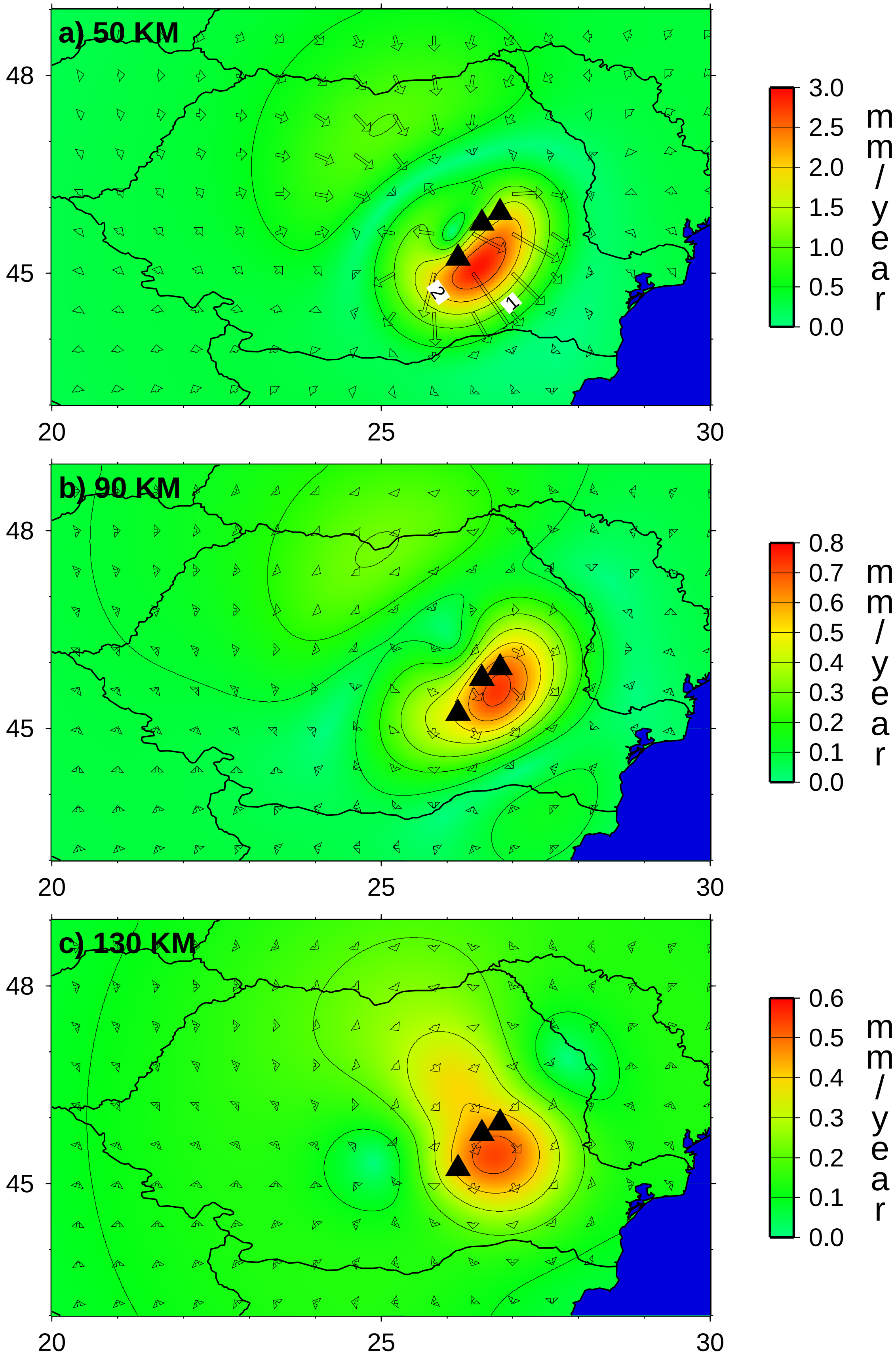

Figure 5.5 Average horizontal surface displacement change from 2002 to 2006 over Romania for an Earth model with varied lithospheric mantle - asthenosphere boundary depth. The 2-D locations of the earthquakes are indicated by a black triangle

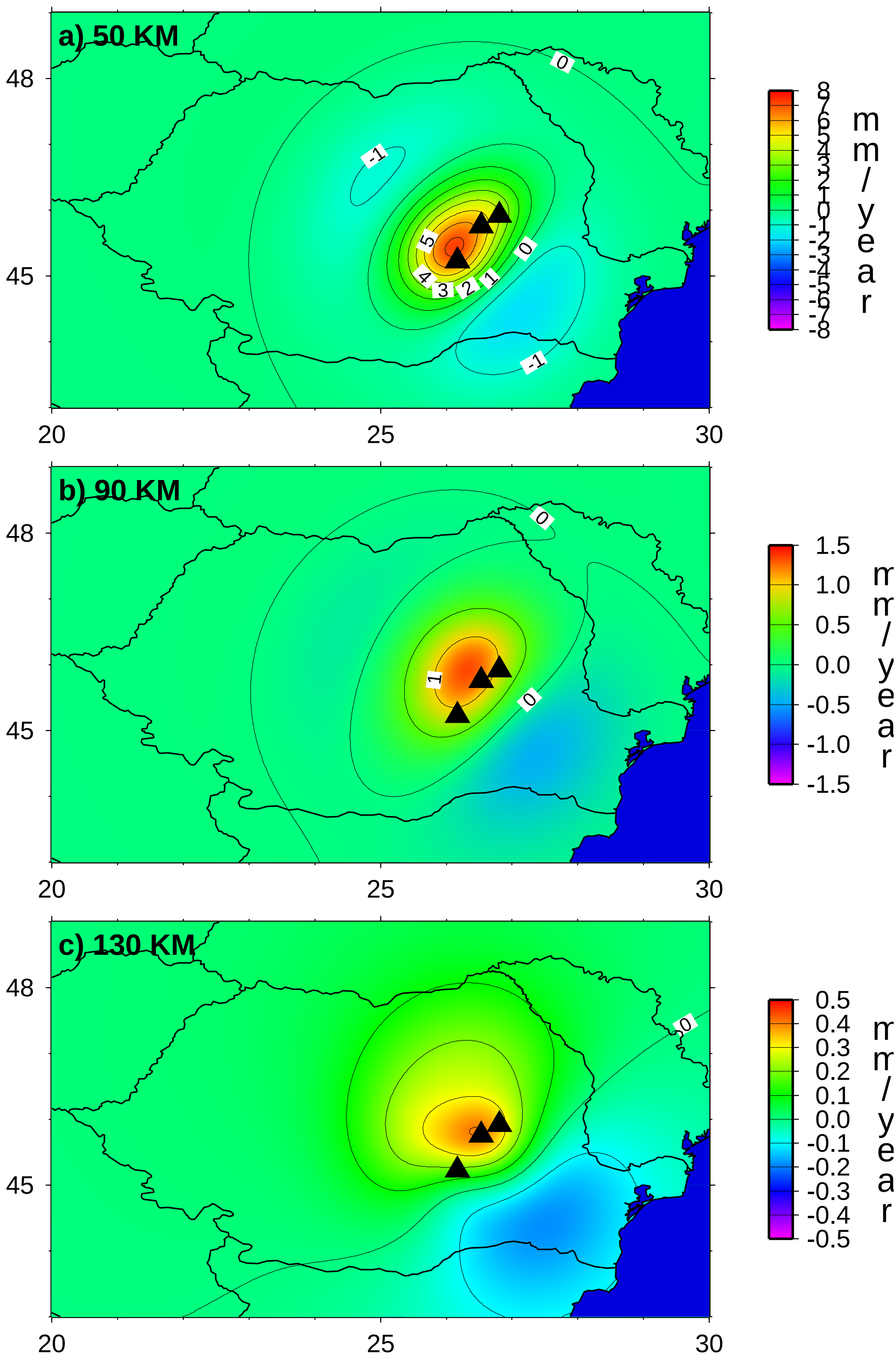

Figure 5.6 Average vertical surface displacement change from 2002 to 2006 over Romania for an Earth model with varied lithospheric mantle - asthenosphere boundary depth. The 2-D locations of the earthquakes are indicated by a black triangle

Table 5.5 Maximal horizontal velocity

LMAB depth (km)	4-Mar-77 (mm/year)	30-Aug-86 (mm/year)	30-May-90 (mm/year)	Total (mm/year)
50	2.14	0.98	0.60	2.91
70	1.09	0.86	0.37	1.76
90	0.19	0.77	0.05	0.74
110	0.13	0.67	0.04	0.68
130	0.08	0.57	0.02	0.54

Table 5.6 Minimal vertical velocity

LMAB depth (km)	4-Mar-77 (mm/year)	30-Aug-86 (mm/year)	30-May-90 (mm/year)	Total (mm/year)
50	-1.26	-1.06	-0.22	-1.91
70	-0.95	-0.82	-0.17	-0.77
90	-0.16	-0.61	-0.04	-0.45
110	-0.06	-0.39	-0.02	-0.24
130	-0.03	-0.25	-0.01	-0.19

to when they are located in a layer with a lower viscosity. The tables also show that the maxima of the 1986 earthquake decrease under the influence of an increasing lithospheric mantle thickness or, probably more important, a decreasing asthenosphere thickness, though the lessening is more gradual.

A last remark about the tables is that sometimes the horizontal maximum of the total is smaller than the corresponding value of a separate earthquake. This is explained by the fact that the numbers in the table are vector magnitudes and that after summation with a vector in a different direction the magnitude of the result does not necessarily have to be larger. The general conclusion for this Earth model is that the induced postseismic velocities decrease when the LMAB position is lowered.

Asthenosphere viscosity

In the last situation the results are calculated for models with an asthenosphere viscosity varying from 10^{17} to 10^{20} Pa s. The velocity field of three of these mod-

Table 5.7 Maximal vertical velocity

LMAB depth (km)	4-Mar-77 (mm/year)	30-Aug-86 (mm/year)	30-May-90 (mm/year)	Total (mm/year)
50	6.61	1.53	1.57	7.25
70	3.39	1.17	0.94	3.81
90	0.73	0.88	0.16	1.33
110	0.26	0.62	0.08	0.88
130	0.14	0.29	0.03	0.40

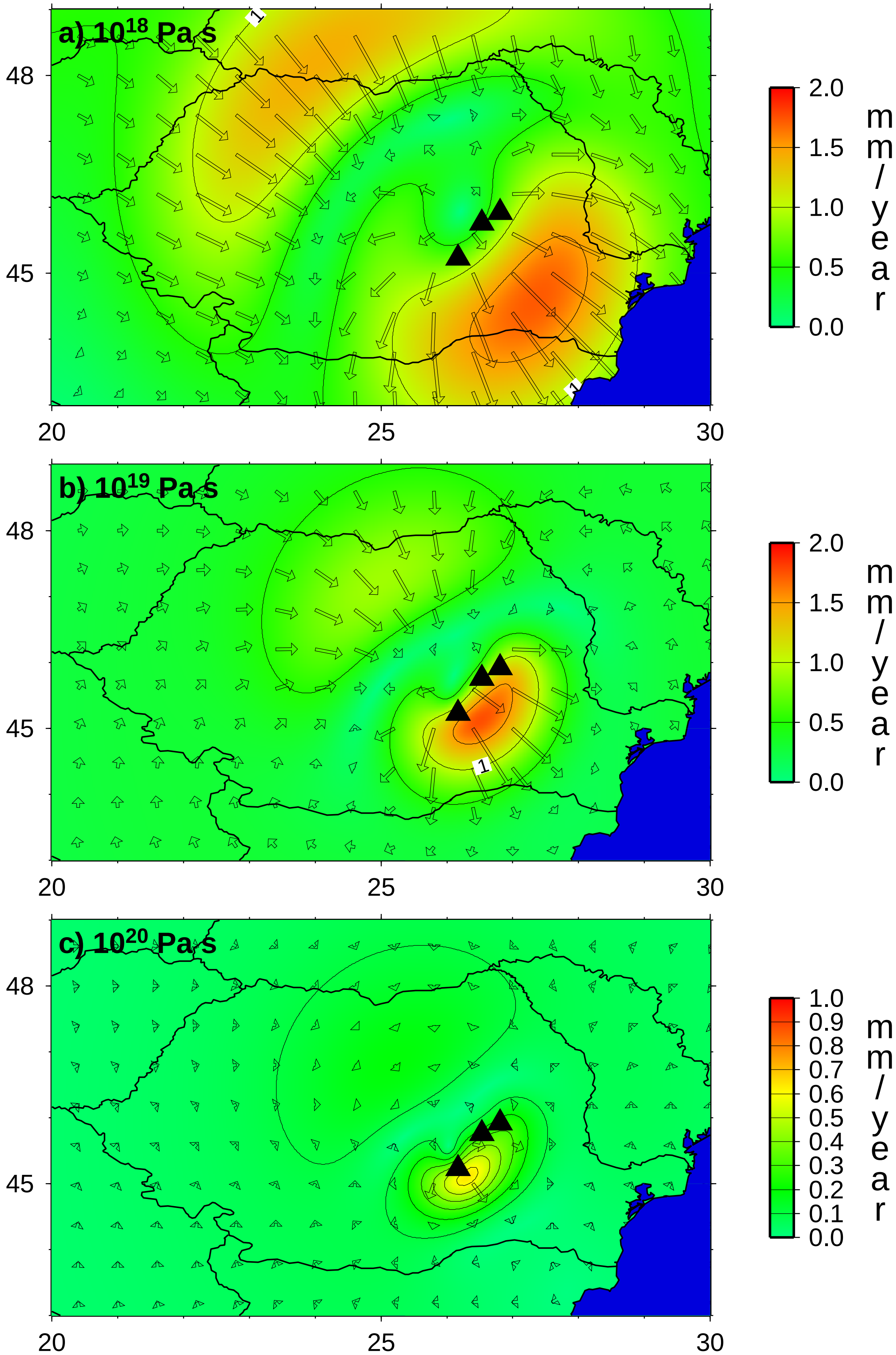

Figure 5.7 Average horizontal surface displacement change from 2002 to 2006 over Romania for an Earth model with varied asthenosphere viscosity. The 2-D locations of the earthquakes are indicated by a black triangle

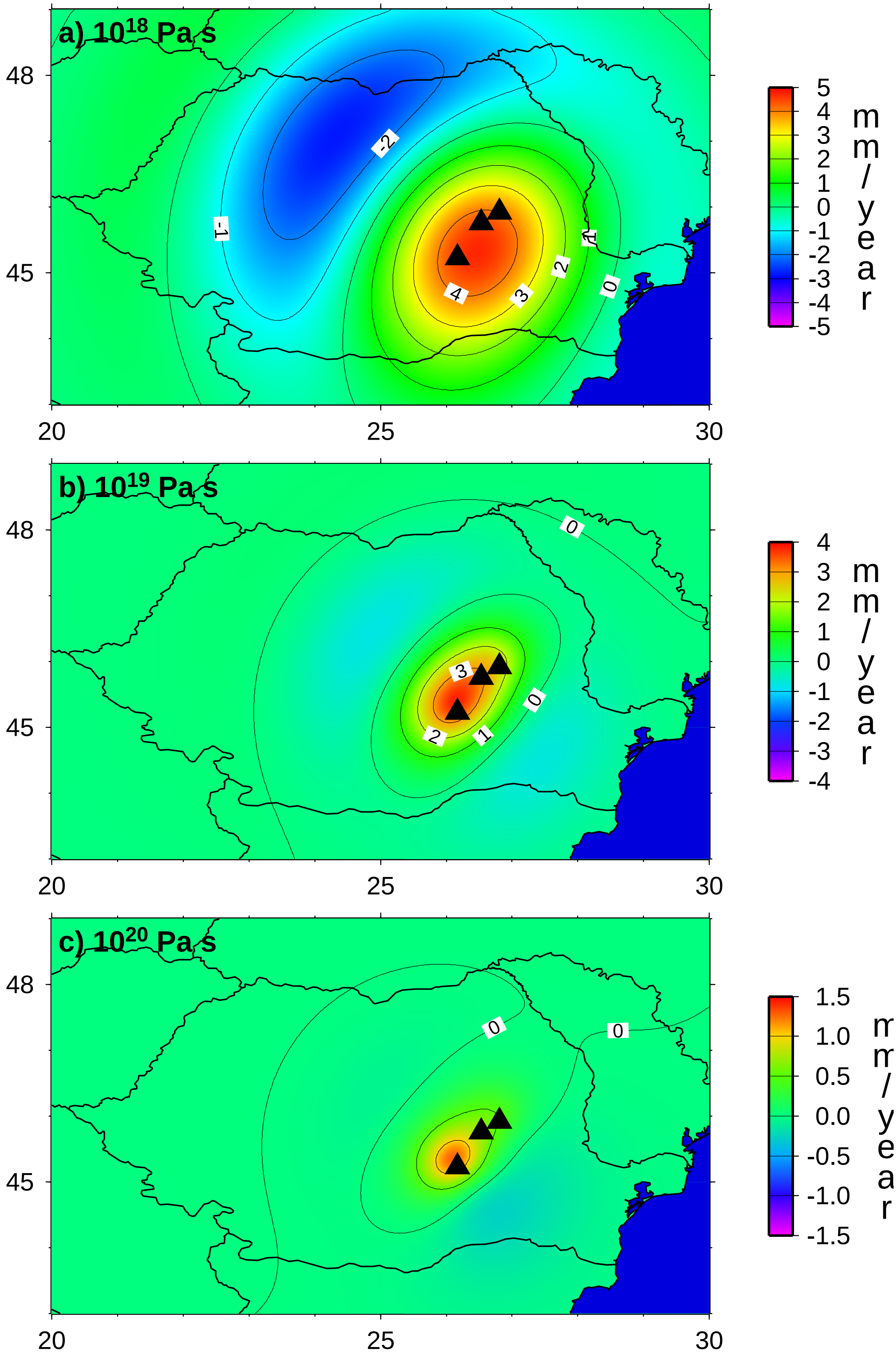

Figure 5.8 Average vertical surface displacement change from 2002 to 2006 over Romania for an Earth model with varied asthenosphere viscosity. The 2-D locations of the earthquakes are indicated by a black triangle

Table 5.8 Maximal horizontal velocity

Ast. viscosity (Pa s)	4-Mar-77 (mm/year)	30-Aug-86 (mm/year)	30-May-90 (mm/year)	Total (mm/year)
10^{17}	1.36	1.74	0.51	1.62
10^{18}	1.20	1.38	0.33	1.72
10^{19}	1.09	0.86	0.37	1.76
10^{20}	0.54	0.16	0.11	0.63

Table 5.9 Minimal vertical velocity

Ast. viscosity (Pa s)	4-Mar-77 (mm/year)	30-Aug-86 (mm/year)	30-May-90 (mm/year)	Total (mm/year)
10^{17}	-7.34	-5.71	-2.63	-5.18
10^{18}	-3.40	-2.60	-0.97	-2.82
10^{19}	-0.95	-0.82	-0.17	-0.77
10^{20}	-0.16	-0.11	-0.03	-0.26

els, the ones with an asthenosphere viscosity of 10^{18}, 10^{19} and 10^{20} Pa s, are illustrated in Figure (5.7) for the horizontal postseismic velocities, and in Figure (5.8) for the vertical velocities. All the maximal resulting velocities for the separate earthquakes and the total are given in Tables (5.8) to (5.10). These tables clarify that within the range of previously stated viscosities the maximal velocities as a result of the separate earthquakes increase with decreasing viscosity. However, Figure (5.7) and Table (5.8) show that this is not always true for the total velocities. The total maximal horizontal velocities for models with asthenosphere viscosities of 10^{17} to 10^{19} Pa s do not differ much, they even decrease with decreasing viscosity. The reason for this can be deduced from Figure (5.7). By decreasing the asthenosphere viscosity the shape of the contours widens and moves away from the epicenters of the earthquakes. This happens for every earthquake and when the resulting displacements are added, the maxima do not coincide anymore and the velocity vectors point in different directions resulting in smaller total magnitudes.

The same widening of the shape of the contours is visible in Figure (5.8) for the resulting vertical velocities. Take for example the 1 mm/year contour that does not even surround all the triangles denoting the locations of the epicenters in Figure (5.8.c). When the asthenosphere viscosity decreases to 10^{19} Pa s, panel (***b***) shows that the contour has expanded to surround all the epicenters. A further

Table 5.10 Maximal vertical velocity

Ast. viscosity (Pa s)	4-Mar-77 (mm/year)	30-Aug-86 (mm/year)	30-May-90 (mm/year)	Total (mm/year)
10^{17}	8.84	6.54	2.79	6.87
10^{18}	4.73	3.22	1.08	4.71
10^{19}	3.39	1.17	0.94	3.81
10^{20}	1.22	0.18	0.23	1.27

decrease of the viscosity to 10^{18} Pa s results in a zero velocity contour that almost surrounds the whole southeastern area of Romania.

Tables (5.9) and (5.10) show that the combined minimal and maximal velocities follow the trend of the separate earthquakes. They both increase in absolute numbers with decreasing asthenosphere viscosity. The increase experienced by the total is however low when compared to the sum of the increases of the velocities induced by the separate earthquakes. This is again caused by difference in location of the maxima. In general it is concluded that decreasing the asthenosphere viscosity can be the source of increasing present-day surface velocities and it causes widening of the contours.

5.2 Results for seven-layer model

5.2.1 Original model

Similar as for the five-layer model a figure of the horizontal (Figure 5.9) and one for the vertical (Figure 5.10) postseismic surface velocity is presented for the seven-layer model as it is given in Table (4.2). Both are composed out of the results of the 1977, the 1986 and the 1990 events and their total, respectively. The maximal velocities reached as a consequence of the separate earthquakes and their total are given in Table (5.11). These figures and the table show that again the 1977 event has the largest influence to the total followed by the 1986 and then the 1990 earthquake. The way the results corresponding to the separate earthquakes and their total mutually differ, is equal to the behavior of the five-layer model (Section 5.1) so no new conclusions can be made.

It is more interesting to compare these results with the five-layer Earth model (Figures 5.1 and 5.2) because the only difference is the low-viscosity zone (LVZ) underneath the lithosphere and the separation in the mantle into an upper and lower mantle with different viscosities. In Section (5.2.2) it shall be shown that the influence of the latter is minimal. A difference is that the maximal velocities increase but that the rise caused by the 1977 event is far greater than for the other events meaning that both its positive maxima are more than twice as large as the positive maxima caused by the 1986 earthquake. The largest differences are visible in Figures (5.9) and (5.10) of the postseismic velocities of the 1977 and the 1990 events, probably because they are located closer to the LVZ. There the higher velocities in the far field northwest of the earthquakes have disappeared and an area of high velocities, even higher than in the southeastern direction, has appeared to the northwest, close to the epicenters. The velocity vectors on opposite sides of the epicenters point in opposite directions.

When the total horizontal velocities of both Earth models are compared it is visible that the LVZ causes larger velocities close to epicenters of the earthquakes, but almost no movement in the far-field. Figures (5.9) and (5.10) clarify that except for the bulge towards the northwest in Figure (5.9.d), the 1 mm/year contours are of the same shape and cover approximately the same area, although the velocities reached within are larger for the seven-layer model. The LVZ also causes the velocities south and east of the epicenters to curve towards the southeast.

Quite remarkable is that except for higher velocities inserting an LVZ has almost no effect on the vertical velocity pattern (compare Figures 5.2 and 5.10). A comparison between Tables (5.11) and (5.1) shows that the difference is so that

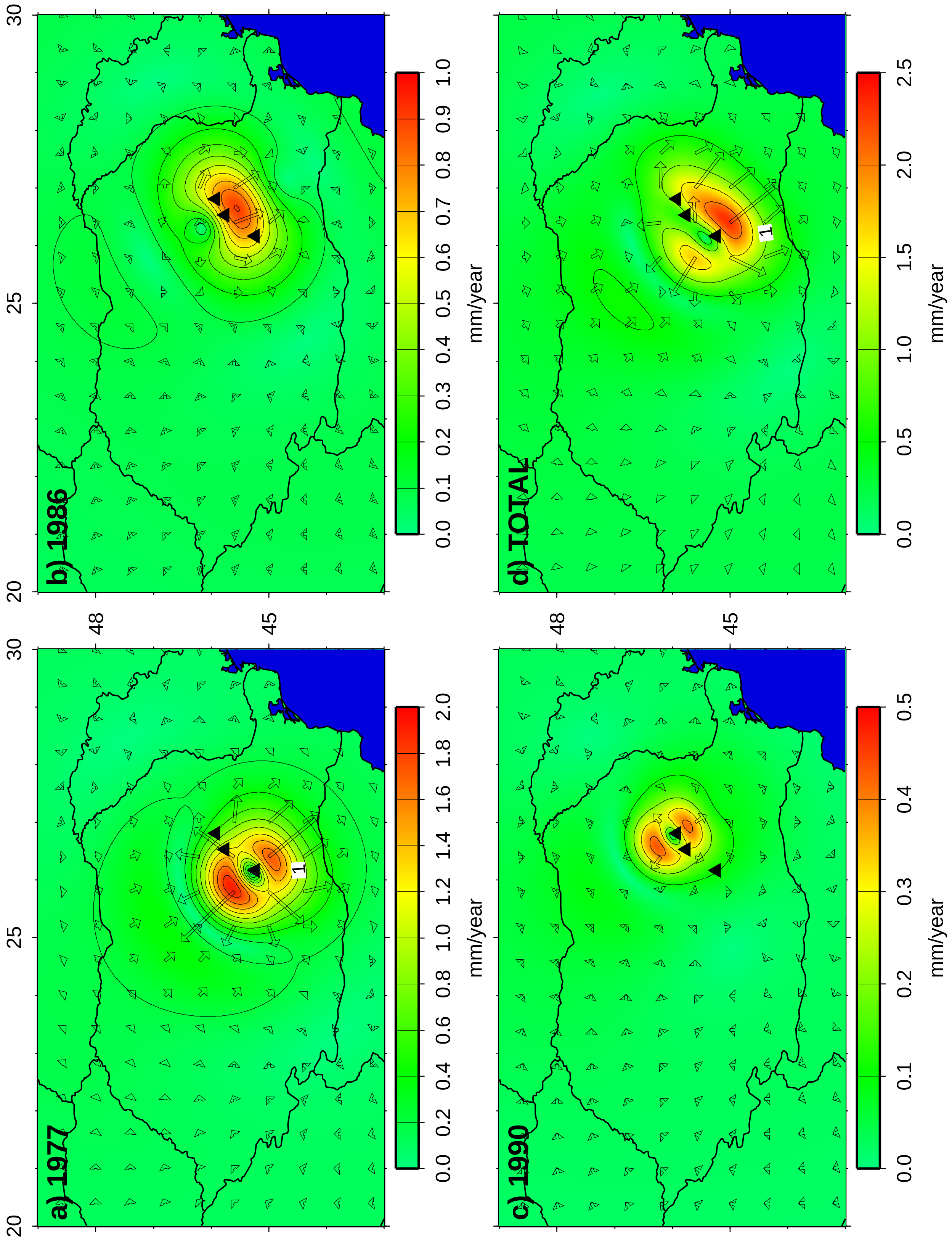

Figure 5.9 Average horizontal surface displacement change from 2002 to 2006 over Romania as result of three separate earthquakes (a-c) and their total (d). The 2-D locations of the earthquakes are indicated by a black triangle

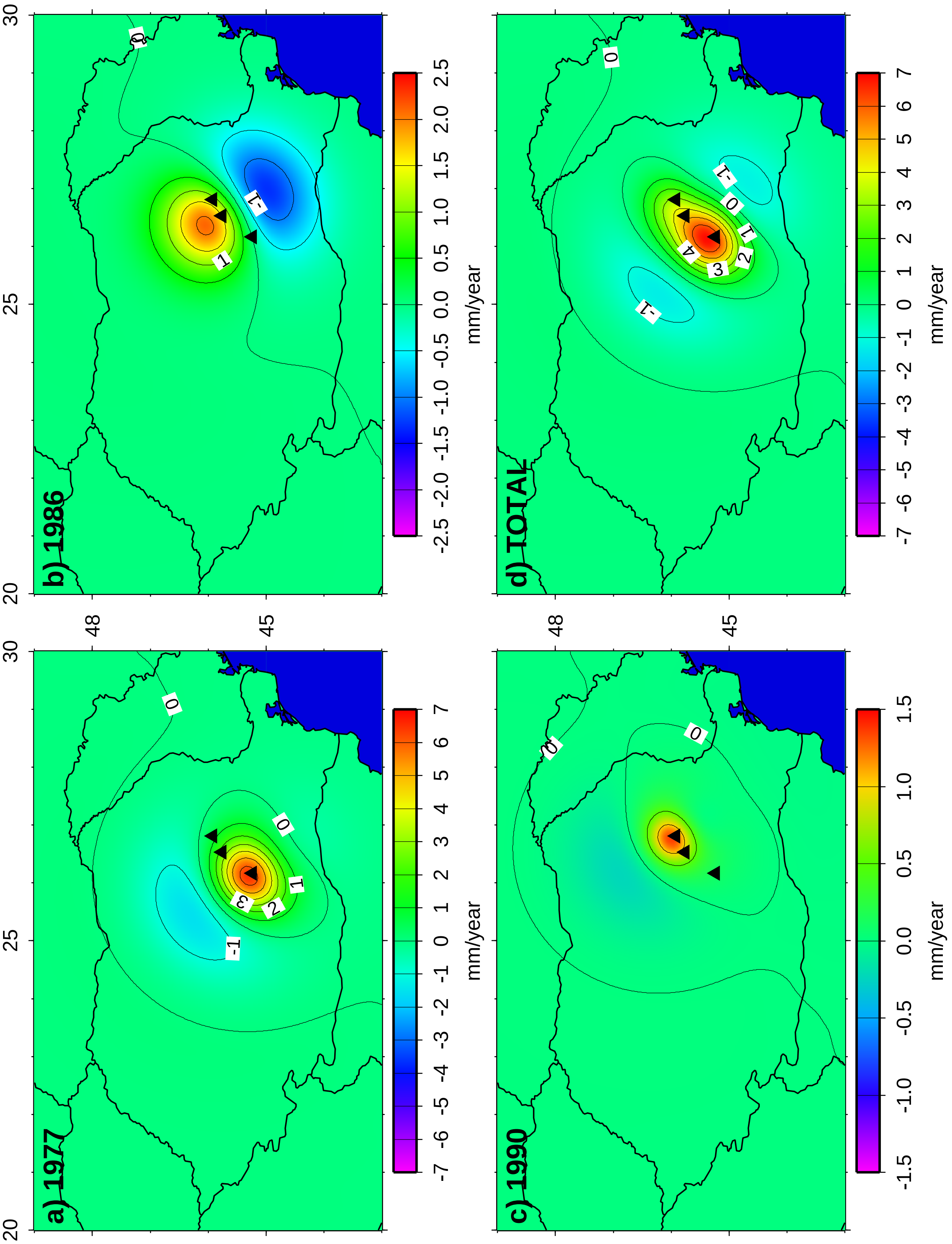

Figure 5.10 Average vertical surface displacement change from 2002 to 2006 over Romania as result of three separate earthquakes (a-c) and their total (d). The 2-D locations of the earthquakes are indicated by a black triangle

both the positive and the negative maximum, induced by the seven-layer model, are almost twice as large as for the five-layer model. Relative to the horizontal velocity increase all three earthquakes cause an equally strong increase. Thus, it may be concluded that for the induced postseismic vertical velocity the influence of the LVZ does not depend on the distance between the LVZ and the depth at which the earthquake occurred.

Table 5.11 Maximal velocities of the original seven-layer model

	4-Mar-77 (mm/year)	30-Aug-86 (mm/year)	30-May-90 (mm/year)	Total (mm/year)
Max. horizontal velocity	1.91	0.90	0.43	2.32
Min. vertical velocity	-1.54	-1.32	-0.23	-1.28
Max. vertical velocity	6.43	2.10	1.35	6.89

5.2.2 Varying model properties

In this section the resulting changes to the calculated displacements after varying one model property will be discussed, similarly as for the five-layer model in Section (5.1.2).

Low-viscosity zone viscosity

Figure (5.11) illustrates the calculated present-day horizontal velocities for the models with an LVZ viscosity of 10^{17}, 10^{18} and 10^{19} Pa s, respectively. They clearly show that by increasing the LVZ viscosity, the movement in the north-western near-field diminishes, while in the far-field the area of slightly larger velocities expands and the local velocities increase. The resulting postseismic vertical velocities are given in Figure (5.11) where only small differences in location and shape of the contours are visible. The most significant is the disappearing of the -1 mm/year contour when the viscosity reaches 10^{19} Pa s, while the positive maximum remains equally large as in the preceding case.

The difference between the maxima reached shall be discussed by making use of Tables (5.12) to (5.14) which give the maximal horizontal, the minimal vertical and the maximal vertical velocity respectively reached for models with the above mentioned LVZ viscosities, 10^{20} Pa s and elastic. In the latter case the model is almost equal to the five-layer Earth model. When the last rows of Tables (5.12) to (5.14) are compared to the numbers in Table (5.1), it is clear that the influence of separating the mantle is indeed negligible.

The tables show that in all cases the 1977 earthquake induces the highest velocities and thus contribute the most to the total result. Table (5.13) indicates that the postseismic minimal vertical velocity decreases in absolute numbers when the LVZ viscosity is increased from 10^{17} Pa s. The most remarkable drop occurs when the viscosity is increased from 10^{18} to 10^{19} Pa s. As a result, the value of the minimal velocity caused by all three earthquakes separate and for the total, is reduced with more than a third. The difference between all the other cases is not nearly as large.

For the maximal vertical velocity (see Table 5.14), a similar decrease occurs for models with LVZ viscosities of 10^{18} Pa s and up. However, for a viscosity of 10^{17} Pa s, the maxima of the 1977 and the 1990 events drop significantly to a

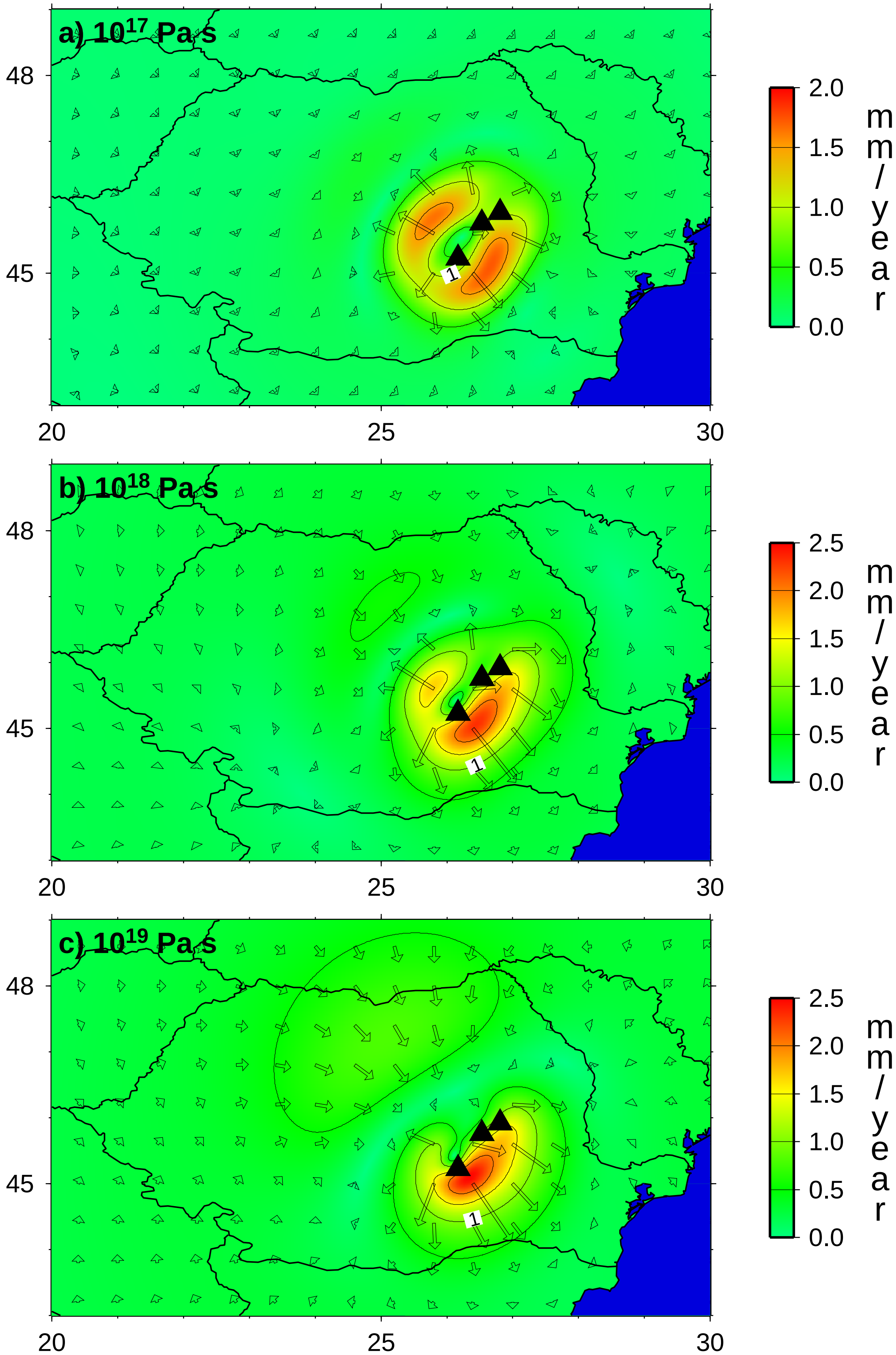

Figure 5.11 Average horizontal surface displacement change from 2002 to 2006 over Romania for an Earth model with varied low-viscosity zone viscosity. The 2-D locations of the earthquakes are indicated by a black triangle

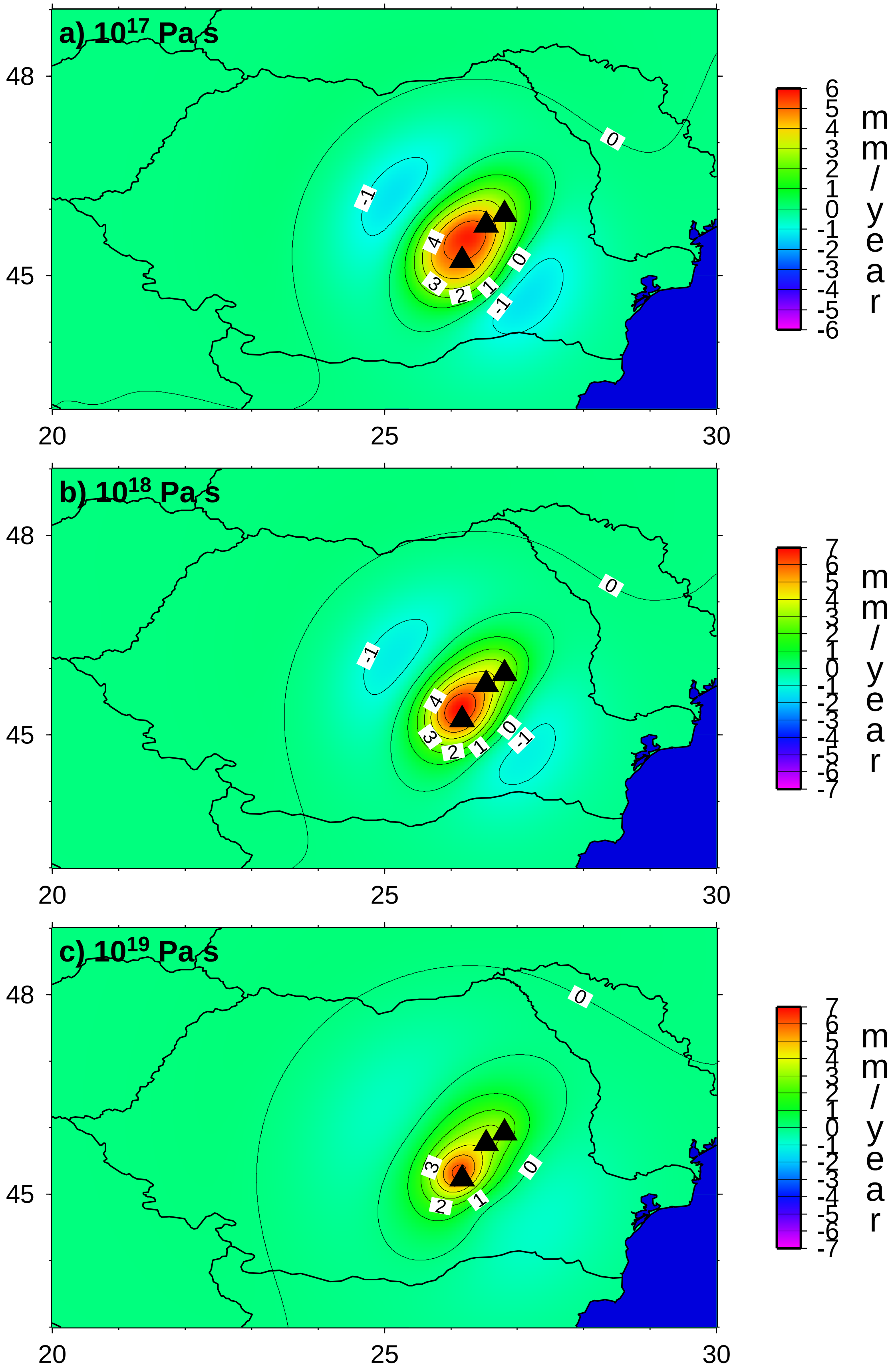

Figure 5.12 Average vertical surface displacement change from 2002 to 2006 over Romania for an Earth model with varied low-viscosity zone viscosity. The 2-D locations of the earthquakes are indicated by a black triangle

Table 5.12 Maximal horizontal velocity

LVZ viscosity (Pa s)	4-Mar-77 (mm/year)	30-Aug-86 (mm/year)	30-May-90 (mm/year)	Total (mm/year)
10^{17}	1.58	0.72	0.33	1.73
10^{18}	1.91	0.90	0.43	2.32
10^{19}	1.81	0.94	0.48	2.48
10^{20}	1.19	0.85	0.38	1.84
10^{50}	1.09	0.83	0.37	1.74

Table 5.13 Minimal vertical velocity

LVZ viscosity (Pa s)	4-Mar-77 (mm/year)	30-Aug-86 (mm/year)	30-May-90 (mm/year)	Total (mm/year)
10^{17}	-1.55	-1.33	-0.24	-1.31
10^{18}	-1.54	-1.32	-0.23	-1.28
10^{19}	-0.92	-0.92	-0.15	-0.81
10^{20}	-0.85	-0.81	-0.15	-0.81
10^{50}	-0.85	-0.79	-0.15	-0.78

value below the velocity magnitudes corresponding to an LVZ viscosity of 10^{19} Pa s. As the velocity corresponding to the 1986 earthquake also slightly drops, the same is valid for the total. It seems that positioning of the earthquakes closer to the LVZ causes the resulting maximal vertical velocity to be more sensitive to changes applied.

Table (5.12) shows that there is probably no simple connection between the viscosity of the low-viscosity zone and the maximal horizontal velocity reached. For the 1986, the 1990 event and the total, the largest maximum is reached for a viscosity of 10^{19} Pa s while a model with an LVZ viscosity of 10^{17} Pa s results in the smallest value. The maximum corresponding to the 1977 event is obtained for a viscosity of 10^{18} Pa s, while an elastic LVZ results in the smallest number.

In this case there does not seem to be a connection between the results of the 1977 and the 1990 earthquake despite their similar location. And although the 1977 event results in the largest maxima, its influence on the total horizontal velocity does not seem to be as significant as the influence of the other two. This can be explained by the fact that for this event the maximum is obtained in the

Table 5.14 Maximal vertical velocity

LVZ viscosity (Pa s)	4-Mar-77 (mm/year)	30-Aug-86 (mm/year)	30-May-90 (mm/year)	Total (mm/year)
10^{17}	4.88	2.01	0.92	5.75
10^{18}	6.43	2.10	1.35	6.89
10^{19}	5.95	1.47	1.25	6.29
10^{20}	3.65	1.14	0.97	4.05
10^{50}	3.33	1.12	0.94	3.74

Table 5.15 Maximal horizontal velocity

LVZ thickness (km)	4-Mar-77 (mm/year)	30-Aug-86 (mm/year)	30-May-90 (mm/year)	Total (mm/year)
5	1.91	0.90	0.43	2.32
10	1.72	0.88	0.34	2.07
20	1.17	0.73	0.25	1.62

Table 5.16 Minimal vertical velocity

LVZ thickness (km)	4-Mar-77 (mm/year)	30-Aug-86 (mm/year)	30-May-90 (mm/year)	Total (mm/year)
5	-1.54	-1.32	-0.23	-1.28
10	-1.44	-1.36	-0.21	-1.22
20	-0.95	-1.25	-0.17	-1.66

area northwest of the earthquake epicenter (see Section 5.2.1), where the velocities introduced by the 1986 event are almost zero. So the maximal values of their sum are reached in an area where the maximum of the 1986 event is located. The other two earthquakes only induced average values which makes the maximum of the 1986 event dominant.

Low-viscosity zone thickness

As a second variation three models were simulated with varying LVZ thickness: 5, 10 and 20 km. In these models the thickness of the lithosphere was kept constant so it was the thickness of the lithosphere mantle that was also changed to 20, 15, and 5 km, respectively. The figures of the horizontal and vertical velocities (Figures 5.13 and 5.14) illustrate that the largest differences between the velocity fields are noticeable when the LVZ thickness is increased from 10 to 20 km. For the model with an LVZ thickness of 20 km, the horizontal 0.5 mm/year contour is equally large or even larger than for the other cases while the maximal velocity reached within this contour is smaller. The same is valid for the zero velocity contour of the vertical velocity. Figure (5.14.c) also shows that for a thickness of 20 km the minimum is reached to the southeast of the epicenters whereas for the other two cases there are two areas where the minus one contour is reached, situated on opposite sides of the epicenters. The area surrounded by the -1 mm/year contour in graph $(\boldsymbol{c})$ is however larger and a higher minimum is reached. The difference between the 5 and the 10 km LVZ thickness cases are insignificantly small changes to the velocity and shape of the contours.

The last columns of Tables (5.15) and (5.17) where the maximal horizontal and the vertical resulting velocities of all three earthquakes are given, confirm the trend of declining velocities caused by an increasing LVZ thickness. The last column of Table (5.16) confirms that in absolute numbers there is only a small difference between the 5 and 10 km case and the model with the 20 km thick LVZ results in clearly the largest minimum, that is -1.66 mm/year.

Similar to the preceding tables, not only are the maxima of the total deformation given but also the velocities reached by the three earthquakes separately. Again the largest maxima are reached as a result of the 1977 earthquake followed

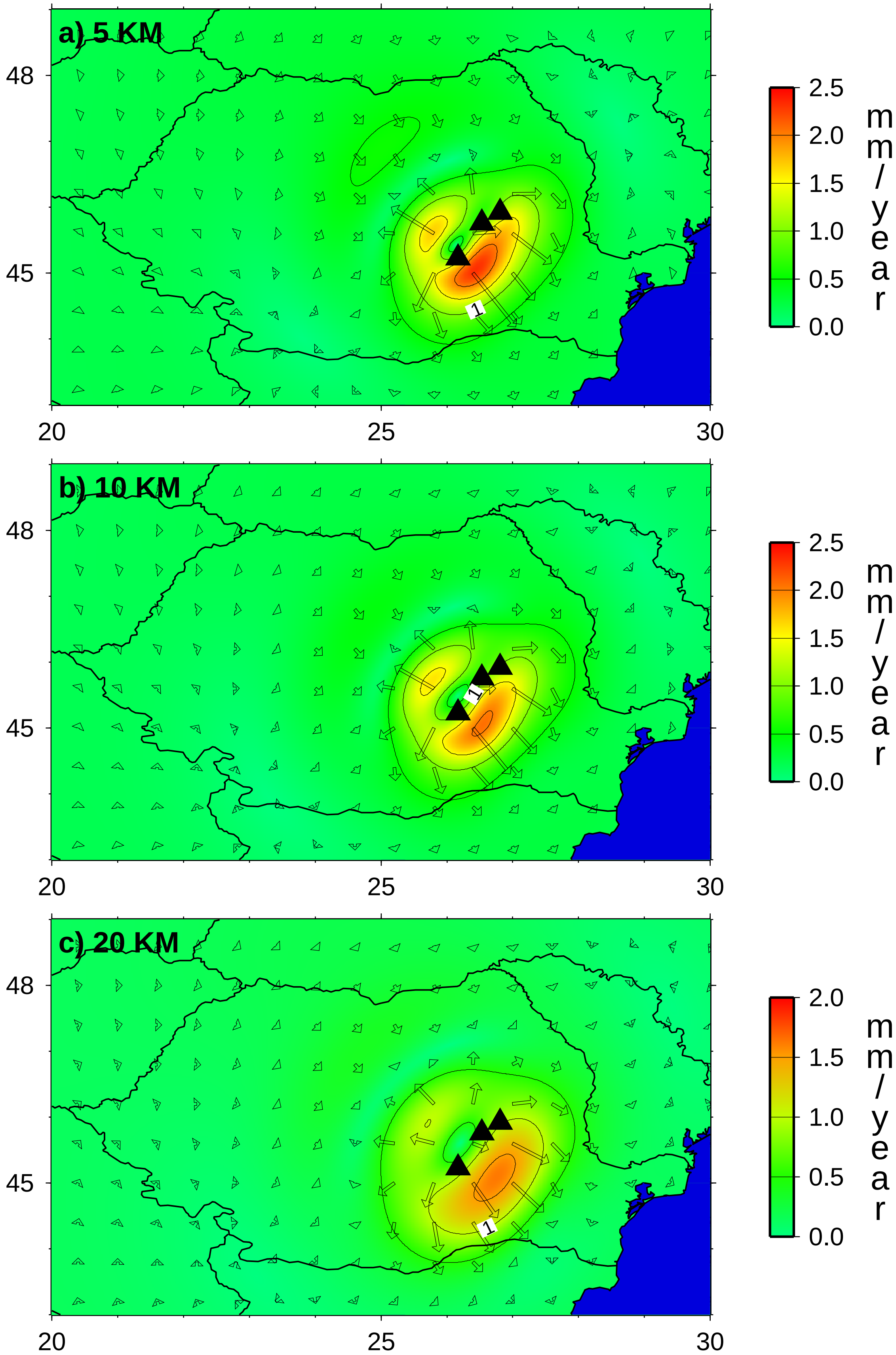

Figure 5.13 Average horizontal surface displacement change from 2002 to 2006 over Romania for an Earth model with varied low-viscosity zone thickness. The 2-D locations of the earthquakes are indicated by a black triangle

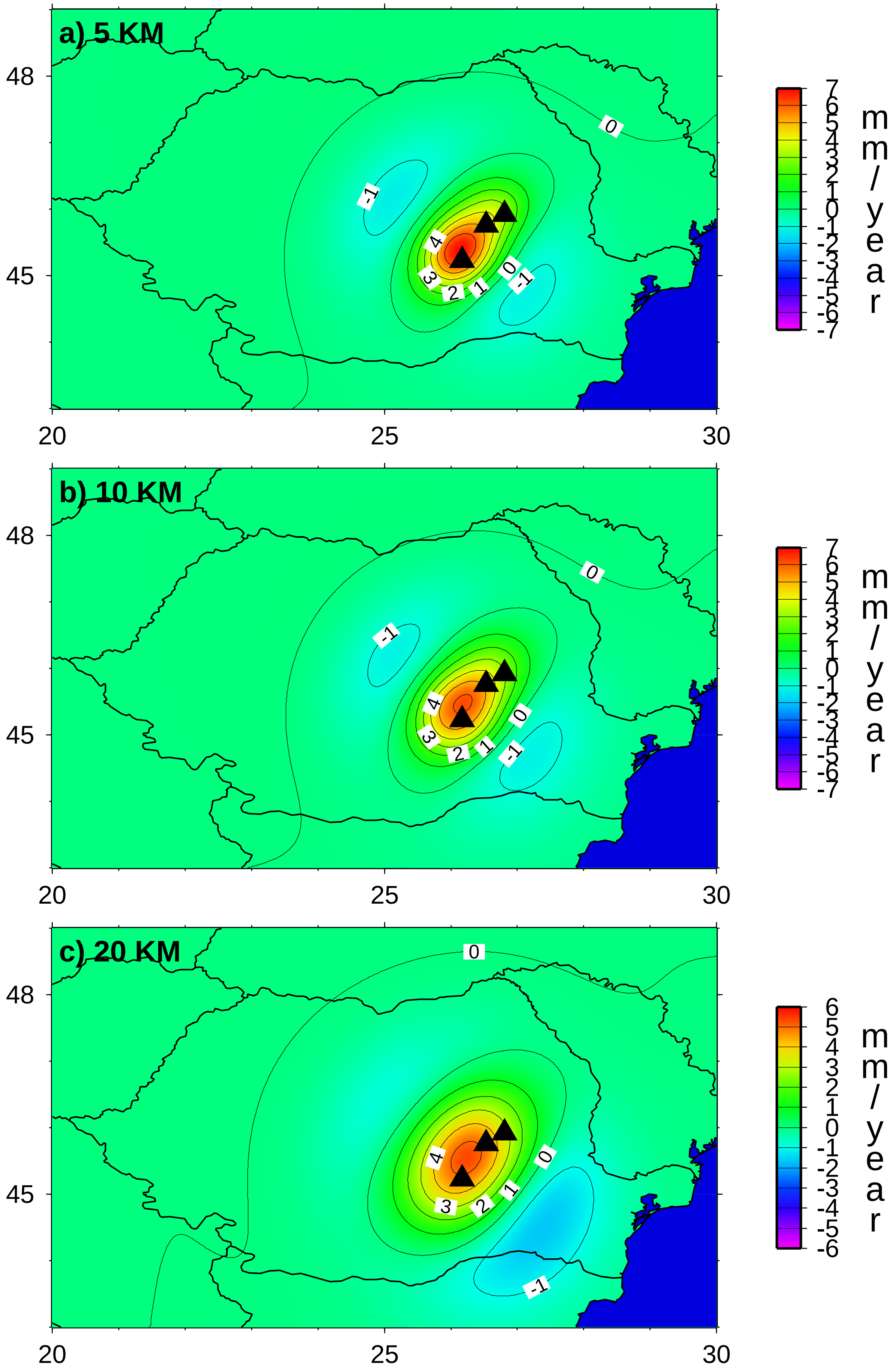

Figure 5.14 Average vertical surface displacement change from 2002 to 2006 over Romania for an Earth model with varied low-viscosity zone thickness. The 2-D locations of the earthquakes are indicated by a black triangle

by the 1986 and then the 1990 events, except for the minimal vertical velocity of the model with an LVZ thickness of 20 km. In that situation, the -1.25 mm/year minimum caused by the 1986 earthquake is smaller than the -0.95 mm/year minimum induced by the 1977 event. Tables (5.15) to (5.17) also clarify the difference between the depth at which the 1977 and the 1990 earthquakes occurred and where the 1986 event took place. In the case of the 1977 and the 1990 earthquakes the postseismic maximal velocities decrease with increasing LVZ thickness which, corresponds to the results of the total. In the case of the 1986 earthquake the same is true for the maximal horizontal velocity. However, the maximal and minimal vertical velocity are reached when the LVZ is 10 km. A general conclusion is that increasing the low-viscosity zone thickness results in a decline of the present-day maximal velocities and rise in the absolute minimal vertical velocity.

Lithospheric mantle viscosity

A variation was then applied to the lithospheric mantle (LM) viscosity. Figures (5.15) and (5.16) respectively give the horizontal and the vertical average deformation change based on models with a lithospheric mantle viscosity of 10^{18}, 10^{20} and 10^{22} Pa s, respectively. For the first case, it means that the model actually has a 25 km thick layer with a viscosity of 10^{18} Pa s, in between an elastic lithosphere and an asthenosphere with a viscosity of 10^{19} Pa s. This probably makes the model quite unrealistic because the strength profile (see Figure 4.1) clearly indicates two strong layers but in Section (5.1.2) it was already demonstrated that an elastic LM had almost no effect compared to the model with an LM viscosity of 10^{22} Pa s. Comparison of Figures (5.15) and (5.16) with Figures (5.3) and (5.4), respectively, shows that there is no reason to believe this result would change by inserting an LVZ. All the figures of the horizontal velocities illustrate that the decrease of the LM viscosity from 10^{22} to 10^{20} Pa s causes almost no change to the 1 mm/year contour, however, the velocities inside are higher. For the vertical velocities the same can be said for the zero velocity contour. The same comparison leads to the conclusion that when model parameters are changed, inserting an LVZ has no other effects than already discussed in Section (5.2.1) were both the original Earth models where compared. For the horizontal velocities there is almost no change to the direction of the vectors to the south-east of the epicenters, the magnitude is however larger for the seven-layer model. Towards the northwest the velocities in the far-field decrease and a bulge of high velocities appears in the near-field. For the vertical velocities no change to the shape of the deformation is visible and the LVZ causes almost a doubling of the maximal and minimal velocity induced by the separate earthquakes and also for the total.

These numbers can be confirmed in Tables (5.18) to (5.20) where the maximal horizontal and the minimal and maximal vertical velocities respectively for all the

Table 5.17 Maximal vertical velocity

LVZ thickness (km)	4-Mar-77 (mm/year)	30-Aug-86 (mm/year)	30-May-90 (mm/year)	Total (mm/year)
5	6.43	2.10	1.35	6.89
10	5.57	2.14	1.00	6.20
20	4.55	1.82	0.71	5.34

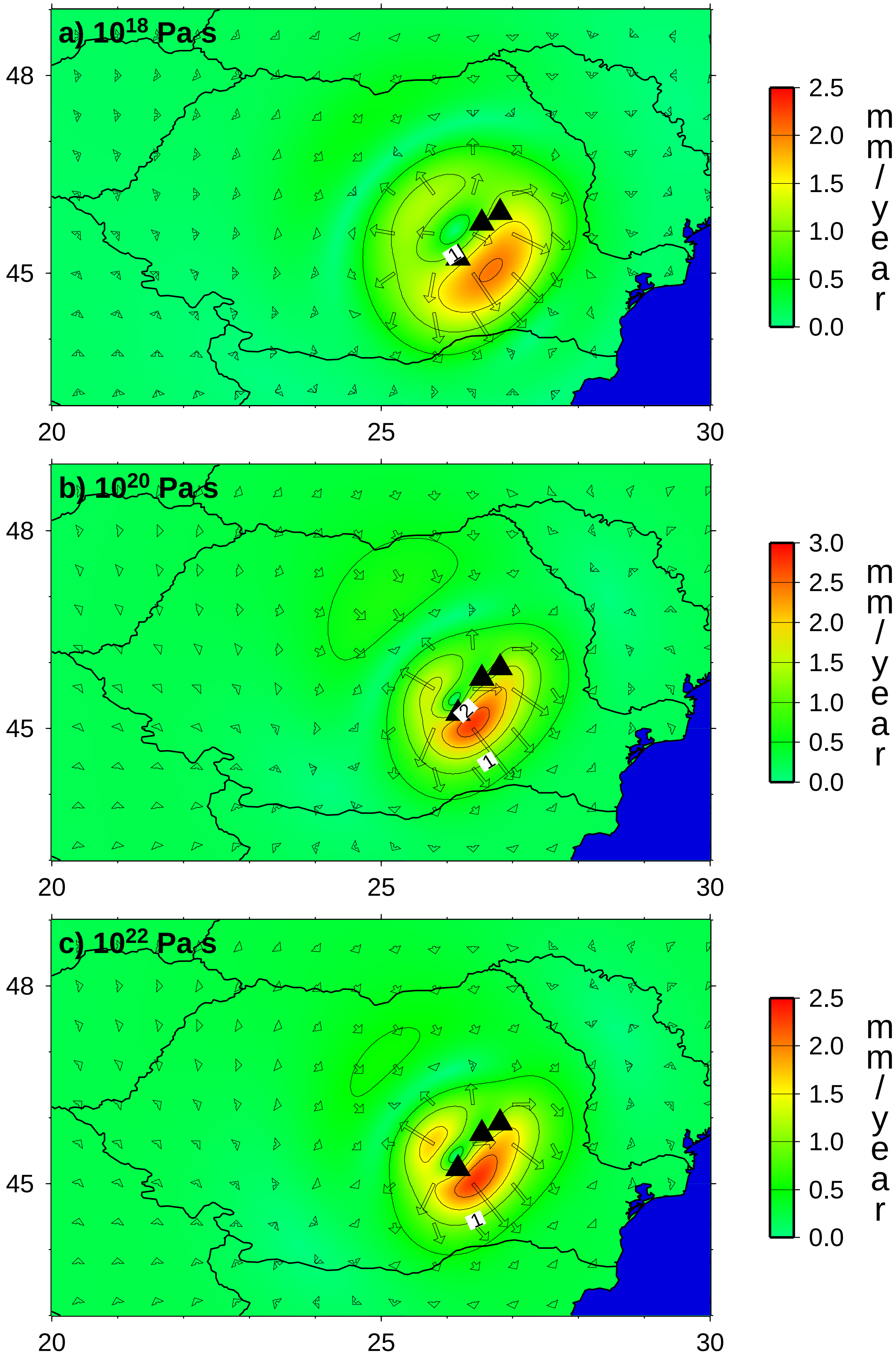

Figure 5.15 Average horizontal surface displacement change from 2002 to 2006 over Romania for an Earth model with varied lithospheric mantle viscosity. The 2-D locations of the earthquakes are indicated by a black triangle

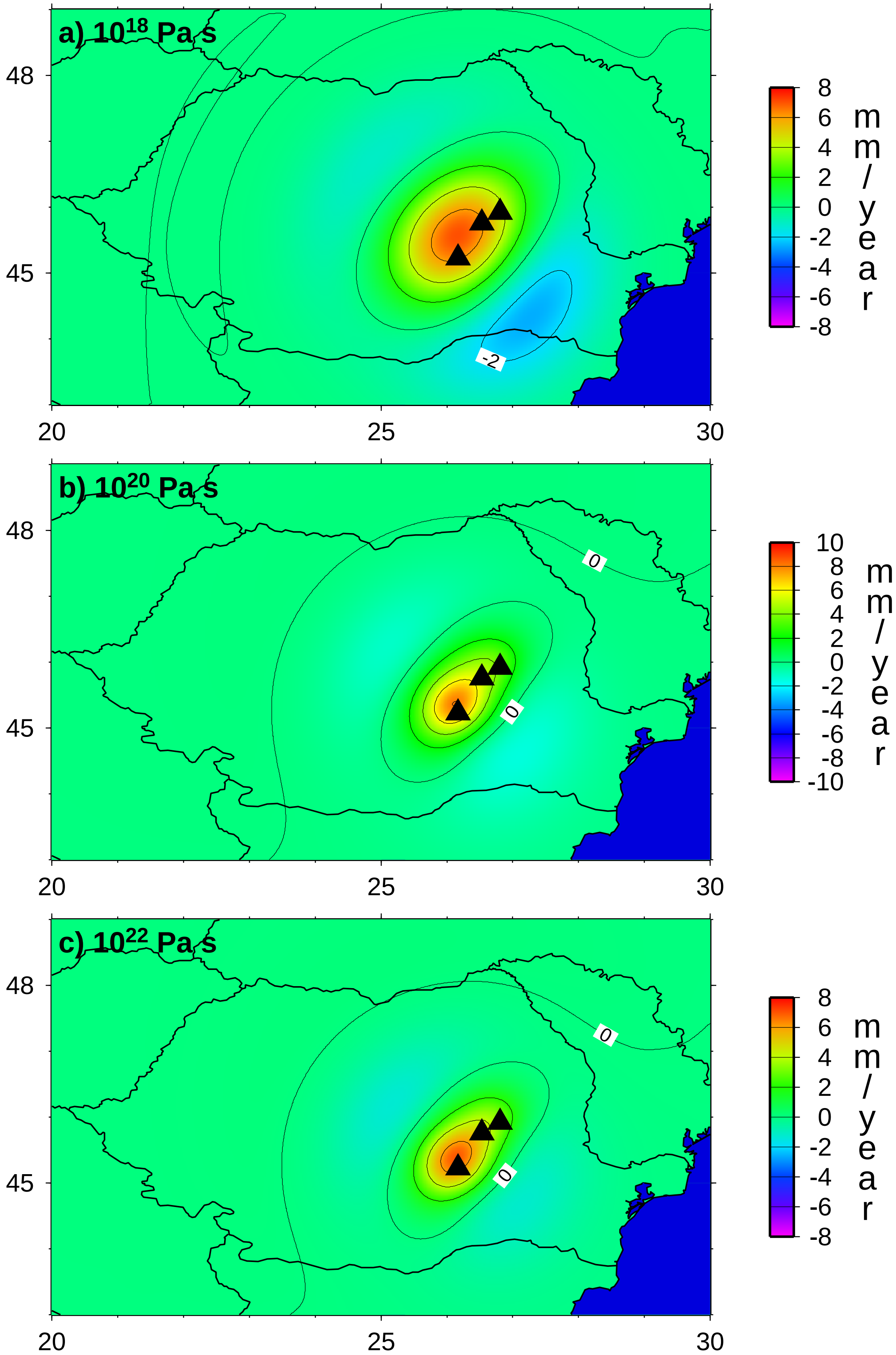

Figure 5.16 Average vertical surface displacement change from 2002 to 2006 over Romania for an Earth model with varied lithospheric mantle viscosity. The 2-D locations of the earthquakes are indicated by a black triangle

Table 5.18 Maximal horizontal velocity

LM viscosity (Pa s)	4-Mar-77 (mm/year)	30-Aug-86 (mm/year)	30-May-90 (mm/year)	Total (mm/year)
10^{18}	1,51	0,58	0,34	2,04
10^{20}	2,10	0,94	0,50	2,76
10^{22}	1,91	0,90	0,43	2,32

Table 5.19 Minimal vertical velocity

LM viscosity (Pa s)	4-Mar-77 (mm/year)	30-Aug-86 (mm/year)	30-May-90 (mm/year)	Total (mm/year)
10^{18}	-1,73	-1,12	-0,31	-2,62
10^{20}	-1,36	-1,31	-0,21	-1,46
10^{22}	-1,54	-1,32	-0,23	-1,28

Earth models are given. They clarify that the rank of the earthquakes concerning the maximal velocities stays unaltered. These tables also demonstrate that decreasing the LM viscosity to 10^{18} Pa s causes a decrease of the positive maximal velocities induced by all the earthquakes. This is remarkable because in the previous sections it has been demonstrated that decreasing the LVZ viscosity or the asthenosphere viscosity generally causes an increase of all the maximal velocities, both positive and negative, of the separate earthquakes. The only exception until now is the reduction of the LVZ viscosity from 10^{18} to 10^{17} Pa s.

Asthenosphere viscosity

The last variation applied was to the asthenosphere viscosity. The resulting average horizontal and vertical deformations have been calculated for models with an asthenosphere viscosity of 10^{18}, 10^{19} and 10^{22} Pa s. The horizontal and vertical velocities are respectively presented in Figures (5.17) and (5.18). Comparing these to the results of the asthenosphere variation applied to the five-layer model (Figures 5.7 and 5.8), shows that the influence of the changes are similar for both models. The only differences between the models were previously discussed in Section (5.2.1) and are assumed to be restricted to the change of including an LVZ in a model.

The exact numbers of the maxima can be found in Tables (5.21) to (5.23) but do not present any significant conclusions. Again the maxima of the 1977 event are the largest, followed by the 1986 and the 1990 earthquakes. This order can change when the viscosity is equal to 10^{22} Pa s but then the velocities are almost

Table 5.20 Maximal vertical velocity

LM viscosity (Pa s)	4-Mar-77 (mm/year)	30-Aug-86 (mm/year)	30-May-90 (mm/year)	Total (mm/year)
10^{18}	5,97	1,51	1,20	7,02
10^{20}	7,55	2,08	1,54	8,02
10^{22}	6,43	2,10	1,35	6,89

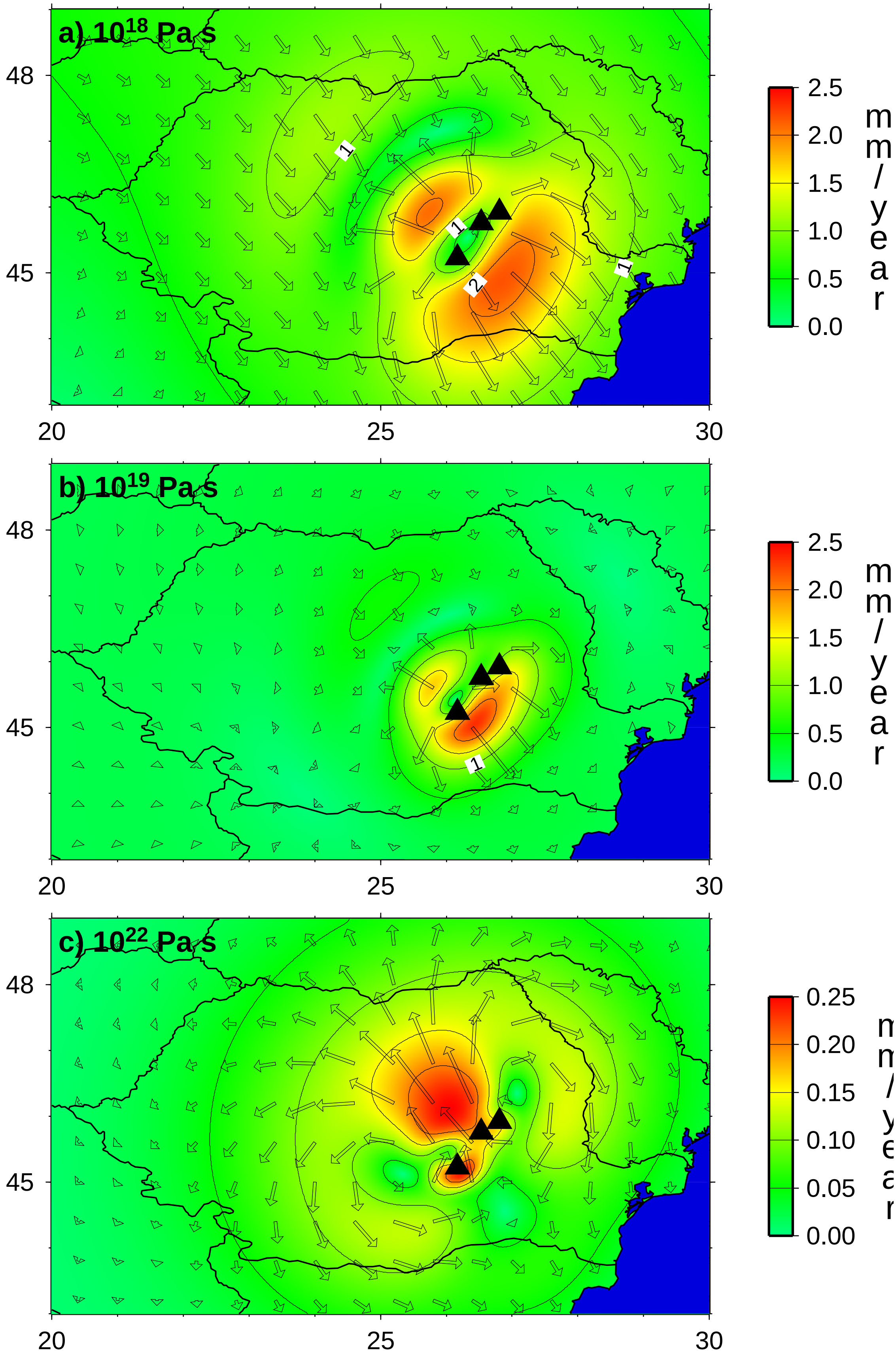

Figure 5.17 Average horizontal surface displacement change from 2002 to 2006 over Romania for an Earth model with varied asthenosphere viscosity. The 2-D locations of the earthquakes are indicated by a black triangle

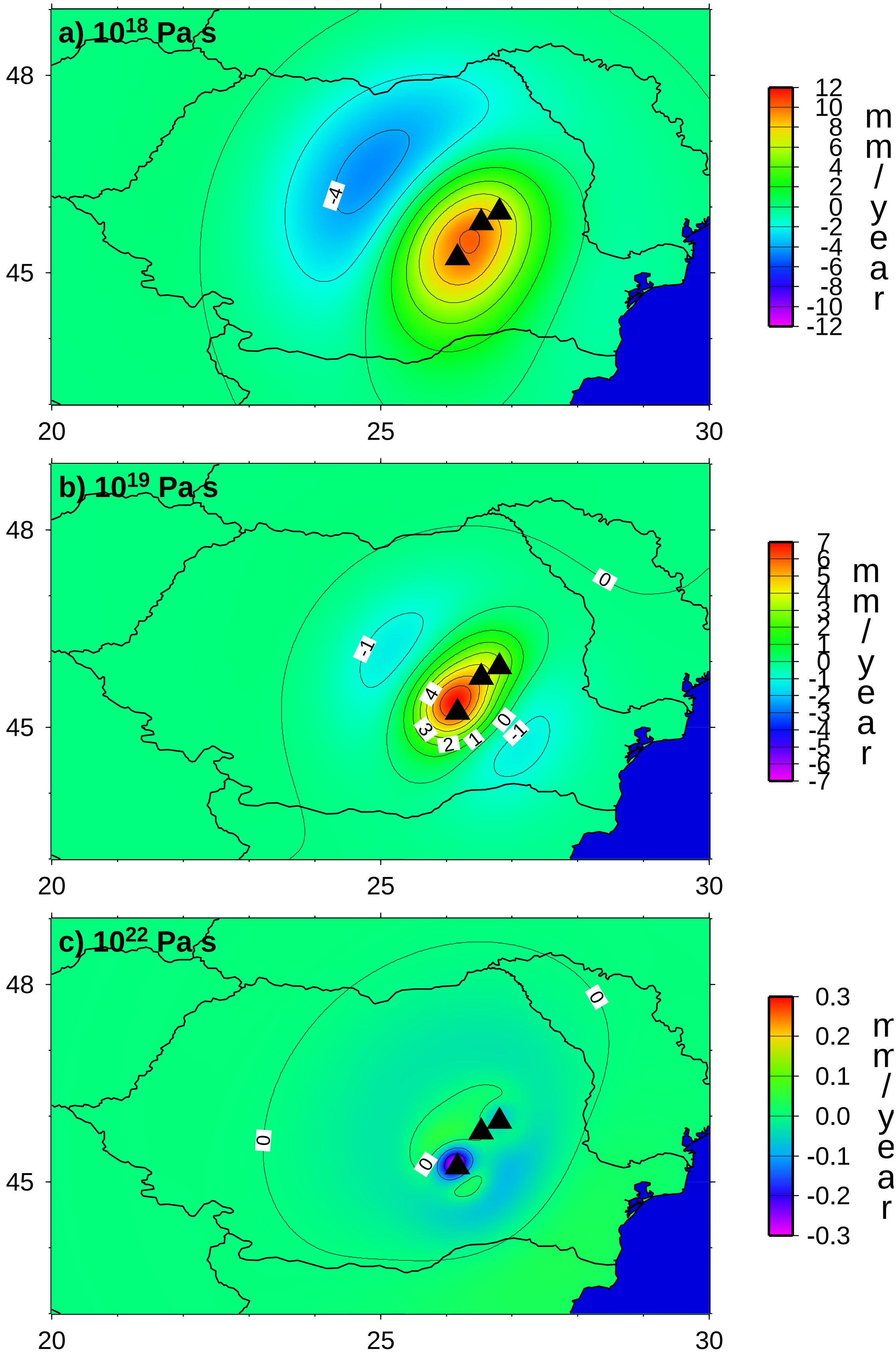

Figure 5.18 Average vertical surface displacement change from 2002 to 2006 over Romania for an Earth model with varied asthenosphere viscosity. The 2-D locations of the earthquakes are indicated by a black triangle

Table 5.21 Maximal horizontal velocity

Ast. viscosity (Pa s)	4-Mar-77 (mm/year)	30-Aug-86 (mm/year)	30-May-90 (mm/year)	Total (mm/year)
10^{18}	2,43	1,78	0,63	2,18
10^{19}	1,91	0,90	0,43	2,32
10^{22}	0,23	0,07	0,09	0,25

Table 5.22 Minimal vertical velocity

Ast. viscosity (Pa s)	4-Mar-77 (mm/year)	30-Aug-86 (mm/year)	30-May-90 (mm/year)	Total (mm/year)
10^{18}	-5,66	-4,19	-1,47	-4,59
10^{19}	-1,54	-1,32	-0,23	-1,28
10^{22}	-0,28	-0,02	-0,08	-0,28

insignificantly small. What stands out is that decreasing the asthenosphere viscosity from 10^{19} to 10^{18} Pa s effects the results induced by the 1986 earthquake the most. This is also valid for the five-layer model and is caused by the difference in depth relative to the other two events.

Table 5.23 Maximal vertical velocity

Ast. viscosity (Pa s)	4-Mar-77 (mm/year)	30-Aug-86 (mm/year)	30-May-90 (mm/year)	Total (mm/year)
10^{18}	9,56	5,86	1,52	10,27
10^{19}	6,43	2,10	1,35	6,89
10^{22}	0,04	0,06	0,01	0,05

Chapter 6

Comparison of modeled values with GPS observations

In this chapter the resulting displacements of several realistic Earth models will be compared to the GPS observed movements at the geographical location of the GPS sites. After more information about the GPS observed and modeled velocities is given.

6.1 GPS observed values

Due to the use of permanent networks that provide accurate geodetic data, GPS is now considered to be one of the most powerful space-geodetic tools to measure the three dimensional surface deformation. Through field campaigns using dense networks and repeating the measurements over spans of several years, the relative motions between stations are estimated with a very high precision of 2-3 mm horizontally and 6-7 mm vertically. This way the crustal movements in Romania have been studied. The resulting velocity vectors are presented as the black arrows in Figures (6.2) to (6.7). Those GPS vector solutions are based on data generated by the combined *Netherlands Research Center for Integrated Solid Earth Sciences* (ISES), the *German Research Foundation* (DFG) and *Collaborative Research Center* (CRC) 461 networks in Romania. People that participated in accomplishing the work have recapitulated it in the paper [*van der Hoeven, et. al.*, 2004], that should be considered as the source of all the information about the GPS-network in Romania in this section and as the source for more information about the project.

The observations started in 1995 when Romania decided to participate in the *Central Europe Regional Geodynamic Project* (CERGOP) to create a network that covers the main tectonic features of the central-eastern part of the continent, the *Central European GPS Geodynamic Reference Network* (CEGRN), with eight stations evenly distributed over the country. Up to 2003 these sites have been observed by CERGOP in four campaigns.

In 1996, DFG funded the CRC 461 to install a GPS network consisting of 28 sites across an area of 250 by 380 km, concentrated around the Vrancea region. Presently the network consist of 56 sites due to expansions achieved by the ISES in close cooperation with the (Romanian) *National institute for Earth's Physics* (NIEP) in 2002 and 2003, extending the area covered to the Black Sea (see Figure 6.1). To date this network has (partly) been measured in 12 GPS campaigns.

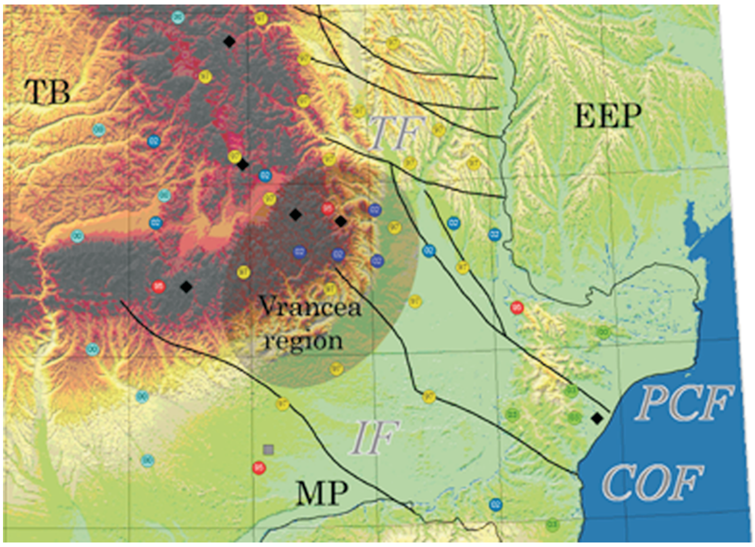

Figure 6.1 GPS network in Central and South-East Romania. The campaign points are indicated by the color-coded circles, the numbers within indicate the last two digits of the year the first measurement at the site took place. The Vrancea region is situated between the Intramoesian fault (IF) and the the Peceneaga-Camena fault (TF). PCF and COF respectively indicate the Peceneaga-Camena fault and the Capidava-Ovidiu fault. TB indicates the Transylvanian basin, EEP the East-European platform and MP the Moesian platform. The blue area is the Black Sea. [*van der Hoeven, et. al.*,2004]

For the Dutch group data processing is performed using the Jet Propulsion Laboratory's (JPL) GIPSY-OASIS software package with a version of JPL's precise point positioning, calculating the GPS motions in the ITRF-2000 reference frame. This results in GPS vectors relative to the assumed stable Eurasian platform. Furthermore, it should be noted that not all the sites given in Figure (6.1) are used in the interpretation of the results. Only the solutions based on stations observed during at least four campaigns (older than 1998) and showing a sufficient confidence level are used. Future campaigns will provide the information needed to enlarge the number of horizontal velocity vectors for analysis. They also provide more data of vertical movements leading to longer time series needed to provide consistent solutions.

The most important conclusion in [*van der Hoeven, et. al.*, 2004] for this report, is that the observed present-day motion in the area between the Vrancea region and the Black Sea, relative to Eurasian platform, tend to point away from the Vrancea region. This indicates a plate divergence between the Tisia-Dacia block, the Moesian plate and the East-European platform.

6.2 Modeled values

In Chapter (5) several Earth models were simulated and their results compared. When all the figures of the horizontal velocities are examined one general conclusion can be made concerning the velocities in the region of interest, the area between the Vrancea region and the Black Sea. Although the changes to the model parameters can have a respectable influence to the magnitude of the vectors, they always point more or less towards the southeast. This is the same direction the velocities calculated on the base of the GPS observations are pointing, making it interesting to compare both velocity vectors (see Section 6.3). However, first more information shall be presented in relation to the Earth model, earthquake parameters and the time span used for the calculations of the postseismic relaxation. This as they differ from the previous chapter.

As stated before the original five- and seven-layer Earth models are based on the strength profile [*Lankreijer, et. al.*, 1997]. Although the profile can only be used as an indication, recent measurements and research have pointed out that the five-layer Earth model corresponds well with the local Earth structure [*Mocanu*, 2004]. It was decided to use an Earth model with a 40 km thick elastic lithosphere above a 100 km thick lithospheric mantle, and a mantle and a core with no change in the depth of the Core Mantle Boundary (CMB). This means that relative to the models used in Chapter (5.1) the asthenosphere has disappeared. However, the lithospheric mantle is divided into an upper section (ULM) with a fixed viscosity of 10^{22} Pa s and a lower part (LLM), for which it is assumed that the viscosity is ranging between 10^{17} and 10^{19} Pa s. The value of the mantle viscosity is equal to 10^{21} Pa s. The boundary between both parts of the lithospheric mantle is believed to be situated at a depth of either 70 or 90 km. The density and shear modulus are calculated by PREM [*Dziewonski and Anderson*, 1981]. This results in six different Earth models that will be compared to the GPS observations. These models are probably not adequate for other regions and therefore the different vectors and their possible correlation will not be discussed for regions other than the southeast of Romania.

Another difference to the data used to simulate the results in Chapter (5) is that it was important for this simulation that the earthquake parameters were correct. As discussed in Chapter (2) there are significant differences between the seismic source parameters given by CMT Harvard (see Table 2.1) and the regional institute (see Table 2.2). As there were no factors known, that could be used to determine which is more accurate, both were applied to each Earth model. This resulted in two different modeled sets of velocities. Furthermore, the 31 May 1990 earthquake was included so all the earthquakes with a moment magnitude larger than 6 of the last 30 years were used for the postseismic relaxation calculations. Finally, for the calculation of the velocities an average value was taken of the postseismic displacements over a period from 1997 to 2003, the same period that the GPS observations took place.

6.3 Comparison of GPS observed and numerically modeled velocities

The resulting velocity vectors for the six Earth models described above and the velocity vectors based on the GPS observations are given in Figures (6.2) to (6.7). In these figures. the arrow of the GPS velocity vector is surrounded by an ellipse. The surface of the ellipse is based on the standard deviation of the observations at that station. The larger the ellipse, the more the observed values diverge from their mean value. This also means that when a modeled velocity vector points within the deviation ellipse at a site, the modeled value falls within the range of values observed at that site. Therefore, the modeled values are considered to be a good approximation of the observed value.

A general conclusion made concerning these figures is that the direction of the modeled velocity vectors is almost independent of the model used and that

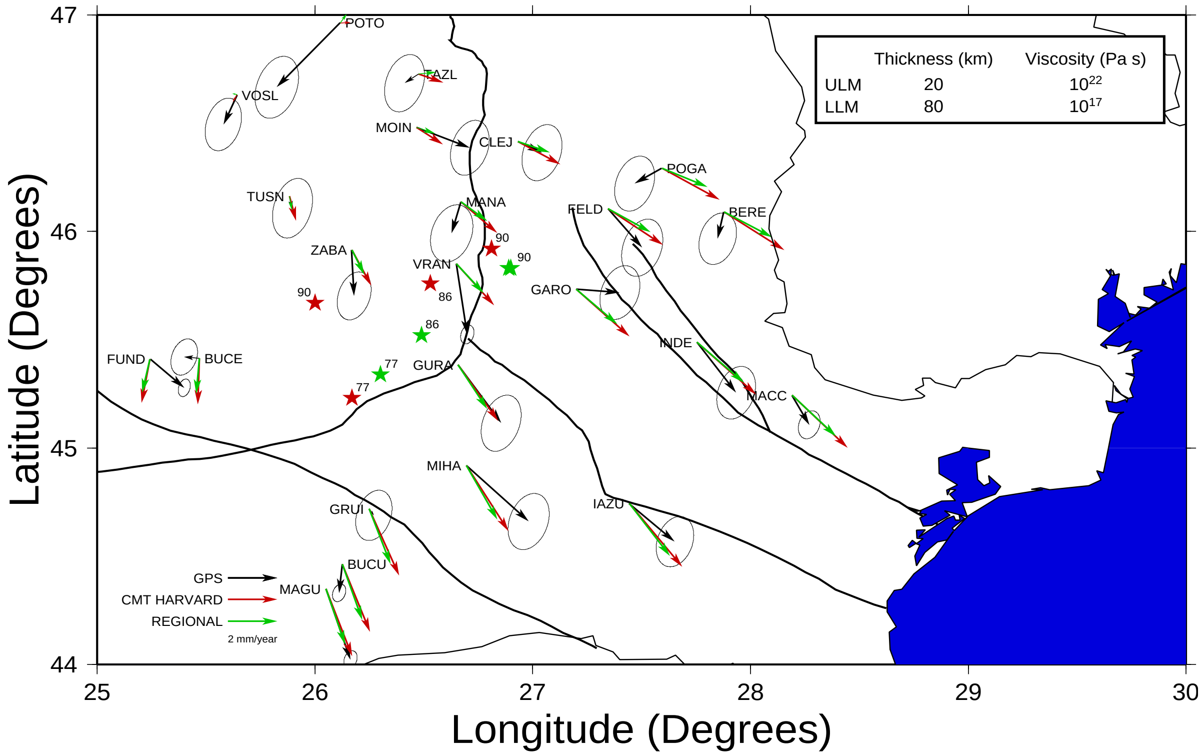

Figure 6.2 The average horizontal displacement change for a period between 1997 and 2003 and the GPS observed displacement changes, at the geographical position of the included GPS sites in south-east Romania. The legend in the lower left corner indicates the source of the seismologic data used and the unit length of 2 mm/year. The box in the upper left corner of the figures explain the structure of the lithospheric mantle of the model. The major fault zones in the area are depicted by the black lines. The stars and the last numbers of the year in which they occurred indicate the 2-D locations of the earthquakes and their color corresponds with the legend.

the direction coincides reasonably well with the direction of the velocity vectors based on the GPS observations. There are however small differences between the direction of the vectors based on the seismic data of the CMT Harvard Catalogue and the regional institute. This is not very odd when the location of the earthquakes according to both sources are considered. The most striking difference is between the two dimensional locations of the May 31 1990 earthquake. According to the regional information the earthquake occurred at almost exactly the same location as the May 30 1990 earthquake, while the CMT Harvard Catalogue indicates a position almost 75 km westwards. The accuracy of this position is questionable but as Tables (2.1) and (2.2) illustrate, the May 31 1990 earthquake was ten times smaller than the May 30 1990 event, which already had the weakest influence to the total (see Chapter 5) making the influence of the first almost insignificant.

The figures also show that the velocity vectors are always larger in magnitude when the upper lithospheric mantle (ULM) and the lower lithospheric mantle (LLM) thicknesses are 20 to 80 km compared to the model with same LLM viscosity but a different lithospheric mantle division. This implies that for a certain LLM viscosity, the magnitude of the modeled results corresponds best to the magnitude of the GPS observed velocities when the LLM is the thickest. For the model with an LLM viscosity equal to 10^{19} Pa s (Figure 6.6) the correlation

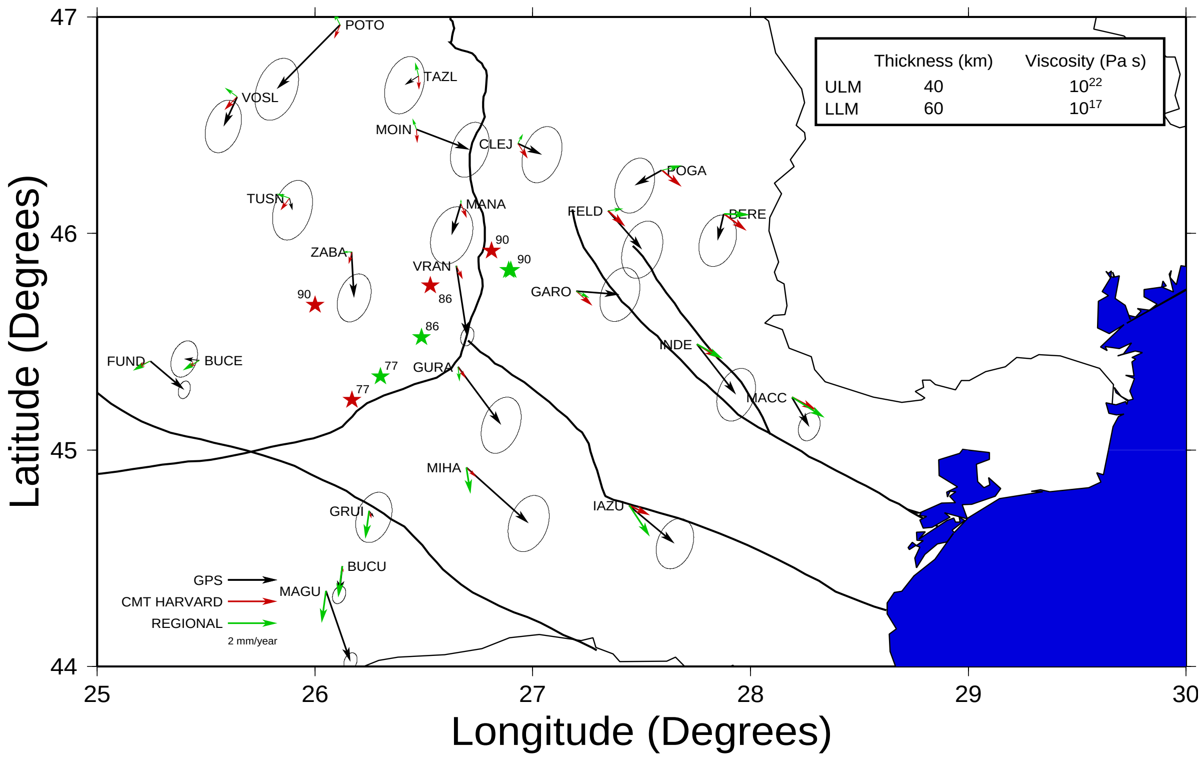

Figure 6.3 The average horizontal displacement change for a period between 1997 and 2003 and the GPS observed displacement changes, at the geographical position of the included GPS sites in south-east Romania. The box in the upper left corner of the figures explain the structure of the lithospheric mantle of the model.

is restricted to results based on the GMT Harvard data and close to the Vrancea region. As the distance to the epicenters enlarges the velocity magnitude of the modeled velocities rapidly decreases, while the magnitudes of the GPS observed values remain almost constant.

For the models with an LLM viscosity of 10^{17} and 10^{18} Pa (Figures 6.2 and 6.4) this is not the case. The correspondence between the modeled velocity vectors and the GPS observed movements remains, independent of which seismic data was used. Furthermore, because the magnitude does not decrease as rapidly, the correlation also remains in the regions further away from the epicenters. This happens not only in the southeast direction towards the Black Sea, but also in the center of the figures, near the Peceneaga-Camena fault and to a lesser extend for the Moesian platform. In the latter region the modeled values correspond well with the observed values at site MAGU, but the magnitude of the observed velocity vectors at the other two local sites are a lot smaller while the modeled values remain constant. Note the fact that the decrease of the velocity with increasing distance to the epicenters is smaller for lower LLM (asthenosphere) viscosities, as was already demonstrated in Chapter (5).

These conclusions are emphasized by the values in Table (6.1) where a misfit value defined as

$$N_{mf} = \frac{1}{M} \sum_{i=1}^{M} \frac{\|\vec{x}^{i}_{mod} - \vec{x}^{i}_{obs}\|}{\sigma^{i}_{obs}} \tag{6.1}$$

is given. In the equation x^i represents the motion vector at station (i) and the subscripts mod and obs represent originated from postseismic model simulations

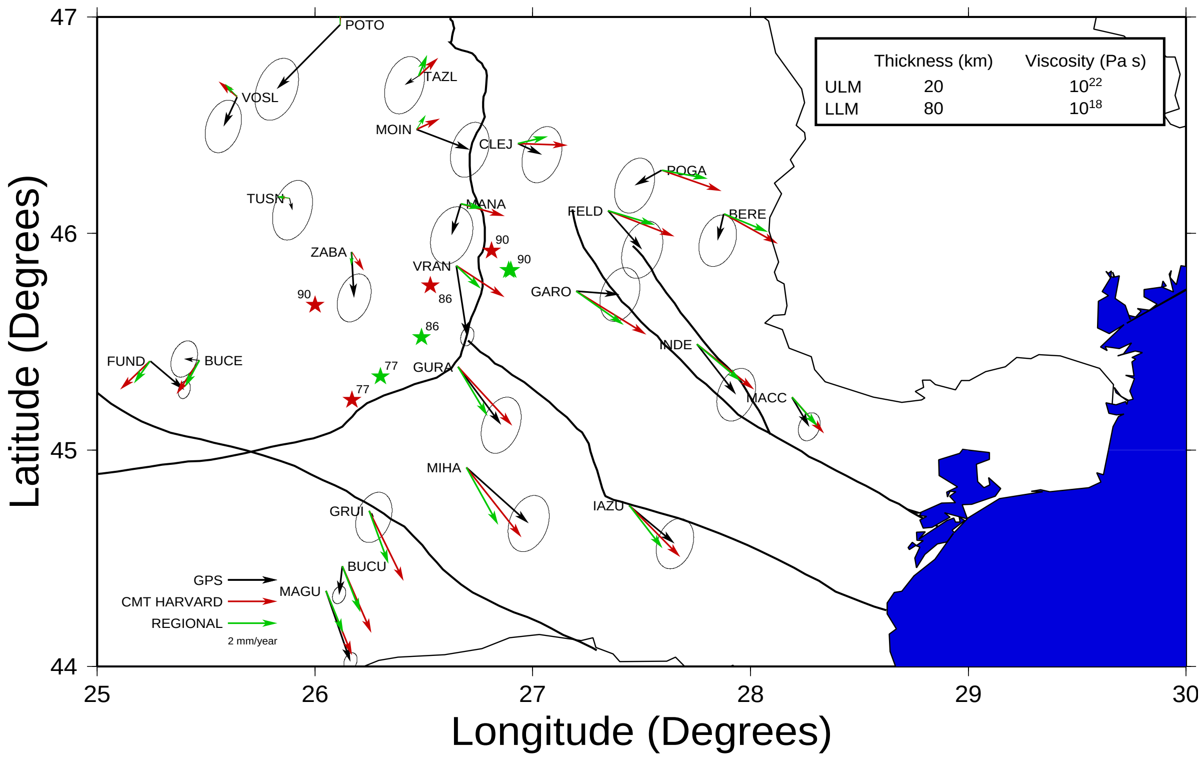

Figure 6.4 The average horizontal displacement change for a period between 1997 and 2003 and the GPS observed displacement changes, at the geographical position of the included GPS sites in south-east Romania. The box in the upper left corner of the figures explain the structure of the lithospheric mantle of the model.

and GPS observations, respectively. The formula calculates the ratio of the difference between the magnitudes of the vectors to the standard deviation in the direction of the difference. This means that the smaller this misfit value, the better the modeled value approached the observed value. The value will be smaller than 1 if the modeled velocity vector is a good approximation and thus falls in the deviation ellipse. Here this value has been averaged for three combinations of GPS sites:

- $\boldsymbol{A}$: stations GURA, MIHA and IAZU
- $\boldsymbol{B}$: $\boldsymbol{A}$ + stations GRUI, BUCU and MAGU
- $\boldsymbol{C}$: $\boldsymbol{B}$ + stations GARO, INDE and MACC

thus describing an expanding area. In situation ($\boldsymbol{A}$) only the three stations representing the tectonic unit between the faults and southeast of the Vrancea area (see Figure 6.1) were included. In situation ($\boldsymbol{B}$) the three sites representing the Moesian platform are added and for situation ($\boldsymbol{C}$) again three stations are added, giving the results for the area surrounding the Peceneaga-Camena fault. The locations of the stations can be found in Figure (6.2). Table (6.1) shows what is visible in Figures (6.2 - 6.7). The best correlation is obtained when the thickness distribution of the LM is 20-80 km and the LLM viscosity is equal to 10^{17} or 10^{18} Pa s, independent of which source is used for the seismic data. For case ($\boldsymbol{A}$) the values are below one, so on average the three modeled vectors are within the uncertainty range for these sites. When the three stations to the south of the Vrancea region are included in the calculations (Case $\boldsymbol{B}$) the misfit increases significantly no matter which Earth model is used. The numbers decrease again when three

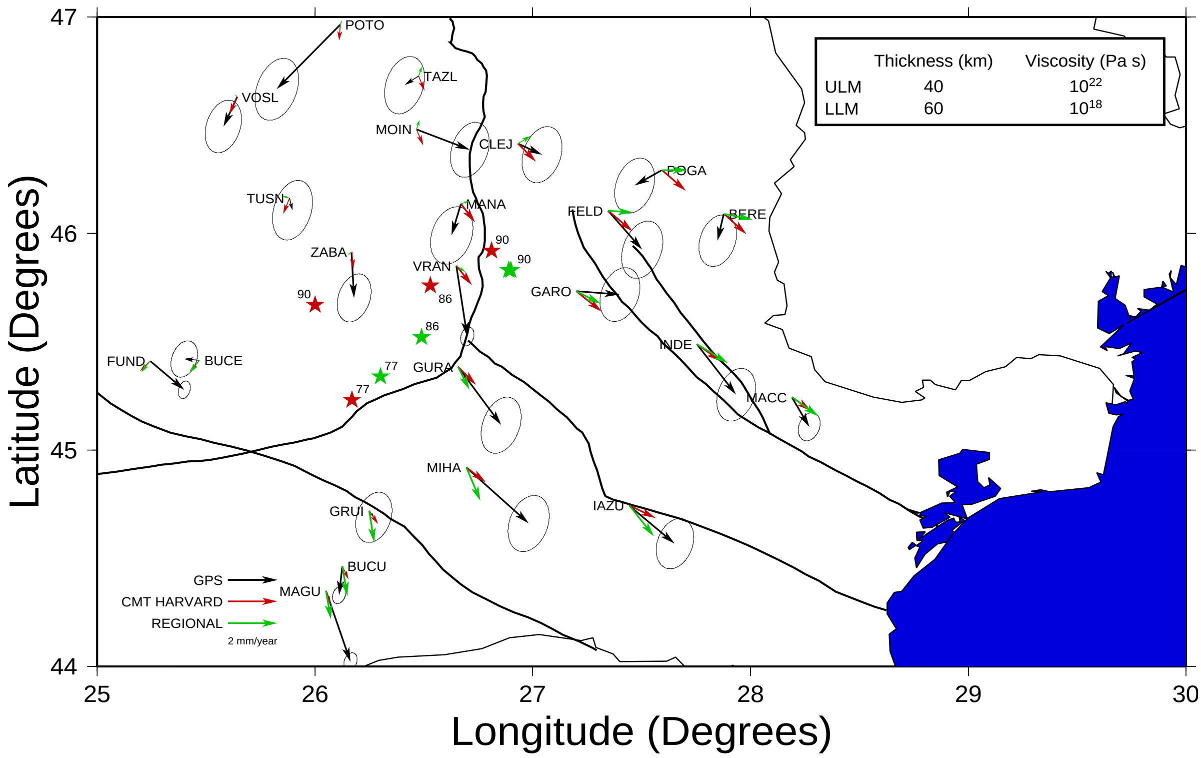

Figure 6.5 The average horizontal displacement change for a period between 1997 and 2003 and the GPS observed displacement changes, at the geographical position of the included GPS sites in south-east Romania. The box in the upper left corner of the figures explain the structure of the lithospheric mantle of the model.

Table 6.1 The misfit value N_{mf} for three different situations. The name of the Earth models consists of three pairs of numbers. The first two denote the logarithmic value of the lower lithospheric mantle (LLM) viscosity and the others indicate respectively the thickness of the upper lithospheric mantle (ULM) and the LLM in kilometers. The three letters added to the model name denote the seismic source of the data. CMT = CMT Harvard Catalogue. REG = regional network.

Model	*A*	*B*	*C*
172080 CMT	0.837	2.151	2.116
174060 CMT	2.249	3.469	2.872
182080 CMT	0.654	2.160	1.887
184060 CMT	1.950	3.027	2.529
192080 CMT	1.350	2.445	2.345
194060 CMT	2.022	2.882	2.661
172080 REG	0.922	2.069	1.870
174060 REG	1.869	2.286	2.039
182080 REG	0.775	2.107	1.738
184060 REG	1.528	2.274	1.956
192080 REG	1.706	3.000	2.684
194060 REG	1.981	3.190	2.803

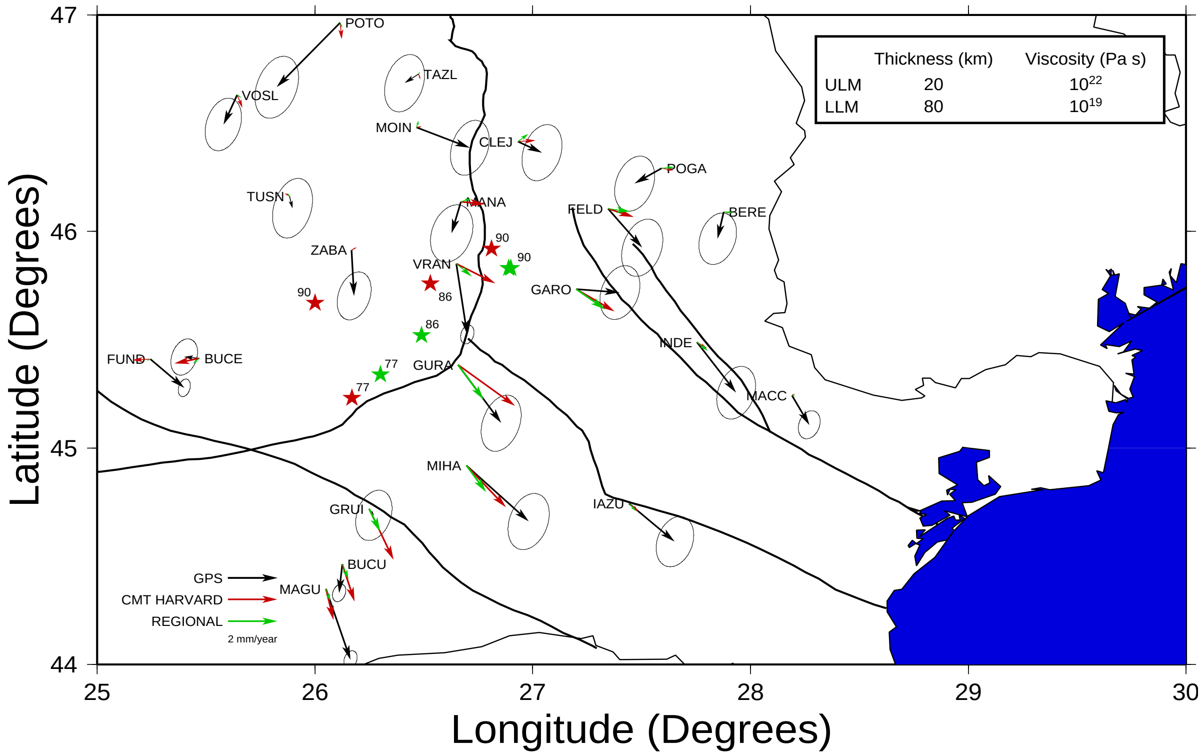

Figure 6.6 The average horizontal displacement change for a period between 1997 and 2003 and the GPS observed displacement changes, at the geographical position of the included GPS sites in south-east Romania. The box in the upper left corner of the figures explain the structure of the lithospheric mantle of the model.

stations to the north of the Vrancea region are also included (Case C) but never approximate the station's observations as well as in the first case. This can be explained by the fact that the Earth model was based on the Earth structure beneath the Vrancea region. The table also shows that for cases (B) and (C) the lowest misfit values are acquired when the simulation is based on the seismologic data from the regional institute.

It can be concluded that if models (**172080**) or (**182080**) of Table (6.1) do indeed describe the structure of the Earth in the Vrancea region, postseismic Earth relaxation is the main contributor to the observed horizontal displacements of the local Earth's surface. Whereas, if one of the other Earth models are a better approximation, postseismic relaxations still contributes to the total displacements. However, the main source should be searched in other, probably long-term, geological processes.

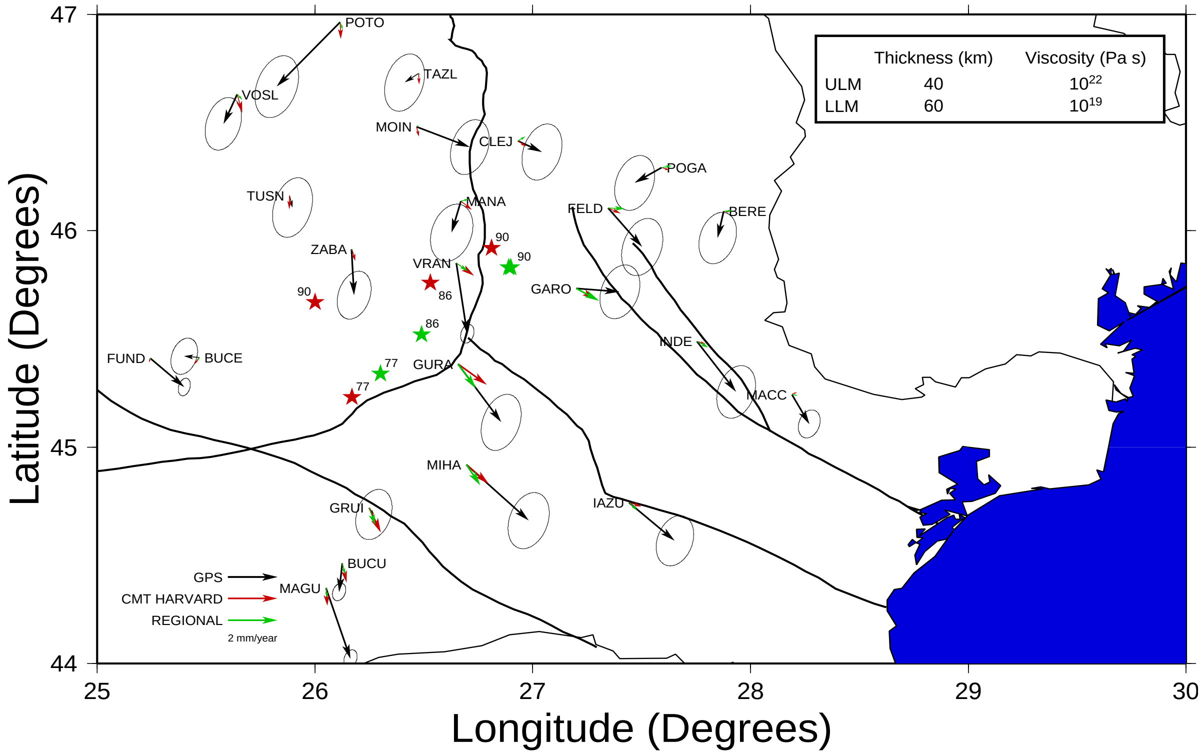

Figure 6.7 The average horizontal displacement change for a period between 1997 and 2003 and the GPS observed displacement changes, at the geographical position of the included GPS sites in south-east Romania. The box in the upper left corner of the figures explain the structure of the lithospheric mantle of the model.

Chapter 7

Conclusions and Recommendations

In this final chapter the conclusions pertaining to the generated results given in Chapters (5) and (6) are presented. The conclusions are mainly concentrated on the area between the Vrancea region and the Black Sea. The discussion concerning the whole displacement field of intermediate-depth earthquakes in general will not be repeated. For more information on this subject refer to Chapter (5). After the conclusions, recommendations for the required continuation of this research are discussed.

7.1 Conclusions

It is concluded that GPS observations demonstrate that there is a contribution of the four largest intermediate-depth Vrancea earthquakes of the last thirty years to the present-day horizontal surface displacements in the area between the Vrancea region and the Black Sea. The direction of the average displacements of the numerically modeled values corresponds reasonably well with the GPS observed vectors in this area and the directions remain practically unaltered when realistic changes are applied to the Earth model. The extent to which the magnitudes of the modeled values correspond to the magnitudes of the horizontal observed displacements depends mainly on the structure of the lithospheric mantle in the Earth model. It has been illustrated that the magnitude of the average displacements can be increased by:

- inserting a low-viscosity zone (LVZ) with a viscosity between 10^{17} and 10^{20} Pa s at the bottom of the lithosphere.
- decreasing the viscosity of the upper lithospheric mantle (ULM) from elastic to minimal 10^{20} Pa s.
- decreasing the depth of the boundary between the upper lithospheric mantle and the lower lithospheric mantle whilst keeping the total thickness constant.
- decreasing the viscosity of the lower lithospheric mantle (LLM) to a minimum of 10^{17} Pa s.

Note that the first three hardly change the location of the 0.5 mm/year contour, which means that the increase is confined to the area close to the epicenters of the earthquakes. Decreasing the LLM viscosity especially increases the velocities in the far-field leading to wider contours that surround a greater area and to the relocation of the maximal velocities away from the epicenters towards the center of the region of interest. It does, however, not always result in an increase of the maximal average horizontal displacement.

In addition, an LVZ also results in a change of direction of the average horizontal displacements in the south and east of the epicenters. This leads in south-east Romania to a displacement field whereof almost all the vectors point towards the south-east. Whereas, for the model without the LVZ, a radially distributed displacement field was found. Furthermore it must be noted that an LVZ does not influence the changes to the average displacements as a result of variations applied to the parameters of the lithospheric mantle. Thus when for example an LVZ is added to a model and the LLM viscosity is decreased, the total resulting change to the displacements will be a combination of the changes induced by the applied modifications separately.

All these findings lead to the conclusion that the GPS observed displacements can be approached reasonably accurately by a realistic Earth model, meaning that the intermediate depth seismicity should be considered as a very important component of the observed horizontal crustal displacements. These GPS measurements can, on the other hand, not give the definite answer to which Earth model describes the Earth's structure underneath the Vrancea region best. None of the models used in the simulations can be excluded on a basis of poor correspondence between directions. The correspondence between the magnitudes leads to preference of the models with an ULM of 20 km, an LLM of 80 km thick and an LLM viscosity of either 10^{17} or 10^{18} Pa s. The other Earth models can, however, not completely be excluded because otherwise one would assume that processes like ongoing subduction, mantle delamination, ongoing detachment or crustal rebound after detachment, correspond with hardly any horizontal displacements.

For the same reasons it is concluded that the vertical solutions of the GPS observations probably will not answer the question either. The differences between the average vertical displacement pertaining to the different models are similar to the average horizontal displacements. This means that even when the accuracy of the GPS observation increases, the comparison will probably again result in a preference for a couple of models, but the comparison can not be completed separately from the ongoing processes in the region.

7.2 Recommendations

The first recommendation concerns the Earth model used. In a region known for its lateral inhomogeneity, a rather simple laterally homogeneous, radially stratified model does not suffice to produce conclusive results. So, it is advised to simulate a laterally inhomogeneous model or a combination of several laterally homogeneous models with different compositions that approach the Earth's structure in the whole of Romania as accurately as possible. This way the discussion is no longer restricted to south-east Romania, but accurate displacements will be also available for the north-west of the Vrancea region where the effect of the ongoing tectonic processes should also be noticeable. It also results in the possibility to insert (a) local low-viscosity zone(s) where the presence of one has been pointed out by seismology or tomographic imaging, and take to the decreasing lithospheric thickness towards the Black Sea into account. Until the arrival of undisputed evidence for the structure of the lithospheric mantle, it is not advised to continue the work with only one Earth model, but to proceed with simulating Earth models based on all possibilities.

It is also recommended to continue the GPS observations to ensure results of a higher precision for both the horizontal and vertical displacements. This will make it in the first place possible to compare the vertical GPS observed values to numerically modeled values. Secondly, it will lead to accurate residual motions when the observed values are subtracted from the average displacements resulting from the improved Earth models. GPS measurements closer to the Romanian coast of the Black Sea should also be considered useful, because the results have identified that the largest differences between the Earth models are noticeable in the far-field of the earthquakes. Relatively small displacements there would lead to models with higher LLM viscosities and/or a thicker ULM.

The final recommendation is that those residual motions should be studied closely together with the geological processes in the region. Due to the uncertainties concerning the structure of the local Earth, especially the viscosity of the lower lithospheric mantle, it might be useful to have the three dimensional displacements as they are supposed to have been caused by subduction, mantle delamination, ongoing slab-detachment and a sinking detached slab separately, based on similar Earth models. This way, after comparing these results to the GPS observed displacements and the numerically modeled postseismic displacements based on several Earth models, a definite answer might be found to what the correct Earth structure in the Vrancea region is, and which processes are taking place underneath. Or if this is too optimistic, at least some of the Earth models and geologic processes can be excluded for further research.

Bibliography

Aoudia, A., A. Borghi, R. Riva, R. Barzaghi, B.A.C. Ambrosius, R. Sabadini, L.L.A. Vermeersen and G.F. Panza, 2003, Post-seismic deformation following the 1997 Umbria-Marche (Italy) moderate normal faulting earthquakes, *Geophys. Res. Lett.*, **30**(7).

Bada, G., F. Horváth, P. Gerner and I. Fejes, 1999, Review of the present-day geodynamics of the Pannonian basin: progress and problems, *Geodynamics*, **27**, 501–527.

Bala, A., M. Radulian and E. Popescu, 2003, Earthquakes distribution and their focal mechanism in correlation with the active tectonic zones of Romania, *Geodynamics*, **36**, 129–145.

Bavinck, H. and H.G. Meijer, 2002, Lecture notes WI4007TU: Fourier- and Laplace Transformation, *Geodynamics*, **36**, 129–145.

Bazacliu, O. and M. Radulian, 1999, Seismicity variation in depth and time in the Vrancea (Romania) subcrustal region, *Natural Hazards*, **19**, 165–177.

Becker, M., D. Ghitau, C. Marcu, P. Neumaier, F. Radulescu, E. Reinhart, V. Rosca, T. Rus and H. Seeger, Plate Kinematic Studies in Romania using GPS, Symposium G16 ”Geodetic and Geodynamic Achievements of the CEI”, EGS98, XXIII General Assembly, Nice, France, 20-24 April 1998.

Cesca, S., L.L.A. Vermeersen and R. Sabadini, 2000, Influence of lithospheric and mantle stratification on co- and post-seismic deformation due to finite faults, *Geophys. J. Int.*, **143**, 575–581.

Chalot-Prat F. and R. Girbacea, 2000, Partial delamination of continental mantle lithosphere, uplift-related crust-mantle decoupling, volcanism and basin formation: a new model for the Pliocene-Quaternary evolution of the southern Eart-Carpathians, Romania, *Tectonophysics*, **327**, 83–107.

Cloetingh, S., F. Horváth, C. Dinu, R.A. Stephenson, G. Bertotti, G. Bada, L. Matenco, D. Garcia-Catellanos and the TECTOP Working Group, 2003, Probing tectonic topography in the aftermath of continental convergence in Central Europe, *EOS*, **11**, 89–96.

Dinter G. and G. Schmitt, 2001, Three dimensional plate kinematics in Romania, *Natural Hazards*, **23**, 389–406.

Dziewonski A.M. and D.L. Anderson, 1981, Preliminary reference Earth model (PREM), *Phys. Earth Planet. Inter.*, **25**, 297–356.

Fan, G., T.C. Wallace and D. Zhao, 1998, Tomographic imaging of deep velocity structure beneath the Eastern and Southern Carpathians, Romania: Implications for continental collision, *J. Geophys. Res.*, **103**(B2), 2705–2733.

Gilbert F. and G. Backus, Elastic-gravitational vibrations of a radially stratified sphere, in *Dynamics of Stratified Solids*, ed. G. Hermann, American Society of Mechanical Engineers, New York, 1968.

Gîrbacea R. and W. Frisch, 1998, Slab in the wrong place: Lower lithospheric mantle delamination in the last stage of the Eastern Carpathian subduction retreat, *Geology*, **26**(7), 611–614.

Gusev, A., M. Radulian, M. Rizescu and G.F. Panza, 2002, Source scaling of intermediate-depth Vrancea earthquakes, *Geophys. J. Int.*, **151**, 879–889.

Gvirtzman, Z., 2002, Partial detachment of a lithospheric root under the southeast Carpathians: Towards a better definition of the detachment concept, *Geology*, **30**(1), 51–54.

Hanyk, L., 1999, Ph.D. Thesis: Viscoelastic response of the Earth: Initial-value approach, Faculty of mathematics and physics, Charles University, Prague.

Lankreijer, A., V. Mocanu and S. Cloetingh, 1997, Lateral variations in lithosphere strength in the Romanian Carpathians: constraints on basin evolution, *Tectonophysics*, **272**, 296–290.

Lay, D.C., 1998, *Linear algebra and its applications*, chapter **3**, pp. 179–204, Addison Wesley Longman, Inc., 1998, second edition.

Linzer, H.-G., W. Frisch, P. Zweigel, R. Girbacea, H.-P. Hann and F. Moser, 1998, Kinematic evolution of the Romanian Carpathians, *Tectonophysics*, **297**, 133–156.

Mocanu, V., Earth structure in the Vrancea region, *Personal communication*, April 2004.

Mueller, D., University of Sidney, url: http://www.earth.northwestern.edu, Accessed on: September 21 2004.

Nemcok, M., L. Pospisil, J. Lexa and R. A. Donelick, 1998, Tertiary subduction and slab break-off model of the Carpathian-Pannonian region, *Tectonophysics*, **295**(3–4), 307–340.

Piersanti, A., G. Spada, R. Sabadini and M. Bonafede, 1995, Global post-seismic deformation, *Geophys. J. Int.*, **120**, 544–566.

Popescu E. and M. Radulian, 2001, Source characteristics of the seismic sequences in the Eastern Carpathians foredeep region (Romania), *Tectonophysics*, **338**, 325–337.

Riva, R., A. Aoudia, L.L.A Vermeersen, R. Sabadini and G.F. Panza, 2000, Crustal versus asthenospheric relaxation and post-seismic deformation for shallow normal faulting earthquakes:the Umbria-Marche (central Italy) case, *Geophys. J. Int.*, **141**, F7–F11.

Riva R.E.M. and L.L.A Vermeersen, 2002, Approximation method for high-degree harmonics in normal mode modelling, *Geophys. J. Int.*, **151**, 309–313.

Sabadini R. and L.L.A Vermeersen, 1997, Influence of lithospheric and mantle stratification on global post-seismic deformation, *Geophys. Res. Lett.*, **24**(16), 2075–2078.

Sklyarov, A., url: http://piramyd.express.ru, Accessed on: April 29 2004.

Sperner, B., F. Lorenz, K. Bonjer, S. Hettel, B. Müller and F. Wenzel, 2001, Slab break-off – abrupt cut or gradual detachment? New insights from the Vrancea Region (SE Carpathians, Romania), *Terra Nova*, **13**, 172–179.

Stein, S. and M. Wysession, An introduction to seismology, earthquakes, and earth structure, chapter **4.2**, pp. 215–219, Blackwell Publishing Ltd., 2003

van der Hoeven, A., G. Schmitt, G. Dinter, V. Mocanu and W. Spakman, 2004, GPS Probes the kinematics of the Vrancea seismogenic zone, *EOS*, **19**, 185–196.

Vermeersen, L.L.A., 2002a, Lecture notes AE4-876: Earth-oriented space research, Delft University of Technology, The Netherlands.

Vermeersen, L.L.A., 2002b, Lecture notes AE4-877: Geophysical applications of satellite measurements, Delft University of Technology, The Netherlands.

Wortel, M.J.R. and W. Spakman, 2000, Subduction and slab detachment in the Mediterranean-Carpathian region, *Science*, **290**, 1910–1917.

Appendix *A*

Mathematical operators

Following mathematical operators used in the report are explicitly written out in spheroidal coordinates, starting with the ∇ operator

$$\nabla = \frac{\partial}{\partial r}\hat{e}_r + \frac{1}{r}\frac{\partial}{\partial \theta}\hat{e}_\theta + \frac{1}{r\sin(\theta)}\frac{\partial}{\partial \phi}\hat{e}_\phi \tag{A.1}$$

This is followed by the introduction of the gradient of a vector $\vec{v} = v_r\hat{e}_r + v_\theta\hat{e}_\theta + v_\phi\hat{e}_\phi$

$$\nabla\vec{v} = \sum_{k=1}^{3}\sum_{l=1}^{3}\left[(\nabla\vec{v})_{kl}\,\hat{e}_k\hat{e}_l\right] \qquad \text{with} \tag{A.2}$$

$$\begin{aligned}
&(\nabla\vec{v})_{rr}=\frac{\partial u_r}{\partial r}, && (\nabla\vec{v})_{\theta r}=\frac{1}{r}\frac{\partial u_r}{\partial \theta}-\frac{u_\theta}{r}, && (\nabla\vec{v})_{\phi r}=\frac{1}{r\sin\theta}\frac{\partial u_r}{\partial \phi}-\frac{u_\phi}{r},\\
&(\nabla\vec{v})_{r\theta}=\frac{\partial u_\theta}{\partial r}, && (\nabla\vec{v})_{\theta\theta}=\frac{1}{r}\frac{\partial u_\theta}{\partial \theta}+\frac{u_r}{r}, && (\nabla\vec{v})_{\phi\theta}=\frac{1}{r\sin\theta}\frac{\partial u_\theta}{\partial \phi}-\frac{u_\phi}{r}\frac{\cos\theta}{\sin\theta},\\
&(\nabla\vec{v})_{r\phi}=\frac{\partial u_\phi}{\partial r}, && (\nabla\vec{v})_{\theta\phi}=\frac{1}{r}\frac{\partial u_\phi}{\partial \theta}, && (\nabla\vec{v})_{\phi\phi}=\frac{1}{r\sin\theta}\frac{\partial u_\phi}{\partial \phi}+\frac{u_r}{r}+\frac{u_\theta}{r}\frac{\cos\theta}{\sin\theta}.
\end{aligned}$$

as well as the first invariant of a tensor $\boldsymbol{t}$

$$\bar{\boldsymbol{t}} = t_{rr} + t_{\theta\theta} + t_{\phi\phi} \tag{A.3}$$

in which the subscript determines the positions in the tensor.

Appendix B

Coefficients of the forcing terms

In this Appendix the forcing terms of the spheroidal ($\tilde{\vec{f}}_{\delta,nm}$ and $\tilde{\vec{f}}_{\delta',nm}$) and of the toroidal components ($\tilde{\vec{g}}_{\delta,nm}$ and $\tilde{\vec{g}}_{\delta',nm}$) are given as obtained from [*Piersanti, et. al.*, 1995] for a dip-slip source with unit moment $\mathscr{M}$. They are given in matrix form and for a fixed degree n, the rows correspond to a distinct order m (m=-2,..,2). For the spheroidal component there are two columns which refer to the third and fourth component of the vector $\tilde{\vec{y}}_{nm}$. The single column present for the toroidal case refers to the second component of the vector $\tilde{\vec{z}}_{nm}$. The dip angle is denoted by δ and r is the distance from the center of the Earth.

Spheroidal components

$$\tilde{\vec{f}}_{\delta,nm}: \quad \begin{array}{l} m=-2 \\ m=-1 \\ m=\ \ 0 \\ m=\ \ 1 \\ m=\ \ 2 \end{array} \quad \begin{bmatrix} 0 & \frac{(2n+1)(n-1)(n+2)}{16\pi r^3}\sin 2\delta \\ \frac{n(n+1)(2n+1)}{8\pi r^3}\cos 2\delta & -\frac{i(2n+1)}{8\pi r^3}\cos 2\delta \\ -\frac{2n+1}{4\pi r^3}\sin 2\delta & \frac{2n+1}{8\pi r^3}\sin 2\delta \\ \frac{i(2n+1)}{8\pi r^3}\cos 2\delta & -\frac{i(2n+1)}{8\pi r^3 n(n+1)}\cos 2\delta \\ 0 & \frac{2n+1}{16\pi r^3 n(n+1)}\sin 2\delta \end{bmatrix} \tag{B.1}$$

$$\tilde{\vec{f}}_{\delta',nm}: \quad \begin{array}{l} m=-1 \\ m=\ \ 0 \\ m=\ \ 1 \end{array} \quad \begin{bmatrix} 0 & -\frac{i(2n+1)}{8\pi r^2}\cos 2\delta \\ -\frac{2n+1}{4\pi r^2}\sin 2\delta & 0 \\ 0 & -\frac{i(2n+1)}{8\pi r^2 n(n+1)}\cos 2\delta \end{bmatrix} \tag{B.2}$$

Toroidal components

$$\tilde{\vec{g}}_{\delta,nm}: \quad \begin{array}{l} m=-2 \\ m=-1 \\ m=\ \ 1 \\ m=\ \ 2 \end{array} \quad \begin{bmatrix} \frac{i(2n+1)(n-1)(n+2)}{16\pi r^3}\sin 2\delta \\ \frac{2n+1}{8\pi r^3}\cos 2\delta \\ -\frac{2n+1}{8\pi r^3 n(n+1)}\cos 2\delta \\ -\frac{i(2n+1)}{16\pi r^3 n(n+1)}\sin 2\delta \end{bmatrix} \tag{B.3}$$

$$\tilde{\vec{g}}_{\delta',nm}: \quad \begin{array}{l} m=-1 \\ m=\ \ 1 \end{array} \quad \begin{bmatrix} \frac{2n+1}{8\pi r^2}\cos 2\delta \\ -\frac{2n+1}{8\pi r^2 n(n+1)}\cos 2\delta \end{bmatrix} \tag{B.4}$$

Appendix C
Residue theorem

In this Appendix a short review is given of the theory concerning the residue theorem as it is presented in [*Vermeersen*, 2002b]. There it is stated that a function $f(z)$ is called analytical at a point $z = z_0$ if the function is differentiable in that point and in a small surrounding area. When the function $f(z)$ is analytical in the complex plane, except in a singularity $z = z_0$, then $f(z)$ can be written as a Laurent series:

$$f(z) = \sum_{n=-\infty}^{\infty} a_n (z - z_0)^n \tag{C.1}$$

Integrating this function over a circle around $z = z_0$ with radius r and replacing $z - z_0$ by re^{it} results in:

$$\oint_c f(z)dz = i \sum_{n=-\infty}^{\infty} a_n r^{n+1} \oint_0^{2\pi} e^{i(n+1)t} dt \tag{C.2}$$

According to the *Cauchy theorem* all the integrals on the right-hand side are zero, except for $n = -1$, therefore:

$$\oint f(z)dz = ia_{-1} \oint_0^{2\pi} e^0 dt = 2\pi i a_{-1} \tag{C.3}$$

The coefficient a_{-1} is called the *residue* of $f(z)$ in $z = z_0$. The *residue theorem* states that if there are a number of singularities in the complex plane, the integral over a closed contour around these singularities is equal to $2\pi i$ times the sum of all the residues belonging to the singularities.

For a singularity in $z = z_0$ with a pole of order m the residue of $f(z)$ in $z = z_0$ is given by

$$a_{-1} = \lim_{z \to z_0} \frac{1}{(m-1)!} \frac{d^{m-1}}{dz^{m-1}} \big((z - z_0)^m f(z) \big) \tag{C.4}$$